ABSTRACT

Title of Document: ISOTOPIC SYSTEMATICS OF ULTRAMAFIC AND MAFIC ROCKS OF THE TAITAO OPHIOLITE, SOUTHERN CHILE

Ruth Frost Schulte, Master of Science, 2007

Directed By: Professor Richard J. Walker
Department of Geology

A variety of ultramafic and mafic rocks from a large, well-mapped sampling of the ca. 6 Ma Taitao Ophiolite, Chile, have been examined. Calculated initial $^{187}Os/^{188}Os$ ratios of the peridotitic rocks range from 0.1168 to 0.1282. Similar ranges of Os isotopic compositions have been reported for abyssal peridotites and peridotites and chromites from some other ophiolites. A correlation between the Mg # of primary olivine grains and Os isotopic compositions of whole rock peridotites suggests that the isotopic variability is due to variable extents of partial melting at approximately 1.5 Ga. This conclusion is also supported by a linear correlation between $^{187}Re/^{188}Os$ and $^{187}Os/^{188}Os$, although how this relation was retained through a second, recent melting event is unclear. The ancient melting event requires that this km-scale block of the mantle remained isolated and unmixed within the convecting upper mantle for a period of ~1.5 Ga. Calculated initial $^{187}Os/^{188}Os$ ratios of the mafic rocks are substantially enriched relative

to the peridotites, suggesting that these rocks were derived via partial melting of portions of the mantle with higher, long/term Re-Os ratios than the ambient upper mantle. The results are comparable to global observations of Os isotopic compositions in mid-ocean ridge basalts (MORB) versus abyssal peridotites. At Taitao, however, the geologic relations are generally well defined.

ISOTOPIC SYSTEMATICS OF ULTRAMAFIC AND MAFIC ROCKS FROM THE TAITAO OPHIOLITE, SOUTHERN CHILE

by

Ruth Frost Schulte

Thesis submitted to the Faculty of the Graduate School of the
University of Maryland, College Park in partial fulfillment
of the requirements for the degree of
Master of Science
2007

Advisory Committee:

Professor Richard J. Walker, Chair
Professor Roberta Rudnick
Assistant Research Scientist Igor Puchtel

ACKNOWLEDGMENTS

First, I want to thank Richard Walker for all his patience and assistance in guiding me through the graduate school process. I'm sure there were times when he scratched his head at my questions and comments. Secondly, I would thank Professor Ryo Anma at Tsukuba University and Professor Maruyama and Dr. Komiya at the Tokyo Institute of Technology for allowing me to select samples from their 2000-2001 and 2002-2003 expeditions to the Taitao Peninsula. You and your graduate students made me feel at ease and I treasure my memories of my time in Tokyo. I am particularly indebted to Kon-san and Shibuya-san for their hospitality and friendship. I would also like to thank Dr. Phil Piccoli for all the hours he spent on the microprobe with me and the hours afterwards helping me understand the results. In addition, thanks to Roberta Rudnick and Igor Puchtel for agreeing to be on my committee despite busy schedules of their own. Thank you to James Farquhar for agreeing to be an unofficial committee member and answering many questions about oxygen isotopes without getting irritated. I also owe my deep gratitude to Mary Horan at the Carnegie Institute of Washington for all her efforts in obtaining Sr and Nd isotopic data for the Taitao peridotites. Many thanks also to Jane Hammarstrom and John Slack at USGS in Reston, VA, for allowing me to use their wonderful Nikon microscope on days that I worked from home.

I would like to thank my parents for always believing in me, loving me and supporting me even when there were times when they thought I might have lost my way and my mind. Mom, you are the steady voice inside my heart that keeps me walking even in the dark. Dad, you are the positive ray of light that brightens my mind and pushes me forward.

To my husband, thank you for the endless encouragement, for the shoulder to lean on, the ear to bend and the hand to hold. You are my soul and teammate. I am so blessed to have found you. I cherish you; love you, and thank you for bringing out the best in me. To Celia, my beautiful daughter, thank you for allowing me the time away from you to finish my degree and for growing into such a wonderful little girl in spite of my many mistakes. To my second child who will be born several months after I have finished my thesis, I hope you will learn to love Earth and its environment with as much wonder as much as I do.

I also want to thank my fellow graduate students for all their support, in particular Tracey Centorbi, Tom Ireland, Nick Geboy, and Margaret Anne Baker. There were countless times when each of you helped me in the lab or answered questions I'm sure I had already asked. I would not have been able to finish without you. Thanks also to Andy Masterson for all the hours he spent loading and running my olivine grains for oxygen analysis as well as the time he took to explain the analytical methods to me.

Last but certainly not least, I would like to extend my deep appreciation to Manuel Schilling for the long hours he spent in the lab confirming my Os isotope analyses and for sharing his thoughts and resources on the Taitao Ophiolite. Muchas gracias para tu ayuda. I hope one day I am able to visit Chile and see the Taitao Peninsula myself.

TABLE OF CONTENTS

LIST OF TABLES

LIST OF FIGURES

CHAPTER 1: INTRODUCTION

Due to the largely inaccessible internal structure of Earth, many questions remain about the chemical composition and evolution of the Earth's interior. One of the fundamental questions in geology relates to the dynamics that operate in the Earth's mantle. Plate tectonics has largely withstood the scrutiny of scientific inquiries for more than 40 years. By now, it is well established that solid-state mantle convection is the driving force behind plate tectonics (e.g., Turcotte and Oxburgh, 1967). However, some details involving the mechanisms and processes that operate in the mantle remain unclear. For instance, at what depths do mantle convection cells originate? What is the fate of subducted lithosphere? How are observed compositional heterogeneities in the mantle generated and when? Geochemical study of basalts and other mantle-derived lavas help answer these questions; however, these materials are sometimes susceptible to contamination via transit through the crust (oceanic and continental) and via interaction with seawater. In addition, lavas can average source heterogeneity so that details of chemical heterogeneity within the mantle may be obscured. For this reason, direct analysis of the upper oceanic mantle (e.g., depleted mid-ocean ridge basalt (MORB) mantle (DMM)) provides complementary information to lavas. This approach is taken here.

1-1 Review of chemical heterogeneity in the mantle

In the early 1960s, the existence of long-term chemical heterogeneity in the mantle was determined by isotope analysis of various ocean-island basalts (OIB) (Faure and Hurely, 1963; Gast et al., 1964; Tatsumoto, 1966). Mid-ocean ridge basalts (MORB) originate from mantle regions that are generally depleted in incompatible elements, whereas OIB are less depleted or even enriched (Allègre et al., 1979; Schilling, 1973). To account for this, the concept of a chemically layered mantle, with an upper depleted and lower undepleted (also called primitive) layer was proposed. Geophysical support for this model comes from the sharp increase in the velocity of seismic waves at a depth of 660-km. The presence of the discontinuity, which shows a density contrast of 10% and boundary transition of less than 10 km, suggests, at the very least, that the mantle consists of two major layers that differ chemically, mineralogically or both (Paulssen, 1988).

The simplistic two-layered mantle model, however, has proven untenable because the compositions of OIB are highly variable such that they could not be derived from a chemically uniform, primitive layer in the mantle. As a result, alternate models have emerged to explain the origin and distribution of chemical heterogeneities in the upper mantle. Early work considered the possibility of contamination of analyzed lavas upon ascent (Gast et al., 1964; O'Hara and Matthews, 1981). For example, Sr isotopes in a range of lavas from the Ascension and Gough islands were examined in an attempt to constrain the cause of observed isotopic heterogeneity in the convecting upper mantle (Gast et al., 1964). The lack of correlation between Sr isotopes and some elements that are enriched in the continental crust argued against crustal contamination. The possibility that contamination of large-ion lithophile elements (LILE) could occur by periodic

interaction with a long-lived magma chamber was considered, though time constraints provided by U-series isotopes have largely ruled this out (O'Hara and Mathews, 1981). Other authors have proposed that old continental lithosphere may have contaminated some plume sources (Widom et al., 1997; Moreira et al., 1999). In general, it is now largely agreed that the origin of OIB is varied and complex.

Chemical heterogeneity has also been noted in the sources of MORB, sometimes over minor distances. Two general types of models have been proposed to account for heterogeneity along ocean ridges. One claims that the depleted upper mantle is well-mixed and receives injections of enriched material from isolated plumes that rise from the lower mantle (Schilling, 1973; Hanan et al., 1986; Brandon et al., 2000). The presence of ocean islands and large seamounts provides surficial evidence for these plumes or 'hotspots' (Morgan, 1971). This model, known as the 'hotspot source-ridge sink' model, proffers that the width of a chemical anomaly along the ridge is inversely proportional to the distance of a hotspot from the ridge axis. Hotspots on the ridge or near the ridge but off axis, therefore, are the cause of localized peaks of enrichment along the ridge. In particular, elemental and Sr isotope analysis of Icelandic basalts suggest a region of mixing between plumes (OIB source) and depleted upper mantle (MORB) on the Reykjanes Ridge south of Iceland (Hart et al., 1973). Dredged samples from the axial valley of the Mid-Atlantic Ridge (MAR) and across the Azores platform provide additional Sr isotope data that indicate large variations in MORB samples, but similar isotope ratios in places where MORB and OIB erupt alongside each other (White et al., 1976 and 1979). As a result of the overlap in compositions and respective differences in

degrees of mantle melting, isotopic heterogeneities on a mineralogical scale are thought to be unlikely.

The second set of models is based on the presence of putative dispersed heterogeneities of variable shapes and sizes, or 'blobs,' that are passively embedded in a continually remixing convecting mantle. Referred to by some as the 'plum-pudding' mantle model, enrichment spikes result from random sampling of one of the dispersed heterogeneities with no essential connection to hotspots (Allègre et al., 1980; Batiza, 1984). According to the model, rare large plumes need not rise in one continuous column from the lower mantle. Instead, the plumes could consist of a train of blobs that pass from a lower mantle reservoir through the asthenosphere or be part of the convecting asthenosphere itself (Allègre et al., 1980). Basaltic glasses from Atlantic Ocean basins, for example, record large ranges of Pb isotopes in comparison to those from the East Pacific Rise (Cohen and O'Nions, 1982). To explain this, Cohen and O'Nions argued that equal amounts of heterogeneity in the Atlantic and Pacific upper mantle exist but that MORB from the East Pacific Rise were homogenized in the large magma chamber associated with its fast spreading ridge. Zindler et al. (1984) confirmed this model with the observation that seamounts near the East Pacific Rise exhibit much more variation than the adjacent ridge. Subsequently, Batiza (1984) noted an inverse relationship between ridge spreading rate and the range of $^{87}Sr/^{88}Sr$ ratios. In other words, according to the model, inherent small-scale heterogeneity in the mantle would be homogenized during melting processes associated with fast spreading ridges.

Geophysical data from fluid-dynamic modeling (e.g., Richter and Ribe, 1979; McKenzie, 1979), however, suggest that discrete structures in the mantle (like blobs)

cannot maintain their form for long periods of time in the convecting asthenosphere. Rather, physical homogenization with the depleted reservoir will tend to occur due to elongation and shearing. Alternating bands of depleted lherzolite and enriched pyroxenite in orogenic lherzolites from the Beni Bousera peridotite massif in Morocco provided early evidence of this process (Polvé and Allègre, 1980). Described as 'marble-cake,' the compositional banding may have been produced by convective stirring and stretching of oceanic crust and underlying residual lherzolite, which is later recycled back into the mantle by subduction (Allègre and Turcotte, 1986; Kellogg and Turcotte, 1990; Pearson and Nowell, 2004). One of the problems encountered in this model is the limited observation of very thin pyroxenitic layers (< 1 cm), most likely due to their obliteration by convection or diffusive re-equilibration or the difficulty in identifying them in outcrop (Pearson and Nowell, 2004). Also, some layers of the pyroxenitic layers are mineralogically zoned, which is attributed to high-pressure crystal fractionation with magmatic veins as well as melt-rock reaction with the surrounding peridotite.

Some more recent models advocate melting of veined lithospheric mantle, where the veins are olivine-poor and pyroxene-amphibole-phlogopite-rich, as an explanation for the heterogeneous composition of the oceanic mantle (e.g., Foley, 1992; Irving, 1980; Carlson and Nowell, 2001). In this model, the veins form an enriched network that traverse the depleted mantle. Although similarities exist between the veined mantle model and the marble-cake model, the veins in the former instance are thought to be derived from more immediate surroundings whereas the pyroxenitic layers in the latter may originate from recycled materials. For example, the composition and Os isotopic systematics of potassic magmas from the Navajo Volcanic Field in the Colorado Plateau

reveal that the radiogenic characteristics of the magmas were not due to crustal contamination upon ascent (as might be argued for upper mantle eclogitic xenoliths), but rather were the result of melting of pyroxene- and mica-rich veins in the lithospheric mantle beneath the plateau (Carlson and Nowell, 2001). Upon formation, the melts of the olivine-poor lithologies interact with surrounding metasomatized peridotite or wall rock to create a range of compositions from, in this case, katungite to minette. Problems with this model include constraining the compositions of the pyroxenite sources in relation to the composition of mantle-derived melts.

1-2 The Re-Os isotope system in the mantle

The Re-Os isotope system is potentially an important tool in understanding the timing and creation of chemical heterogeneities in the DMM. ^{187}Re decays to ^{187}Os ($^{187}Re \rightarrow {}^{187}Os + \beta^-$) with a half-life of 41.6 x 10^9 yr and a decay constant (λ) of 1.666 x 10^{-11} yr^{-1} (Smoliar et al., 1996). Unlike other radiogenic isotope systems (i.e., U-Pb, Sm-Nd, Lu-Hf), Re is moderately incompatible during partial melting in the mantle while Os is highly compatible. Mafic oceanic crust is therefore enriched in Re and depleted in Os relative to mantle sources. Conversely, generation and extraction of mafic melts leads to Re depletion and retardation in the growth of $^{187}Os/^{188}Os$ in the residue. As a result, the Re-Os isotope system can provide age constraints on the timing of melt depletion. The high abundance of Os in the mantle residue makes this system relatively impervious to the effects of secondary processes.

There is a limited range of materials with which to study the composition of the convecting upper oceanic mantle: MORB, abyssal peridotites and ophiolites. Each of these comes with problems for the Re-Os system. While MORB is useful in elucidating the range of compositions present in the oceanic upper mantle, their Os isotopic compositions tend to be highly variable and, in general, radiogenic. MORB glasses from the South Atlantic Ridge, for example, have $^{187}Os/^{188}Os$ ratios that range from 0.1314 to 0.2316 (Escrig et al., 2005). Basaltic glasses from the Pacific, Atlantic and Indian mid-ocean ridges also display large variations in $^{187}Os/^{188}Os$ ratios, from 0.128 to 0.163 (Schiano et al., 1997). Proposed reasons for the observed variability include seawater contamination (Roy-Barman and Allègre, 1995), in-situ decay of ^{187}Re (Gannoun et al., 2004), and metasomatism of the asthenospheric mantle by melt percolation from an

ancient subduction zone (Escrig et al., 2005), or primary features indicating mantle chemical heterogeneity (Schiano et al., 1997). Although plentiful and well studied, MORBs are a product of melting and can be affected by interactions with the lithosphere as well as highly radiogenic seawater ($^{187}Os/^{188}Os_{seawater} \sim 1.06$; Levasseur et al., 1998). Also, due to the high Re/Os ratios in most terrestrial basalts, only the youngest samples are useful for initial isotopic composition data and measures must be taken during analysis to determine if hydrothermal alteration has occurred. However, even the least radiogenic samples cannot necessarily be said to be representative of the DMM or unaffected by contamination; and thus, the actual mantle source composition may be considerably lower than any MORB yet analyzed.

Abyssal peridotites are mantle residues of MORB generation and, as such, are presumably representative of the DMM. They contain, on average, 50 to 1000 times more Os than typical MORB (Brandon et al., 2000), so are resistant to alteration by seawater. However, measured abyssal peridotites have Os isotopic compositions that cover a wide range (0.114-0.167; Snow and Reisberg, 1995; Brandon et al., 2000; Standish et al., 2001; Alard et al., 2005; Harvey et al., 2006) yet only modestly overlap those values recorded by MORB (0.127 to >0.2; Roy-Barman and Allègre, 1994; Schiano et al., 1997; Roy-Barman et al., 1998) despite their spatial and genetic association. Indeed, even the least radiogenic MORB glasses are still roughly 2% more radiogenic than the abyssal peridotite average of Snow and Reisberg (1995) ($^{187}Os/^{188}Os = 0.125$). Some have referred to this as the 'Os paradox.' Reasons for these discrepancies may include: 1) modifications to the mantle via fluids and melts derived from a subducting slab (Elthon, 1991; Brandon et al., 1996), 2) actual sampling of old subcontinental

lithospheric mantle (SCLM) (Walker et al., 1989), or 3) the average Os isotopic composition of either abyssal peridotites or MORB is not representative of the bulk upper mantle (Snow and Reisberg, 1995; Walker et al., 2002).

The large Os isotopic range of abyssal peridotites also suggests that the sources of abyssal peridotites may be quite heterogeneous on a global scale. Recent Os isotopic analyses of magmatic sulfides (the predominant carrier of Os) using in situ laser ablation techniques reveal $^{187}Os/^{188}Os$ ratios consistent with a primary mantle origin, such that the presumed effect of seawater on measured Os isotopic compositions may have been previously overestimated (Alard et al., 2005). Nonetheless, extensive serpentinization and seafloor alteration leave few primary petrologic features intact, which also may account for isotopic compositions that are more radiogenic than the average bulk Earth estimates despite the incompatibility of Re during partial melting (Snow and Reisberg, 1995).

Ophiolites represent slices of oceanic lithosphere that have been exposed at the surface through tectonic processes such as obduction. Although originally thought to represent complete slices of oceanic lithosphere, ophiolites – it is now recognized -- can be created at mid-ocean ridge spreading centers as well as at back-arc spreading centers and continental rifts (Elthon, 1991; Tsuru et al., 2000). Unlike MORB and abyssal peridotites, which are < ~100 Ma, ophiolites sample the mantle over a significant portion of Earth history, the oldest (Dongwanzi ophiolite, China) dating back as far as 2.5 Ga. This makes them desirable in the characterization of the convecting upper mantle (and possibly useful in determining the history of plate tectonics). Another advantage in

studying ophiolites is that the upper mantle sections can be collected in situ such that their mantle or lower crustal association remains in spatial context.

The examination of Os and other isotopes in ophiolites is not without challenges. Constraining the amount of alteration is a primary concern insofar as the mantle sections of almost all ophiolites are highly altered, either through mantle metasomatic events or metamorphism associated with tectonic emplacement. Recent studies of dunites in the Troodos Ophiolite Complex, for instance, suggest that Os can behave incompatibly during melt percolation (Büchl et al., 2002; Büchl et al., 2004). Specifically, dunites in a single melt channel from the mantle sequence have significantly enriched Os isotopic compositions ($^{187}Os/^{188}Os_{90Ma}$ = 0.1335-0.1374) relative to carbonaceous chondrites ($^{187}Os/^{188}Os_{90Ma}$ = 0.1264) (Büchl et al., 2002). In contrast, the surrounding harzburgites are only slightly suprachondritic ($^{187}Os/^{188}Os_{90Ma}$ = 0.1288-0.1311), which suggests that Os is dissolved by the melt during melt percolation and mobilized together with the sulfides. Rather than remain in the residue, the Os enters the melt, which could account for the enriched Os isotopic compositions in the dunite vein. This contradicts the standard Re-Os fractionation behavior, and suggests that highly siderophile elements (HSE) like Os can be used as proxies for melting and enrichment processes in the Earth's mantle. Thus, in order to obtain useful isotopic information about primary assemblages, careful examination of the alteration history of the rocks must be undertaken.

In general, there have been few studies of ophiolites using multiple radiogenic isotope systems. This is in part due to the fact that Pb, Sr and Nd are mobilized by melt-fluid interaction so that they are not reliable recorders of primary source heterogeneity. Previous major studies include the Oman ophiolite from the Tethyan suture zone

(Briqueu et al., 1991; Chalot-Prat et al., 2003; Lapierre et al., 2004), the Troodos ophiolite in Cyprus (Rautenschlein et al., 1985), Ligurian ophiolites in the Apennines of Italy (Rampone, 2004) and a few lesser-known ophiolites in Asia.

1-3 Purpose of This Work

In order to better understand the composition and evolution of the Earth's interior, including mantle convection dynamics, it is important to constrain the chemical structure and isotopic heterogeneity of the upper oceanic mantle. One of the primary aims of this study, therefore, is to investigate and document the Os, Nd, Sr and O isotopic variability within a young and well-mapped ophiolite. It may be possible to constrain the causes of isotopic variability in this suite of rocks and precisely relate the isotopic variability to spatial variations in primary lithology. Furthermore, the isotopic composition of Os in the peridotitic rocks may help identify and date mantle processes, such as melt extraction, involved in the formation of the ophiolite, due to the resilience of the Re-Os isotope system to the effects of secondary processes.

Establishing the metamorphic effects that have occurred and in what ways, if any, these have influenced or altered isotopic compositions are essential in identifying the cause of isotopic variability in this suite of rocks. For the same reason, the extent of hydrothermal or surface alteration and whether it has affected the isotopic compositions must be resolved. Specifically, the relationship between Os isotopic compositions for whole rock powders with major and trace element data, such as magnesium numbers and anhydrous aluminum, may reveal information related to melt depletion or post-crystallization effects. In addition, comparison of isotopic compositions of chromite

separates versus whole rock powders may validate or refute the reliability of whole rock data insofar as serpentinization of silicates can cause open-system behavior for Re-Os. Chromite separates may be used to see through serpentinization effects because they are resistant mineral phases within peridotitic rocks and concentrate Os in trace phases. Strontium, Nd and O isotopes should also provide additional insight into the extent and significance of alteration, including crustal contamination and interaction with meteoric and/or seawater.

Interpretation of Os data for old ophiolites may be compromised by post-formation open-system behavior, e.g., recent Re gain or loss. Such effects are particularly exacerbated in mafic rocks that dominate the upper crustal portions of most ophiolites. Study of a very young ophiolite, such as the ~ 6 Ma Taitao Ophiolite in southern Chile should, however, enable comparisons of initial Os isotopic composition between mafic and ultramafic rocks as well as the distribution of Re and Os within the ophiolite. If the initial $^{187}Os/^{188}Os$ of ultramafic and mafic rocks are different, for example, the Os isotopic compositions may reflect original isotopic heterogeneities of the source region. Previous attempts to compare Os isotopic compositions of ultramafic and mafic rocks have proven contentious in that the age corrections associated with much older ophiolitic bodies have resulted in significant errors. Therefore, determining the level of isotopic variability within a very young ophiolite such as Taitao as well as constraining the causes of heterogeneities found therein remains critical for full interpretation of the convecting upper oceanic mantle.

CHAPTER 2: STUDY SITE AND SAMPLE DESCRIPTION

2-1 Regional Geology

The Taitao ophiolite is located on the Taitao Peninsula, which is the westernmost promontory of the Chilean coast and approximately 50 km south of the present-day Chile Triple Junction (CTJ) (Bourgois et al., 1996). Presently, the CTJ is situated at 46°12'S and represents the junction of the Nazca, Antarctic, and South American plates in a ridge-trench-trench configuration (Guivel et al., 1999). Global plate tectonic reconstructions show that the convergence of the Nazca plate has been constant with respect to the South American plate towards N85°-90°E and moved with a nearly steady velocity of 8.5 cm/yr. Meanwhile, the Antarctic plate has maintained an eastward convergence velocity of 2 cm/yr during the last 10 Ma (Cande and Leslie, 1986). Based on the oblique configuration of the Taitao Ridge (a submarine promontory north of the Taitao Peninsula and possible nascent ophiolite; Lagabrielle et al., 2000) with respect to the Peru-Chile trench axis, the CTJ is thought to have migrated with relatively high velocity from south to north in the last 14 Ma as the ridge subducted (Guivel et al., 1999). Periods of slow, southward migration, on the other hand, are thought to have occurred when a fracture zone in the Chile Ridge system subducted (Cande and Leslie, 1986; Lagabrielle et al., 2000).

According to the 1972 Penrose Conference on Ophiolites, a typical ophiolite sequence is defined as a specific association of ultramafic, mafic and sedimentary rocks that become tectonically emplaced in a continental setting. Following this guideline, the Taitao ophiolite is a pseudo-stratified classic Penrose sequence with basal mantle peridotites overlain by gabbros, doleritic dikes, pillow lavas and sediments (Figure 2-1).

The ultramafic rocks consist mainly of harzburgites and a minor amount of lherzolites and dunites (Nelson et al., 1993). They are predominantly deformed and serpentinized, with foliations trending NW-SE to EW (Veloso et al., 2005). Geochemical uniformity and light rare earth element (LREE) depletions suggest that these rocks developed as partial melting residues formed within the mantle rather than as cumulates (Kaeding et al., 1990). Furthermore, major and trace element compositions are consistent with other ophiolites (Kaeding et al., 1990).

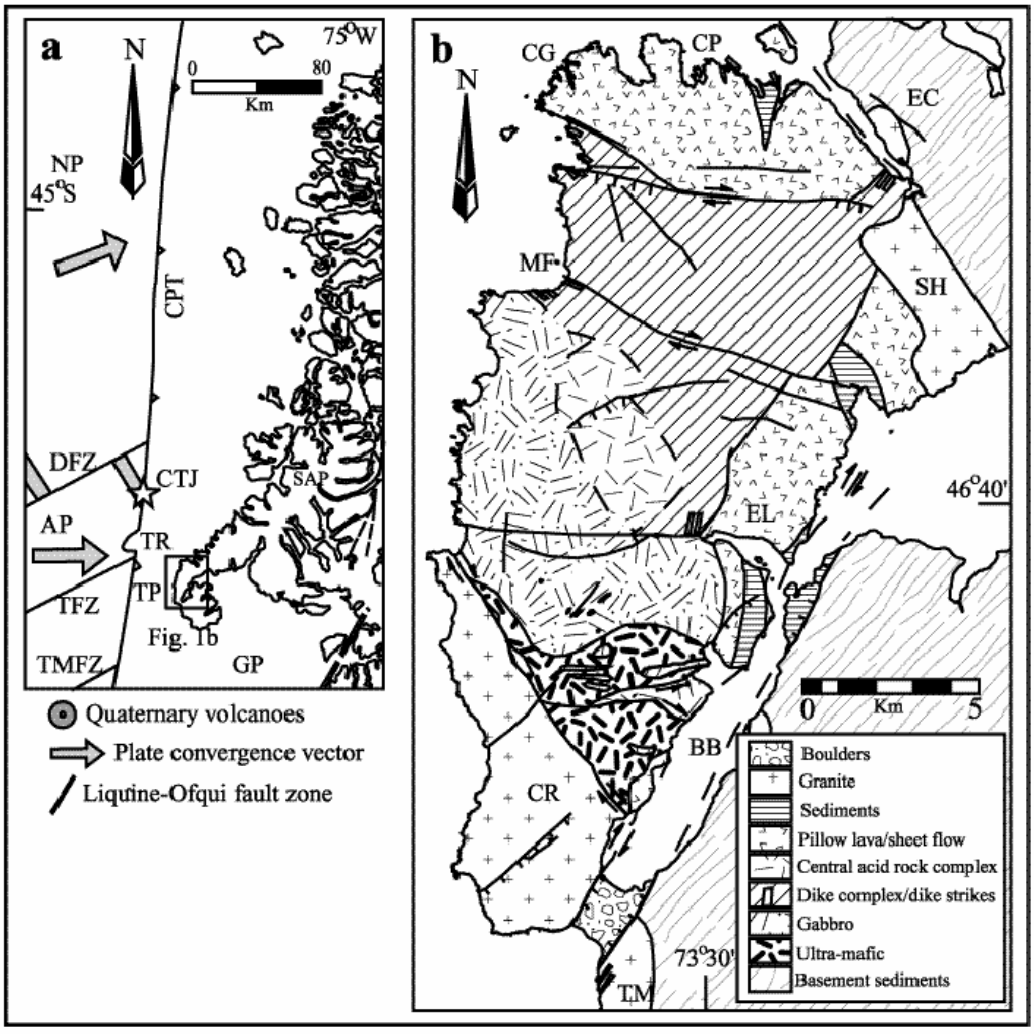

Figure 2-1. Geology of the Taitao Ophiolite (from: Veloso et al., 2005)

The gabbroic rocks are also LREE-depleted. This characteristic, together with petrography, suggests a cumulate origin (Kaeding et al., 1990). Distribution of layered and massive gabbros occurs widely in the north of the ultramafic rock section (Guivel et al., 1999). The layered gabbros mainly strike in the ENE-WSW direction (Veloso et al., 2005). Gabbros also occur as dikes that intrude into the ultramafic rocks. The estimated total thickness of the gabbros is 4-5 km (Nelson et al., 1993). The ultramafic rocks and gabbros share most boundaries, some of which are faulted, and both have complex folds about sub-horizontal axes (Veloso et al., 2005). Intrusive contact relationships are observed in a few outcrops, such that intruding gabbroic dikes do not disrupt basal contacts with the ultramafic rocks.

The sheeted dike complex (Bimodal Dike Complex (BDC); Guivel et al., 1999) possesses bimodal compositions, with mafic to intermediate lavas (48-56% SiO_2) and acidic lavas ranging from dacites to rhyolites (66-73% SiO_2), and lies on top of the gabbro section, with proportions of the dikes increasing toward the north (Guivel et al., 1999; Lagabrielle et al., 2000). Contacts between gabbros and the sheeted dike complex appear gradual and, in general, maintain primary relationships (Veloso et al., 2005). The unit exhibits minor normal faults.

A volcani-clastic sequence known as the Main Volcanic Unit (MVU) is widely distributed to the north and mainly composed of pillow lavas, pillow breccias and sediments, with frequent observations of normal faulting (Guivel et al., 1999; Veloso et al., 2005). Based on sedimentary facies analyses, the MVU accumulated in a shallow submarine environment and later developed a greenschist metamorphic overprint (Guivel et al., 1999; Nelson et al., 1993). The Chile Margin Unit (CMU), another section of

volcani-clastic rocks, extends along the Bahia Barrientos fault zone, which is located along the eastern border of the Taitao ophiolite. The CMU consists of interbedded sedimentary and volcanic material also deposited in a shallow water environment. Lava flows in the MVU and CMU record a large range of compositions including Normal-MORB (N-MORB), Enriched-MORB (E-MORB), and calc-alkaline lavas; and are likely to have originated from the buried active spreading center during subduction at shallow depth (Guivel et al., 1999).

The Bahia Barrientos fault zone creates an uncomformable boundary between the ophiolitic body and the Pre-Jurassic basement (Veloso et al., 2005). Metasediments comprise the bulk of the Pre-Jurassic basement rock, with metamorphic grades ranging from greenschist to amphibolite facies (Davidson et al., 1987). For the purposes of this study, however, only the ultramafic and gabbroic sections of the ophiolite outcrop are examined.

Previous studies in the CTJ region suggest that subduction of the Chile Ridge beneath the South American continental margin was contemporaneous with the emplacement of magmatic suites and possibly ophiolite obduction close to the trench axis (Guivel et al., 1999). Major, trace and rare earth element geochemical data and geophysical proximity to the CTJ, in addition to the Sr and Nd isotopic data, also suggest that the Taitao ophiolite formed in a suprasubduction zone (SSZ) setting. Specifically, Kaeding et al. (1990) reported that Sr and Nd isotopic data for mafic dikes and volcanic units are consistent with that of modern oceanic suites; although, Nd isotopic compositions are greater in range than typical MORB ($^{143}Nd/^{144}Nd$ varies from 0.512867 to 0.513134; ε_{Nd} from +4.5 to +9.7, respectively). The documented range could also be

due to original heterogeneity in the mantle source, since the concentration of Nd in meteoric and seawater is so small that no bulk or isotopic re-equilibration takes place. More importantly, when plotted on a Nd-Sr correlation diagram, the basaltic units lie along a mixing curve between the gabbros and either forearc sediment or metamorphic basement, supporting 10-25% or 5-10% assimilation.

Overall, Sr ratios indicate little exchange with seawater ($^{87}Sr/^{86}Sr$ isotopic compositions range from 0.702650 in samples interpreted to be N-MORB to 0.704394 in those considered to be evolved, calc-alkaline magmas; Guivel et al., 1999) and support the idea of a primary magmatic origin for the anomalously high Na and Ti contents of the mafic rocks (Kaeding et al, 1990). Rubidium, Sr and Ba concentrations of mafic dikes are consistent with island arc tholeiite (IAT)-like values, which Kaeding et al. (1990) suggested might be due to alteration. Nickel and Cr contents vary between typical MORB and IAT with Zr contents representative of typical MORB. Most major elements are negatively correlated with SiO_2 except Na_2O and K_2O (Guivel et al., 1999). However, compositional differences at similar SiO_2 concentrations are observed among the basalts. Most of the basalts from the Taitao ophiolite display N-MORB characteristics and are LREE-depleted with $(La/Yb)_N < 1$ and large ion lithophile element (LILE) variations, illustrated by K/Ti ratios that range from 0.03 in an ophiolitic dolerite to 0.6 (Guivel et al., 1999). However, the LILE variations may be secondary due to mobility during alteration and metamorphism.

Geophysically, the ridge-trench-trench (R-T-T) configuration of the CTJ, where active oceanic spreading ridges enter the subduction zone, permits the development of high thermal gradients not found in other forearc regions (Lagabrielle et al., 2000). A

given section of the margin may be affected by repeated passage of several ridge segments, such that melting of oceanic rocks can occur at temperatures of 800-900^{o}C and low pressures corresponding to depths of 10-20 km.

Two main magmatic suites characterize the CTJ domain as a result of the unique tectonic geometry, both of which could have subsequently been emplaced within the sediments of the forearc region (or accretionary wedge), and provide additional evidence for ophiolite formation in a SSZ: (1) MORB-type magmas, and (2) calc-alkaline acidic magmas. MORB-type magmas are thought to derive from the buried active spreading center subducted at shallow depths. Calculations using the trace element and isotopic data compiled by Guivel et al., 1999, indicate that partial melting of oceanic crust plus 10-20% of sediments, leaving an amphibole- and plagioclase-rich residue, may account for the genesis of the acidic magmas (Lagabrielle et al., 2000). Deformation in the CTJ forearc domain, such as horizontal displacements and tilting of crustal blocks along a network of strike-slip faults, implies that a tectonic coupling may exist between the upper and lower plates. This coupling may have led to partitioning of the continental lithosphere and tectonic underplating of young oceanic lithosphere below the continental wedge (Lagabrielle et al., 2000).

Klein and Karsten (1995), however, found that trace element signatures in the southern Chile Ridge lavas are anomalous with respect to the majority of MORBs previously sampled. Specifically, several segments of the active Chile Ridge record convergent-margin geochemical characteristics. As a result, the enriched magmas of the Taitao ophiolite may have formed in the spreading ridge environment, not in a SSZ. Furthermore, chromite grains examined in this study have Cr #'s ($Cr^{3+}/(Cr^{3+} + Al^{3+})$)

ranging from ~ 0.3 to ~ 0.6, which is consistent with Type I peridotites generated at mid-ocean ridges (Dick and Bullen, 1984). For this reason, the preferred provenance for the Taitao ophiolite is a mid-ocean spreading ridge.

With respect to other alteration indicators, the $\delta^{18}O$ magma values of basalts range from +6.2 to +6.6 ‰ (Guivel et al., 1999), modestly higher than magmas from Chile Ridge basalts ($\delta^{18}O$ = +5.6 to +6.0 ‰; Sherman et al., 1997) and typical mantle $\delta^{18}O$ magma values of +5.7 ± 0.3 ‰. Stern et al. (1976) examined the oxygen isotopes of several southern Chilean ophiolites, including the Taitao ophiolite, and reported that the underlying, least altered gabbros record $\delta^{18}O$ of ~ 6.5‰, also consistent with a primary magmatic origin rather than secondary hydrothermal or contact metamorphism due to the circulation of seawater or tectonic activity associated with the spreading center.

Previous attempts to constrain the absolute age of the Taitao ophiolite have produced different results. Guivel et al. (1999) obtained $^{40}Ar/^{39}Ar$ age data from lower plutonic rocks that crosscut the ophiolite indicating that the obduction event may have occurred at ~ 6-7 Ma. Plio-Pleistocene foraminifera sediments interbedded with the upper volcanic rocks, determined by K/Ar methods, suggest 2.5-5.5 Ma as the date of formation (Elthon, 1998). However, large uncertainties exist for the K/Ar dates due to the influence of excess argon inherent in this technique. Recent sensitive high mass-resolution ion microprobe (SHRIMP) U-Pb and fission-track (FT) data of zircons from hornblende-bearing gabbros reveal absolute ages of 5.9 +/- 0.4 and 5.6 +/- 0.1 Ma (Anma et al., 2006). These ages validate previous conclusions regarding emplacement of the ophiolite during Chile Ridge collision events, starting at around 6 Ma, and further support the necessity for both ridge collision and ridge subduction events in generating the

magmatic rocks (Cande and Leslie, 1986; Guivel et al., 1999, Anma et al., 2006). Based on the reliability and precision of the recent zircon data and due to the analytical uncertainties in the K/Ar dates, the age of the ophiolite used in this study is ~6 Ma.

2-2 Sample Descriptions

The 16 mafic and 22 ultramafic samples examined in this study were selected from more than 350 rocks collected by Prof. R. Anma of Tsukuba University and Prof. S. Maruyama and Dr. T. Komiya at the Tokyo Institute of Technology during their 2000-2001 and 2002-2003 Japanese Taitao expeditions. The samples examined here were chosen based on both thin section analysis and hand sample inspection, for their least-altered appearance as well as olivine and chromite abundance (Appendix 1). Sample distributions within the ultramafic and mafic portions of the ophiolite also contributed to their choice in order to more fully characterize the ophiolite.

The samples from the ultramafic portion of the ophiolite were collected from the entire areal extent of the outcrop. The ultramafic samples range from highly serpentinized (as much as 98% secondary minerals) with little to no primary olivine remaining, to moderately serpentinized (40-60% secondary minerals) with moderately abundant (20%) and well-preserved olivine crystals. All of the ultramafic samples fall within the general peridotite field of the olivine-orthopyroxene-clinopyroxene IUGS triangle with original olivine contents greater than 50%. The majority of samples are lherzolites, having 10-40% pyroxene content and 60-90% olivine, though a few samples are harzburgites. Those samples with fabrics reflecting deformation are also termed tectonites. Overall, the peridotites contain variable amounts of chromium spinel

(chromite), orthopyroxene (mostly enstatite, occasionally oikocrystic), and clinopyroxene. Chromite grains are largely subhedral to anhedral with lacy or feathery edges and reddish-brown interiors that are interwoven and rimmed with darker, more Fe-rich chromite veins. Orthopyroxene crystals sometimes contain kinkbands, which suggests minor metamorphism. The rims of a few orthopyroxene grains have also been replaced with clinopyroxene or hornblende. Secondary minerals in these samples include serpentine, amphibole (usually hornblende or actinolite), talc and opaque minerals such as magnetite.

The mafic samples consist of medium- to coarse-grained gabbros from the Gabbro Zone of the ophiolite, some with layered- or weakly-foliated fabrics, basalts, and dikes that are randomly distributed throughout the mafic and ultramafic portions of the ophiolite. The layered gabbros commonly have well-preserved igneous sedimentary structures such as grading and cross-laminations (Veloso et al., 2005). Groundmass minerals mostly include plagioclase, pyroxene and quartz with minor amounts of opaque minerals and occasionally hornblende. Seritization of plagioclase grains is apparent in most samples. Plagioclase also often displays myrmekitic texture or is replaced by epidote or chlorite in variable quantities. Clinopyroxene crystals in coarse-grained gabbros have randomly been replaced by hornblende and actinolite around the rims. Clinopyroxene grains additionally display kinkbands in one or two samples, particularly those with other metamorphic features. Secondary magnetite precipitated along cleavage planes in pyroxene and amphiboles. Other secondary minerals such as titanite, chlorite, and prehnite can also be found. The olivine gabbros contain highly fractured olivine with a skeletal network of secondary magnetite and a minor amount of serpentine. Due to the

absence of garnet and the occasional presence of actinolite and epidote, these metagabbros lie predominantly in the greenschist facies with crossover into the amphibolite facies in those samples that contain abundant hornblende. Additionally, amphiboles in the moderately metamorphosed mafic rocks are complexly zoned and frequently display undulose extinction.

The mafic dikes analyzed in this study are located in the ultramafic and gabbroic sections of the ophiolite rather than the sheeted dike complex itself, mostly due to the fact that the dike complex is largely inaccessible such that few samples from this section were obtained. Most of the dikes are rich in clinopyroxene (as much as 80%). Other minerals include amphibole, olivine, plagioclase, serpentine, and epidote. A few basalts, including basaltic dikes and pods within a mafic or ultramafic host, were selected to aid in a more complete geochemical characterization of the ophiolite. The basalts are aphanitic with plagioclase phenocrysts that are euhedral, tabular in habit, and range in size from 0.25 mm to 1 mm.

Two specimens (TPH065 and TPH069) sample across boundaries between the ultramafic and gabbroic sections of the ophiolite, which places them in a separate category and may require a complex interpretation of their isotopic compositions. For this reason, they have been excluded from the discussion. To obtain further details on mineral abundances, kinematic features and overall characterization of the samples, please refer to Appendix 2 for full petrographic descriptions and associated thin section photographs.

CHAPTER 3: ANALYTICAL METHODS

3-1 Re-Os Isotopic Analysis

Following previously published methods of Shirey and Walker (1995) for Re-Os analysis, approximately 2-3 g of finely ground whole rock powder was dissolved with approximately 3 g of concentrated HCl and approximately 6 g of concentrated HNO_3 and equilibrated with Re-Os spikes in Pyrex Carius tubes. The tubes were subsequently frozen in a dry ice-ethanol slush, sealed with an oxygen-propane torch, and heated to 240^{o}C for approximately 3 days, rotating at least once during the 72-hour period to facilitate sample digestion. Upon cooling and opening the tubes, 3 ml of carbon tetrachloride was added to the acid mixture to extract Os from the aqueous phase (Shirey and Walker, 1995). Reduction of the Os tetraoxide ensued by mixing with approximately 4 ml concentrated hydrobromic acid. Final Os separation and purification was achieved via microdistillation (Birck et al., 1997). Rhenium was extracted from the residual aqua regia solution and purified via anion exchange chromatography using Eichrom AG1X8 anion exchange resin.

To examine the robustness of the chemical digestion process, most of the peridotites were analyzed using both high temperature (340^{o}C) and regular temperature (240^{o}C) digestion techniques (e.g., Shirey and Walker, 1995). The data obtained using low temperature digestion techniques are listed in bold (Table 4-5 in Results), though agreement between the values is excellent (0.5% or better).

Osmium isotopic compositions were measured via negative thermal ionization mass spectrometry (N-TIMS) at the University of Maryland, College Park (UMCP).

Osmium in the ultramafic samples was measured in static mode using seven Faraday cups on a VG-Sector 54 mass spectrometer. Generally, 100 mV to 1V of signal was obtained on mass 240 ($^{192}Os^{16}O_3^-$), as this is the most abundant Os peak. Osmium blanks and samples with low Os abundances (i.e., gabbros and basalts) were measured in negative polarity using an ETP discrete dynode electron multiplier using the NBS Bobcat mass spectrometer in the TIMS laboratory at UMCP, which was modernized from its original 1960's design with a NIST parametric electrometer and an HP voltmeter. The sample was loaded onto a Pt filament in approximately 0.6-0.8 μl of concentrated HBr and dried. The filament was loaded into the mass spectrometer and heated to ~ 860^{o}C. Osmium analysis began when ~10,000 counts per second registered on mass 238 (or 1,000 counts per second on mass 235).

Rhenium was measured using two electron multipliers in a static data collection mode using the NuPlasma multi-collector inductively coupled plasma mass spectrometer (ICP-MS) at UMCP. The purified Re samples were diluted in a 2% nitric acid solution before introducing into the nebulizer. The solution was aspirated into the argon plasma, which provided the source for the ions. A minimum of 2-3 mV on ^{185}Re was obtained for each sample in order to ensure reliable statistics. Likewise, further dilution of the sample solutions was necessary when the signal on ^{185}Re exceeded $3x10^5$ counts per second. The intake tube was washed between samples with a pure 2% nitric solution to remove contamination from previous samples. A mass-fractionation correction factor was applied to the $^{185}Re/^{187}Re$ ratios based on averaged measurements of a 200 ppt Re standard solution. Rhenium concentrations in two ultramafic rocks, TPG001 and TPG068, were extremely high and most likely due to contamination from drilling.

Total analytical blanks averaged 2.0 pg for Os and 3.2 pg for Re. The $^{187}Os/^{188}Os$ of the Os blank averaged 0.179. Blank corrections were negligible (<< 1%) for most Os analyses and minor (0.8% or better) for most Re analyses. Analytical uncertainties in $^{187}Os/^{188}Os$ were generally ± 0.1% ($2\sigma_m$) or better based on repeated analyses of comparable quantities of a standard analyzed with the VG Sector 54 multiplier and Faraday cups, and ± 0.2% ($2\sigma_m$) with the NBS Bobcat mass spectrometer. Analytical uncertainties for Re were typically ± 2% ($2\sigma_m$).

Table 3-1. Total Analytical Blank (TAB) Data. 2SDM% represents the percent of standard deviation of the mean at the 2σ level.

TAB	Re (pg)	Os (pg)	$^{187}Os/^{188}Os$
6/7/2004	2.0	2.0	0.174
7/5/2004	0.3	1.6	0.205
2/9/2005	7.4	2.08	0.161
1/6/2005		2.07	0.172
1/6/2005		2.28	0.178
2/27/2006		3.06	0.147

Table 3-2. Osmium standard analyses for VG Sector 54 TIMS. FC - Faraday cup. 2SDM% represents the percent of standard deviation of the mean at the 2σ level.

	$^{187}Os/^{188}Os$	2SDM	$^{186}Os/^{188}Os$	2SDM	$^{190}Os/^{188}Os$	2SDM	$^{189}Os/^{188}Os$	2SDM
VG Sector 54								
7/12/2004	0.11380	0.00105	0.11992	0.00048	1.9837	0.0001	1.21976	0.00007
11/10/2004	0.11380	0.00035	0.11986	0.00016	1.9837	0.0000	1.21977	0.00004
11/11/2004	0.11383	0.00025	0.11985	0.00012	1.9837	0.0000	1.21980	0.00003
2/23/2005	0.11383	0.00043	0.11989	0.00020	1.9838	0.0000	1.21978	0.00004
1/16/2005	0.11377	0.00148	0.11980	0.00046	1.9836	0.0001	1.21967	0.00009
1/18/2005	0.11398	0.00120	0.11988	0.00049	1.9838	0.0001	1.21979	0.00008
1/14/2005	0.11383	0.00022	0.11986	0.00010	1.9837	0.0000	1.21980	0.00002
	0.11391	0.00105	0.11983	0.00048	1.9836	0.0001	1.21975	0.00007
1/27/2006	0.11362	0.00184	0.11969	0.00170	1.9829	0.0006	1.21939	0.00076
1/27/2006	0.11384	0.00026	0.11986	0.00012	1.9834	0.0000	1.21975	0.00003
Average	0.11383	0.00081	0.11983	0.00043	1.9835	0.0001	1.21970	0.00012

Table 3-3. Osmium standard analyses for NBS Bobcat TIMS. 2SDM% represents the percent of standard deviation of the mean at the 2σ level.

	$^{187}Os/^{188}Os$	2SDM	$^{190}Os/^{188}Os$	2SDM	$^{192}Os/^{188}Os$	2SDM
NBS Bobcat						
7/20/2004	0.11411	0.00137	1.9830	0.0005	3.0743	0.0005
7/15/2004	0.11392	0.00152	1.9855	0.0008	3.0616	0.0013
6/25/2004	0.11374	0.00190	1.9825	0.0008	3.0679	0.0012
	0.11393	0.00239	1.9851	0.0014	3.0524	0.0020
	0.11469	0.00120	1.9813	0.0005	3.0364	0.0007
1/10/2006	0.11394	0.00233	1.9817	0.0008	3.0454	0.0009
Average	0.11406	0.00178	1.98319	0.0008	3.05631	0.0011

3-2 Electron Microprobe Analysis

Olivine and chromite grains from most ultramafic samples were analyzed by standard wavelength dispersive spectroscopy (WDS) using a JEOL JXA-8900 electron probe microanalyzer (EPMA) at the University of Maryland Center for Microanalysis. Polished thin sections were coated with ~300Å carbon using standard thermal evaporation techniques. Typically, multiple spots were analyzed, from core to rim, in order to assess within-grain heterogeneity. The following standards were used for chromite analyses: Bushveld Chromite (Mg, Cr, and Fe); Kakanui Hornblende (Al, Si); Ilmen Mountains Ilmenite (Ti, Mn), gahnite (Zn), and Co and Ni metals. Standards employed for the olivine analyses include: fosterite (Fo90; Mg, Fe, Ni, Si), hypersthene (Ca, Cr, Al), rhodonite (Mn) and Co. Secondary standards consisted of a variety of standard minerals. Statistical uncertainties for olivine in the peridotite samples were 0.6% for MgO, 21% for CaO, 0.5% for SiO_2, 1.5% for FeO and 13% for NiO (Table 3-4). The percent deviation of these oxides from accepted values is 0.01% for MgO, 0.15% for SiO_2, 0.73% for FeO, and 1.4% for NiO. Statistical uncertainty for chromite grains were 0.6% for MgO, 0.9% for Al_2O_3, 0.7% for Cr_2O_3, and 0.2% for FeO (Table 3-5).

Operating conditions were as follows: accelerating voltage of 15.0 kV, sample current of 50 nA (chromite) or 20 nA (olivine), 3 mm beam diameter, and peak and background count times of up to 60 seconds. X-ray intensities were corrected using the CIT-ZAF algorithm.

Table 3-4. Forsterite Fo90 primary olivine standard over a one week period. STD represents "standard deviation," and is determined at the 1 σ level.

Fo (90) Standard	**MgO**	**CoO**	**Al_2O_3**	**CaO**	**SiO_2**	**MnO**	**Cr_2O_3**	**FeO**	**NiO**	**Total**
OL-080204	48.99	0.053	0.00	0.10	40.45	0.08	0.02	9.69	0.44	99.83
OL-080204	49.18	0.033	0.01	0.10	40.63	0.09	0.01	9.26	0.37	99.68
OL-080204	49.63	0.044	0.05	0.15	40.71	0.09	0.00	9.51	0.38	100.56
OL-080204	49.40	0.035	0.02	0.12	40.80	0.08	0.02	9.63	0.30	100.39
OL-080204	49.27	0.038	0.00	0.08	40.79	0.09	0.02	9.59	0.41	100.30
OL-080204	49.47	0.028	0.01	0.13	40.97	0.07	0.02	9.57	0.29	100.56
OL-080304	49.60	0.046	0.00	0.10	40.71	0.08	0.00	9.40	0.38	100.33
OL-080304	48.93	0.036	0.01	0.11	41.00	0.11	0.01	9.59	0.34	100.14
OL-080304	49.64	0.012	0.00	0.10	40.89	0.08	0.00	9.30	0.30	100.32
OL-080304	49.47	0.061	0.00	0.17	40.94	0.09	0.03	9.57	0.38	100.71
OL-080304	49.62	0.044	0.01	0.12	40.91	0.12	0.00	9.44	0.41	100.66
OL-080404	49.18	0.040	0.04	0.09	40.99	0.07	0.01	9.36	0.40	100.17
OL-080404	49.31	0.051	0.01	0.09	40.83	0.10	0.03	9.36	0.34	100.12
OL-080404	49.59	0.027	0.04	0.13	40.52	0.10	0.00	9.55	0.41	100.36
OL-080404	49.77	0.046	0.00	0.15	40.70	0.08	0.00	9.62	0.37	100.75
OL-080404	49.68	0.001	0.02	0.10	40.69	0.06	0.00	9.62	0.46	100.63
OL-080504	49.72	0.016	0.01	0.11	40.47	0.10	0.00	9.40	0.33	100.14
OL-080504	49.65	0.028	0.04	0.08	41.00	0.09	0.00	9.29	0.47	100.64
OL-080504	48.78	0.013	0.00	0.10	40.39	0.11	0.00	9.25	0.36	99.00
OL-080504	49.39	0.058	0.02	0.11	40.61	0.09	0.01	9.59	0.36	100.24
AVG	**49.41**	**0.04**	**0.01**	**0.11**	**40.75**	**0.09**	**0.01**	**9.48**	**0.38**	**100.28**
STD	0.28	0.02	0.02	0.02	0.19	0.01	0.01	0.14	0.05	0.41
Accepted Composition	**49.42**				**40.81**	**0.14**		**9.55**	**0.37**	**100.29**
% Deviation	0.01%				0.15%	-36%		0.73%	1.4%	0.01%

Table 3-5. Bushveld chromite standard. STD stands for "standard deviation" and is reported at the 1 σ level.

Standard	MgO	CoO	Al_2O_3	MnO	SiO_2	Cr_2O_3	ZnO	NiO	FeO	TiO_2	Total
BUSH	10.71	0.05	15.0	0.40	0.00	45.9	0.06	0.09	25.49	0.56	98.2
BUSH	10.70	0.07	15.1	0.45	0.00	46.3	0.08	0.11	25.55	0.56	99.0
BUSH	10.55	0.07	14.9	0.41	0.00	46.1	0.06	0.07	25.59	0.53	98.2
BUSH	10.63	0.08	15.0	0.45	0.00	46.5	0.05	0.10	25.62	0.49	99.0
BUSH	10.67	0.06	14.8	0.43	0.00	46.6	0.09	0.10	25.55	0.50	98.9
Average	**10.65**	**0.07**	**15.0**	**0.43**	**0.00**	**46.3**	**0.07**	**0.09**	**25.56**	**0.53**	**98.6**
STD	0.06	0.01	0.1	0.03	0.00	0.3	0.01	0.01	0.05	0.03	0.4

3-3 XRF Analysis

Whole rock mafic and ultramafic samples were crushed in an agate chamber shatter box to grain sizes < 80-mesh sieve screen. Approximately 10 g of powdered rock was then weighed and sent to Stan Mertzman at Franklin & Marshall College in Lancaster, PA, for major and trace element analyses via X-ray fluorescence (XRF). The methodology used for XRF analysis has been described at length elsewhere (Boyd and Mertzman, 1987). To summarize, 0.4000 ± 0.0001 g of rock powder is added to 3.6000 ± 0.0002 g lithium tetraborate, mixed for 10 minutes and transferred into a 25 cc. 95% Pt-5% Au crucible. Approximately 3 drops of a 2 % solution of LiI is then added to the powder to reduce the viscosity of the resulting mixture. The crucible is subsequently heated and covered with a lid, into which the molten sample is poured and cast. The side of the disc in contact with the Pt lid is exposed to the primary X-ray beam. The major elements (Si, Ti, Al, Fe, Mn, Mg, Ca, Na, K, P) are measured via this technique, as are Sr, Zr, Cr and V. Trace element analysis is accomplished by weighing out 7.0000 ± 0.0004 grams of whole rock powder, adding 1.4000 ± 0.0002 grams of high purity copolywx powder, mixing for 10 minutes, and pressing the sample into a briquette.

Elements measured in this manner include Rb, Sr, Y, Zr, Nb, Ni, Ga, Cu, Zn, U, Th, Co, Pb, Sc, Cr and V. Lanthanum, Ce, and Ba are calibrated using an L x-ray line and a mass absorption correction.

All data are acquired and reduced using a Philips 2404 X-ray fluorescence vacuum spectrometer, which is equipped with a 102-position sample changer and a 4 kW Rh x-ray tube. The amount of ferrous Fe is titrated using a modified Reichen and Fahey (1962) method and loss on ignition (LOI) is determined by heating an aliquot of the sample at 950^{o}C for one hour. The x-ray procedure determines the total Fe content as Fe_2O_3T. All major element data were normalized to 100 to account for loss on ignition (LOI) when creating abundance diagrams and comparative graphs. The original data are reported in Table 4-1. Internal reproducibility (2σ) based on repeat analyses of sample 98-54 are 0.12 for Al_2O_3, 0.09 for Fe_2O_3T, 0.93 for MgO, 0.04 for CaO, 16 for V, 3 for Ni, and 1 for Co. The percent deviation of standard BVHO-1 from its accepted values is 0.94% for Al_2O_3, 2.29% for Fe_2O_3T, 1.94% for MgO, 0.18% for CaO, 2% for V, 5% for Ni, and 9% for Co (Table 3-6).

Table 3-6. XRF Standards. Fe_2O_3T stands for Fe_2O_3 total. Specimen 98-54 is a sample repeatedly analyzed at Franklin and Marshall College. BVHO-1 is the name of the standard.

	98-54A	98-54B	98-54C	Average	2 σ	BHVO-1 Measured	BHVO-1 Accepted	% Deviation
SiO_2	51.67	52.08	51.71	51.82	0.45	49.73	49.94	0.42
TiO_2	1.22	1.23	1.22	1.22	0.01	2.72	2.71	0.37
Al_2O_3	18.10	18.15	18.03	18.09	0.12	13.67	13.8	0.94
Fe_2O_3T	8.91	8.96	9.00	8.96	0.09	11.95	12.23	2.29
MnO	0.17	0.17	0.17	0.17	0.00	0.17	0.17	0.00
MgO	5.18	5.21	5.19	5.19	0.03	7.09	7.23	1.94
CaO	7.77	7.81	7.79	7.79	0.04	11.38	11.4	0.18
Na_2O	3.98	3.97	3.96	3.97	0.02	2.41	2.26	6.64
K_2O	1.05	1.04	1.04	1.04	0.01	0.53	0.52	1.92
P_2O_5	0.59	0.59	0.59	0.59	0.00	0.28	0.27	3.70
LOI	1.24	1.19	1.26	1.23	0.07			
Total	99.88	100.4	99.96	100.1	0.6	99.93	100.53	0.60
Rb	8.5	8.5	8.7	8.6	0.23	9.5	11	13.6
Sr	792	789	789	790	3	393	403	2
Y	25.1	25.3	25	25.1	0.3	27.7	27.6	0.4
Zr	130	129	129	129	1	176	179	2
V	200	184	189	191	16	311	317	2
Ni	61	59	58	59	3	115	121	5
Cr	102	83	82	89	23	296	289	2
Nb	8.9	8.7	8.7	8.8	0.2	19.8	19	4.2
Ga	20.7	20.3	20.7	20.6	0.5	21.1	21	0
Cu	76	74	78	76	4	123	136	10
Zn	85	83	83	84	2	101	105	4
Ba	560	576	563	566	17	132	139	5
U	0.5	0.7	0.9	0.7	0.4	0.8	0.4	100
Th	0.6	1.2	0.8	0.9	0.6	1.3	1.1	18.2
Co	31	30	31	31	1	41	45	9
La	19	22	21	21	3	14	16	13
Ce	42	43	42	42	1	36	39	8
Pb	7	8	7	7	1	4	3	33
Sc	22	21	21	21	1	31	32	3

3-4 Olivine Oxygen Isotope Analysis

Olivine separates from the least altered ultramafic samples were carefully handpicked from crushed whole rocks that were sieved using a 150 μm mesh screen. The selected samples were chosen to represent the observed range in whole-rock Os isotopic composition. Examination under a binocular microscope allowed for the elimination of grains containing inclusions, cracks or alteration. Samples of 1.4 to 3.7 mg were loaded into wells of a stainless steel sample stage. This stage was loaded into a reaction cell equipped with a BaF_2 laser window, and sealed with a Viton® O-ring. The reaction cell was heated to 250 ºC and evacuated to a baseline pressure for 5 hours to remove residual water. Prefluorination with bromine pentafluoride (BrF_5) for 24 hours removed remaining water, and evolved oxygen (O_2) was pumped away prior to laser analyses.

CO_2 laser fluorination analyses were subsequently made using a 25-W Synrad Laser with BrF_5 as the fluorinating reagent. Lasing of samples was carried out with ~30 Torr of BrF_5, and laser power was controlled to reduce grain sputtering. Molecular oxygen is formed from forsterite grains by the reaction $Mg_2SiO_4 + BrF_5 \rightarrow O_2$ (g) + Br_2 (g) + MgF_2 (l) + SiF_4 (g). Pressure changes were monitored on a 1000 Torr MKS Baratron head gauge. Lasing time of grains ranged from 4-8 minutes. Upon complete ablation of the grains, residual BrF_5, Br_2, SiF_4, and condensable fluorine compounds were frozen with liquid nitrogen (-196ºC) in a manifold U-trap for 20 minutes. After opening to a second manifold, any residual waste was removed in an additional glass trap, frozen for 10 minutes, and final pressure was monitored on a 10-Torr Baratron head. Pure molecular O_2 was frozen with LN_2 into a cold-finger containing a 13X molecular sieve for 15 minutes, and subsequently sealed from the manifold. Analyte oxygen was then

expanded for 10 minutes into the inlet of a continuous flow gas source Thermofinnigan Delta Plus mass spectrometer at the University of Maryland College Park using 2mm metal capillary tubes (Widom and Farquhar, 2003). The CO_2 laser fluorination analyses of Taitao ultramafic olivines yield an average $\delta^{18}O$ of 5.4 ± 0.1‰.

3-5 Whole Rock Oxygen Isotope Analysis

Oxygen from bulk rock powders was extracted using the BrF_5 method of Clayton and Mayeda (1963) at Indiana University in Bloomington, IN. Approximately 5-6 mg of powdered whole rock sample was loaded into pure nickel reaction tubes (with 60 cm^3 capacity), the weight being chosen so that the amount of reagent will exceed stoichiometric requirements five-fold. The reactions tubes were then transferred into a dry box containing air dried by P_2O_5 and heated for 2 hours at 250°C in the absence of BrF_5 and while open to a high vacuum line to remove any adsorbed air and water from the system. Following the BrF_5-free pretreatment, a cold BrF_5 treatment, occurring for one or more 20-minute intervals, removed minor amounts of oxygen compounds that may have formed on the Ni walls during sample loading. After completion of the pretreatment processes, the Ni-reaction vessels were evacuated, charged with BrF_5, closed off and heated by electrical resistance furnaces. Reactions were typically run at 600-700°C for 12-14 hours. The oxygen was collected and isolated by passing the reaction products through a series of cold traps. Once the quantity of O_2 was measured, oxygen was converted to CO_2 by reaction with a heated graphite disk. The CO_2 was then transferred to a sample tube for transport to the mass spectrometer. Isotopic analyses were made using a Finnigan MAT 525 stable isotope ratio mass spectrometer. Results

are reported in standard delta notation, defined as the deviation in per mil (parts per thousand) of the $^{18}O/^{16}O$ ratio from that in standard mean oceanic water (SMOW). Analytical uncertainty was less than 0.46 ‰ and blanks are less than 1 μmol following these procedures. The value of San Carlos olivine in the Mineralogical Laboratories at Indiana University is 5.4 ± 0.3 ‰.

3-6 Sm-Nd and Rb-Sr Isotope Analyses

Samples weighing between 0.1 and 1 gram were spiked for Sm, Nd, Rb and Sr and then dissolved using HF-HNO_3 by Mary Horan at the Carnegie Institute of Washington. Rubidium, Sr and the REE were separated from the matrix using a BioRad cation exchange resin AG50-Wx8, 200-400 mesh, and 2.5 M HCl (for Rb and Sr) and 4M HCl (for REE) in appropriately-sized Teflon or quartz columns. Rubidium was further purified in Teflon columns using the same resin and 0.5M HCl. Strontium was further purified using Eichrom Sr-specific resin. Samarium and Nd were separated from the bulk REE fraction using 0.21M methyllactic acid on AG50Wx8, 200-400 mesh in NH_4^+ form.

Rubidium was analyzed on a P-54 multicollector ICP-MS using an Apex sample introduction system with desolvation via an actively cooled membrane (ACM). Mass fractionation was corrected by internal normalization to $^{90}Zr/^{91}Zr \equiv 4.588$. Samarium was analyzed on the P-54 with the same sample introduction system; mass fractionation was corrected using $^{147}Sm/^{152}Sm = 0.56081$. Strontium was analyzed on a Thermo Finnigan Triton thermal ionization mass spectrometer using Re filament material onto which a thin film of Ta_2O_5-NaOH-HF activator solution was dried with each sample. The standard SRM 987 gives $^{87}Sr/^{86}Sr = 0.710247$. Neodymium was also measured on the

Triton using Re filament material, with Nd measured as the oxide. The standard JNdi yields $^{143}Nd/^{144}Nd = 0.512102$.

CHAPTER 4: RESULTS

4-1 Major elements

Whole-rock major element compositions of the ultramafic samples (Table 4-1) are compared with the primitive mantle (PM) estimate of McDonough and Sun (1995) in Figure 4-1. All peridotitic whole rocks are depleted in Ti, Al, and Ca, and P relative to PM. Most ultramafic rocks are also depleted in Na, although samples TPB124, TPB120, TPE029, TPE033, TPB116 and TPB127 have concentrations similar to PM. It is important to note that the ferric-ferrous ratio was not determined for seven of the samples. As a result, the total Fe_2O_3 was converted to total FeO, which was then used to calculate the Fe^{2+} content of the ultramafic rocks. More importantly, the normalized abundance diagram (commonly referred to as a "spidergram") reveals that Fe is only slightly depleted relative to the PM estimate (Figure 4-1). Also, none of the ultramafic samples have K above the detection limit of 100 ppm K_2O.

The calculated anhydrous Al_2O_3 contents of the ultramafic samples are much lower than the PM, ranging only from 0.74 to 2.51 wt. %, compared to the PM estimate of ~ 4.4 wt. %. Correlation of Al_2O_3 with MgO suggests that these samples experienced variable, relatively high degrees of partial melt extraction (Figure 4-3). Other melt depletion trends, like MgO versus CaO are only broadly consistent with variable extents of melting. Here, the general scatter is most likely due to mobility of Ca during alteration processes (Figure 4-5). However, the partial melting trend from PM estimate is still roughly preserved and coincident with melting trends recorded by abyssal peridotite data (Brandon et al., 2000; Harvey et al., 2006) and ophiolite peridotite data (Godard et al., 2000).

The lack of a linear correlation in the plot of MgO versus FeO is not surprising given that the concentration of Fe in peridotites depends on the depth at which the melting has occurred and not on the degree of partial melting alone (Figure 4-6). For shallow melts, FeO content will remain at ~ 8% (Walter, 1999). Relatively constant FeO suggests shallow melt extraction. At greater depths, Fe will be preferentially depleted in the residue (Walter, 1999). In the case of the Taitao peridotites, the lack of a linear correlation combined with the slightly depleted FeO contents relative to PM may indicate that the rocks experienced shallow or lower degrees of melting, or it might reflect variable metasomatic overprinting by later melts or fluids. The Mg #'s ($Mg^{2+}/(Mg^{2+} + Fe^{2+})$) for whole rock peridotites vary from 0.906 to 0.924.

Mafic rocks are variable in composition (Table 4-1; Figure 4-2), with most enriched in Ti, Al, Ca, and Na, and depleted in Fe and Mg relative to the PM estimate. Several samples are also depleted in Ti and Na. Four of the mafic rocks have K_2O below the detection limit. The remaining seven samples are variably enriched and depleted in K_2O relative to PM. About half the rocks are depleted in MnO. Mg #'s vary from 0.355 to 0.872, which likely reflects their origin as products of mantle melting.

Table 4-1. Major element oxide compositions of whole rock powders determined by XRF analysis. The abbreviation "dup" means the sample is a duplicate analysis of the preceding sample. N.d. stands for "not determined."

Sample	SiO_2	TiO_2	Al_2O_3	Fe_2O_3	FeO	MnO	MgO	CaO	Na_2O	K_2O	P_2O_5	LOI	Total	Fe_2O_3T	Mg #
Ultramafic Rocks:															
TPB124	38.5	0.05	1.40	8.99		0.14	37.1	0.25	0.39	0.0	0.02	12.9	99.7	8.99	0.906
TPE068	38.5	0.04	0.80	6.84	2.13	0.13	38.1	0.27	0.02	0.0	0.01	13.1	99.9	9.21	0.906
TPB120	39.0	0.02	1.24	8.83		0.14	37.7	1.00	0.38	0.0	0.02	11.2	99.5	8.83	0.909
TPE029	38.5	0.01	1.18	8.85		0.12	37.6	0.12	0.37	0.0	0.02	12.8	99.6	8.85	0.908
TPE033	37.7	0.03	0.79	9.03		0.14	38.9	0.56	0.39	0.0	0.02	12.0	99.6	9.03	0.909
TPG001	38.9	0.02	1.53	8.76		0.15	37.8	0.43	0.38	0.0	0.02	11.6	99.6	8.76	0.909
	39.1	0.02	1.51	5.88	2.39	0.16	37.7	0.43	0.13	0.0	0.03	11.9	99.3	8.54	0.911
TPG049	40.8	0.03	1.34	5.36	2.89	0.13	37.9	0.68	0.01	0.0	0.01	10.6	99.7	8.57	0.912
TPH053	39.3	0.03	1.43	5.59	2.66	0.13	37.8	0.54	0.05	0.0	0.01	12.0	99.5	8.55	0.911
TPB116	38.0	0.02	1.10	8.64		0.14	38.1	0.52	0.37	0.0	0.02	12.7	99.6	8.64	0.911
TPE005	39.5	0.02	0.64	6.28	2.11	0.06	38.2	0.07	0.05	0.0	0.01	12.6	99.6	8.62	0.912
TPB016	38.4	0.02	0.98	4.43	3.81	0.14	38.7	1.15	0.06	0.0	0.01	11.9	99.6	8.66	0.912
TPG091	38.1	0.02	0.91	5.57	2.84	0.13	39.7	0.41	0.01	0.0	0.01	12.5	100.1	8.73	0.914
TPB010	38.6	0.05	1.15	4.31	3.7	0.13	38.6	1.04	0.06	0.0	0.02	12.0	99.5	8.42	0.914
TPG050	43.5	0.04	2.27	3.62	3.66	0.13	36.2	1.15	0.03	0.0	0.01	9.6	100.2	7.69	0.916
TPG036	38.8	0.02	1.26	6.07	1.98	0.12	38.4	0.21	0.05	0.0	0.01	12.6	99.6	8.27	0.915
TPG068	39.2	0.02	1.53	8.21		0.13	38.6	1.55	0.38	0.0	0.02	10.0	99.6	8.21	0.916
	40.1	0.02	1.53	3.74	3.85	0.14	38.0	1.49	0.14	0.0	0.03	10.5	99.5	8.02	0.917
TPB127	38.5	0.01	0.79	8.28		0.13	38.8	0.35	0.35	0.0	0.02	12.3	99.6	8.28	0.916
TPG005	39.6	0.03	1.26	6.59	1.34	0.08	37.9	0.26	0.01	0.0	0.01	13.0	100.1	8.08	0.916
TPE010	38.3	0.02	0.98	4.81	3.01	0.13	39.3	0.32	0.05	0.0	0.01	12.7	99.5	8.16	0.918
TPE024	39.9	0.01	0.99	3.43	3.69	0.12	39.5	0.71	0.06	0.0	0.01	11.4	99.7	7.53	0.924
Contact rocks:															
TPH069	43.7	0.16	4.31	4.89	3.87	0.17	28.7	3.68	0.42	0.0	0.02	9.5	99.5	9.33	0.905
TPE004	38.8	0.01	0.78	9.33		0.09	38.3	0.08	0.39	0.0	0.02	11.8	99.6	8.5	0.912
TPH065	39.5	0.03	1.34	6.34	1.94	0.07	37.9	0.20	0.01	0.0	0.01	12.3	99.7	9.19	0.879
Ultramafic Dike:															

TPE027	47.8	0.12	4.31	1.23	2.75	0.1	23.0	14.6	0.32	0.0	0.02	4.3	98.5	4.29	0.926
Mafic Rocks:															
TPB042	45.1	6.2	10.1	4.96	14.68	0.3	4.9	9.23	2.87	0.0	0.04	1.3	99.6	21.27	0.350
TPB040	48.9	2.5	9.46	3.68	11.04	0.16	9.5	9.73	2.45	0.16	0.03	2.0	99.5	15.95	0.581
TPB039	49.5	1.0	15.6	1.86	6.76	0.15	8.5	11.7	2.42	0.22	0.09	1.7	99.4	9.37	0.679
TPB046	51.9	0.54	16.3	1.63	6.38	0.16	8.0	10.6	2.65	0.01	0.03	1.3	99.4	8.72	0.681
TPE017	47.0	1.1	15.9	0.87	7.43	0.15	8.5	11.0	3.16	0.07	0.10	4.2	99.5	9.13	0.684
TPB023	51.9	1.3	15.5	1.80	4.6	0.05	8.5	11.3	3.22	0.1	0.09	1.1	99.4	6.91	0.742
TPH063	41.9	0.23	14.1	1.24	3.89	0.21	11.2	20.9	0.21	0.0	0.01	5.7	99.6	5.56	0.824
TPE063	42.4	0.21	19.5	0.82	4.33	0.09	12.2	12.9	1.04	0.0	0.01	6.2	99.6	5.63	0.834
TPE062	43.9	0.13	22.6	0.88	3.53	0.07	12.3	11.7	1.26	0.0	0.02	3.2	99.6	4.8	0.856
TPH005	45.5	0.13	19.4	1.24	3.67	0.09	14.0	10.6	1.51	0.03	0.04	3.5	99.7	5.32	0.860
TPE049	45.3	0.05	23.7	0.56	2.92	0.06	10.8	11.8	1.54	0.1	0.03	2.8	99.7	3.81	0.869

Figure 4-1. Abundance diagram (also referred to as a "spidergram") of cation data for ultramafic whole rock (recalculated to anhydrous) and normalized to primitive mantle estimates (McDonough and Sun, 1995; Workman and Hart, 2005).

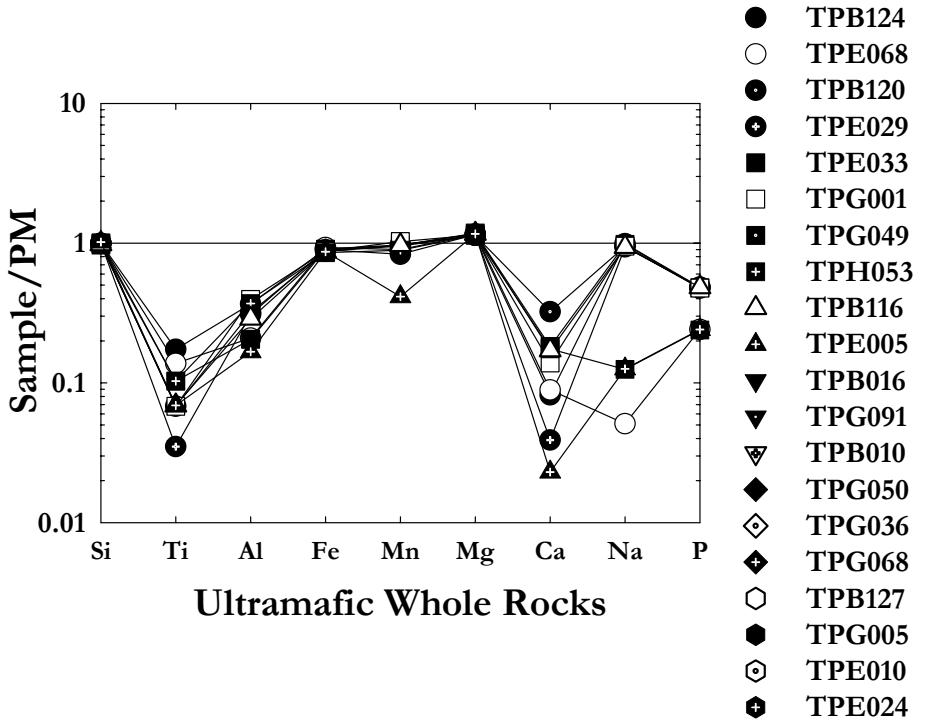

Figure 4-2. Abundance diagram of mafic whole rock cation data (recalculated to anhydrous) normalized to primitive mantle estimates (McDonough and Sun, 1995; Workman and Hart, 2005).

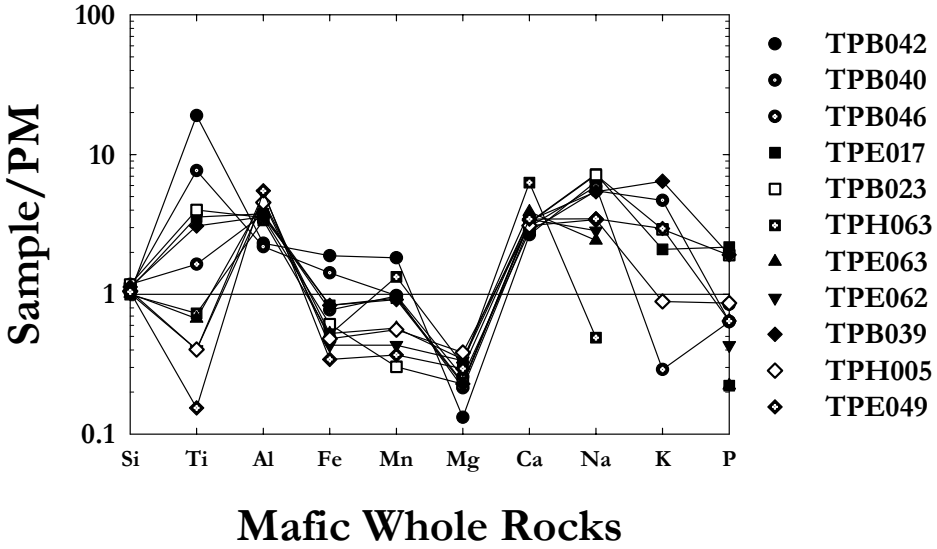

Figure 4-3. Plot of MgO (recalculated to anhydrous) versus Al_2O_3 (recalculated to anhydrous) of Taitao whole rock peridotites (filled circles). □ = PM estimate for MgO and Al_2O_3 (McDonough and Sun, 1995). For this graph and following graphs, Δ = abyssal peridotite data (Brandon et al., 2000); open diamonds (◊) = abyssal peridotite data (Harvey et al., 2006); open downward-pointing triangles = Oman ophiolite peridotites (Godard et al., 2000).

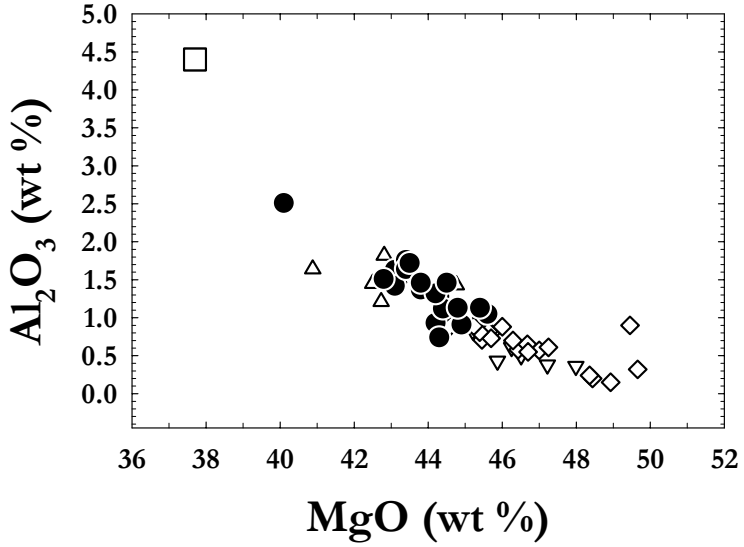

Figure 4-4. Plot of Al_2O_3 (recalculated to anhydrous) versus CaO (recalculated to anhydrous) of Taitao whole rock peridotites (filled circles). □ = PM estimate for Al_2O_3 (McDonough and Sun, 1995) and CaO (Workman and Hart, 2005). See Figure 4-3 for other symbol references.

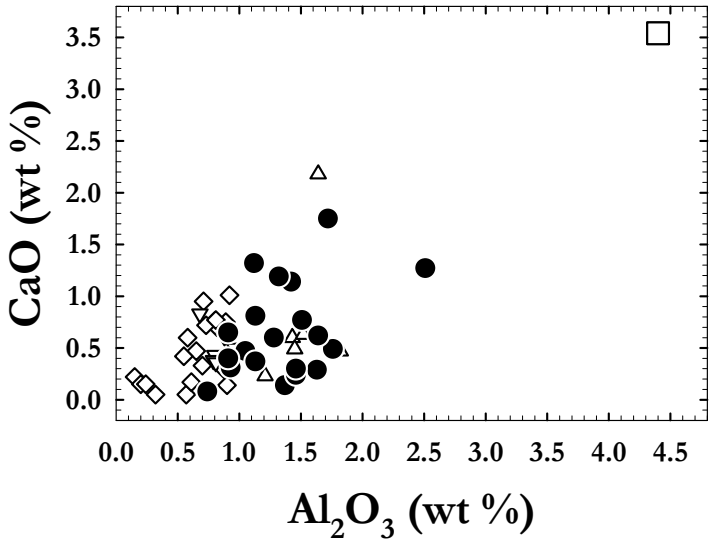

Figure 4-5. Plot of MgO (recalculated to anhydrous) versus CaO of Taitao whole rock peridotites (filled circles). □ = PM estimate for MgO (McDonough and Sun, 1995) and CaO (Workman and Hart, 2005). See Figure 4-3 for other symbol references.

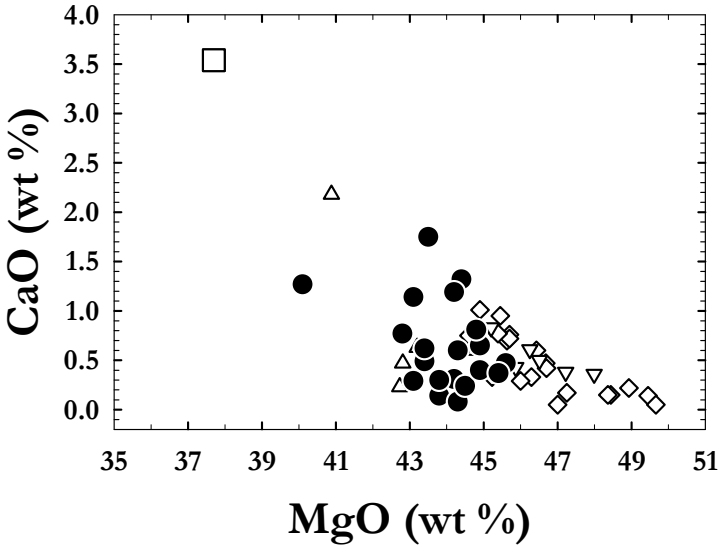

Figure 4-6. Plot of MgO versus FeO_T (both recalculated to anhydrous) of Taitao whole rock peridotites. The open box represents the PM estimate from McDonough and Sun (1995). Open hexagons correspond to peridotite data from the Troodos ophiolite (Büchl et al., 2002 and 2004). See Figure 4-3 for other symbol references.

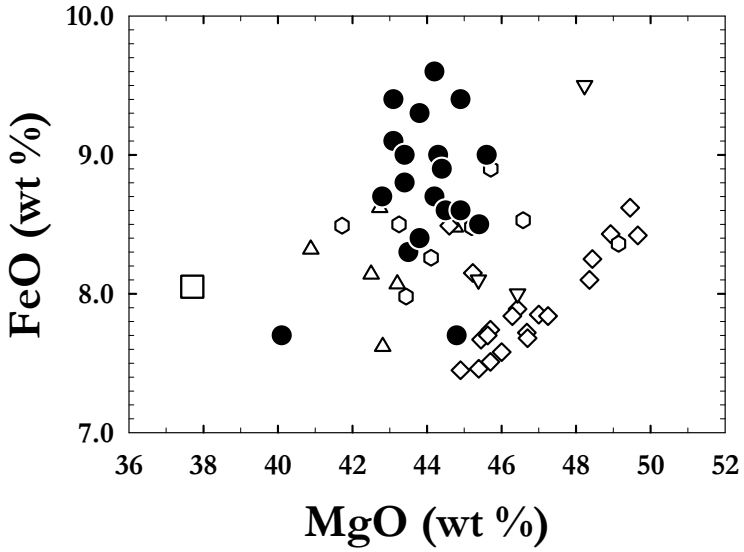

4-2 Trace elements

Table 4-2 provides trace element compositional data for ultramafic and mafic whole rock samples. Concentrations of U, La and Ce are below the detection limit for all peridotites, which are correspondingly 0.5 ppm, 2 ppm and 2 ppm. Nearly all of the ultramafic samples also have Th concentrations below the detection limit of 0.5 ppm. For this reason, these elements have been excluded from the table. The one exception to these trends is TPG091, which contains 0.7 ppm Th.

Most of the peridotitic rocks are enriched in Ba and Pb and depleted in Sr, Y, Cu and Ga relative to PM (Figure 4-8). Exceptions to this include TPG050, which is enriched in Cu, TPG068, which is depleted in Ba and Zr, and TPG001, which is depleted in Zr. Moreover, TPE024 and TPE005 are significantly depleted in Ga while the other peridotitic samples are only moderately depleted in Ga. Incompatible refractory elements, such as vanadium, show a positive correlation with Al_2O_3 (Figure 4-10). Compatible trace elements like Ni and Co mostly scatter in relation to Al_2O_3 and MgO (Figures 4-11, 4-12, 4-13), suggesting serpentinization or other alteration processes have mobilized these elements.

Trace element concentrations of the mafic rocks are more variable and display fewer consistent trends when compared to PM estimates (Figure 4-9). However, the mafic rocks are enriched in Ba, Th, Nb, and Pb. Due to the provenance of these samples, the Ba spike may reflect interaction with seawater or other fluids. Most of these rocks are depleted in Cr, Ni, Co and Zn. The mafic samples also record moderate depletions of Co and Zn. The concentrations of U, La and Ce are generally below the detection limits of 0.5 ppm, 2 ppm and 2 ppm, respectively. These elements have been excluded from the

table. Samples TPB042, TPB040, TPH005 and TPE049 are exceptions in that they have the following trace elemental concentrations: 3 ppm La and 10 ppm Ce (TPB042), 4 ppm La and 12 ppm Ce (TPB040), 3 ppm La and 8 ppm Ce (TPH005), and 2 ppm La and 6 ppm Ce (TPE049).

Table 4-2. Trace element data for whole rock samples determined by XRF analysis. All element concentrations are reported in ppm.

Specimen	Rb	Ba	Nb	Pb	Sr	Zr	Y	Sc	Cr	Cu	Co	Zn	Ni	V	Ga
Ultramafic Rocks:															
TPB124	<0.5	<3	1.3	<1	<1	10	2.5	12	2810	19	97	50	2090	56	1.7
TPE068	1.7	6	1.1	5	7	11	1.8	8	2340	6	106	33	2230	38	0.8
TPB120	<0.5	15	1.3	<1	<1	10	2.1	13	2420	15	96	42	2220	48	1.3
TPE029	<0.5	3	1.6	1	<1	10	2.1	11	2510	23	96	39	2260	50	1.1
TPE033	<0.5	3	1.3	<1	<1	10	2	7	1890	7	101	42	2300	32	0.9
TPG 001	<0.5	5	1.0	<1	4	2	2.2	12	2890	16	98	39	2010	60	<1
TPG049	1.6	5	1.2	7	6	9	1.5	9	2600	7	105	38	2300	42	1.3
TPH053	<0.5	3	1.4	6	1	9	0.7	10	2830	16	96	39	2040	59	0.9
TPB116	<0.5	5	1.5	<1	<1	10	1.4	10	2290	6	84	40	2290	40	1.1
TPE005	<0.5	<3	1.1	5	1	10	0.5	6	1910	<3	95	23	1940	38	<0.5
TPB016	<0.5	<3	1.4	4	1	9	<0.5	8	2410	13	102	39	2110	48	0.6
TPG091	1.6	<5	1.2	6	7	10	0.9	8	2180	6	103	33	2160	37	1.0
TPB010	<0.5	<3	1.5	4	<0.5	14	2.4	9	2450	7	102	38	2090	48	1.0
TPG050	1.6	<5	1.0	6	7	9	1.1	13	3940	313	90	35	1840	67	1.9
TPG036	<0.5	<3	1.1	3	0.7	9	0.9	11	2330	9	93	33	2050	45	1.2
TPG 068	<0.5	<2	1.1	<1	3	2	1.9	12	3060	13	95	40	2040	55	<1
TPB127	<0.5	8	1.3	3	<1	10	1.8	9	2670	<3	93	39	2160	31	0.9
TPG005	1.6	7	1.0	4	10	9	0.9	9	2600	6	100	31	2070	46	1.2
TPE 010	<0.5	<3	1.0	4	<0.5	9	0.5	8	2700	6	98	36	2100	41	0.6
TPE024	<0.5	<3	1.2	5	1	9	0.6	7	2630	<3	92	37	2040	32	<0.5
Contact Rocks:															
TPH069	1.7	5	1.2	4	38	12	3.7	15	1780	305	101	52	1530	66	5.3
TPE004	<0.5	5	1.2	<1	<1	10	1.5	8	2760	<3	95	31	2170	32	0.8
TPH065	1.3	<5	0.9	4	8	9	1.1	9	2830	1	94	25	2060	50	1.5
Ultramafic Dike:															
TPE 027	<0.5	15	1.2	2	5	1	6.3	39	6380	6	40	16	1170	195	1.4
Mafic Rocks:															
TPB 042	2.0	5	1.7	1	88	55	35.7	53	42	50	43	129	6	540	21.8

TPB 040	2.8	25	1.8	2	83	32	63.3	66	86	3	65	27	220	510	16.7
TPB039	4.8	74	3.2	3	162	71	22.9	38	381	37	41	46	127	235	14.4
TPB046	2.1	5	1.9	4	73	32	13.9	34	101	29	41	54	68	174	15.3
TPE017	6.1	316	2.4	2	632	81	26.4	35	318	70	43	64	129	220	12.9
TPB023	2.6	22	3.7	3	186	81	30.0	43	280	9	37	11	161	262	15.7
TPH063	2.5	<10	1.7	5	42	15	7.4	41	186	52	33	44	237	154	9.0
TPE063	2.1	5	1.5	3	105	14	5.9	16	611	369	45	36	410	73	10.6
TPE062	2.4	<5	1.3	4	41	13	3.0	10	122	30	43	28	419	35	10.3
TPH 005	1.5	20	1.1	<1	110	3	3.4	13	420	148	41	29	665	43	7.4
TPE 049	3.8	18	0.9	1	120	2	2.1	9	170	49	27	21	485	12	8.0

Figure 4-7. Abundance diagram for ultramafic whole rock trace element data normalized to primitive mantle estimates (McDonough and Sun, 1995; Workman and Hart, 2005).

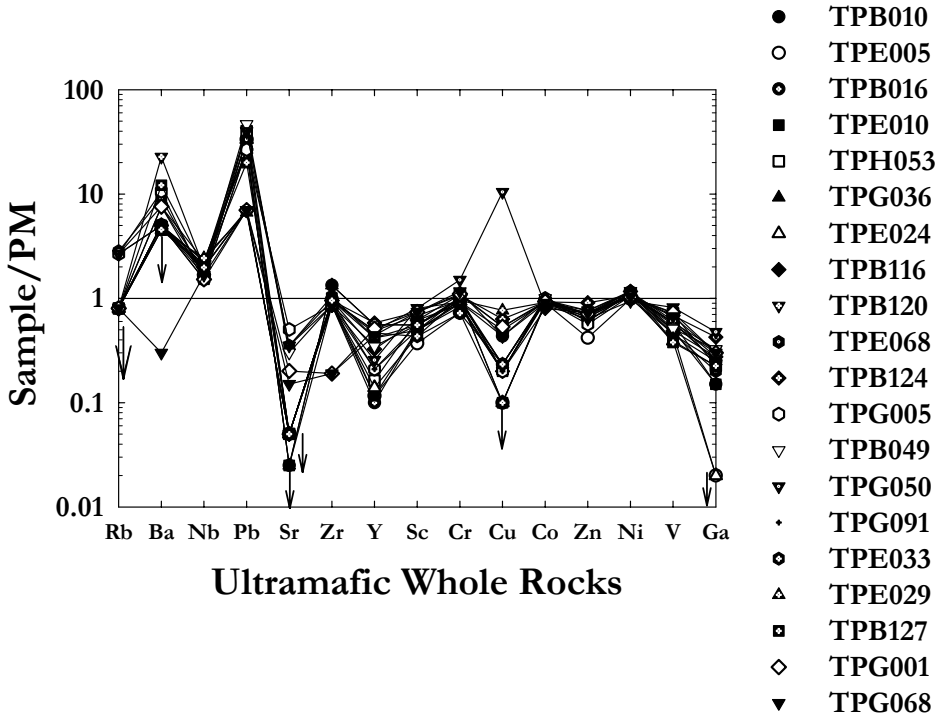

Figure 4-8. Abundance diagram for mafic whole rock trace element data normalized to primitive mantle estimates (McDonough and Sun, 1995; Workman and Hart, 2005).

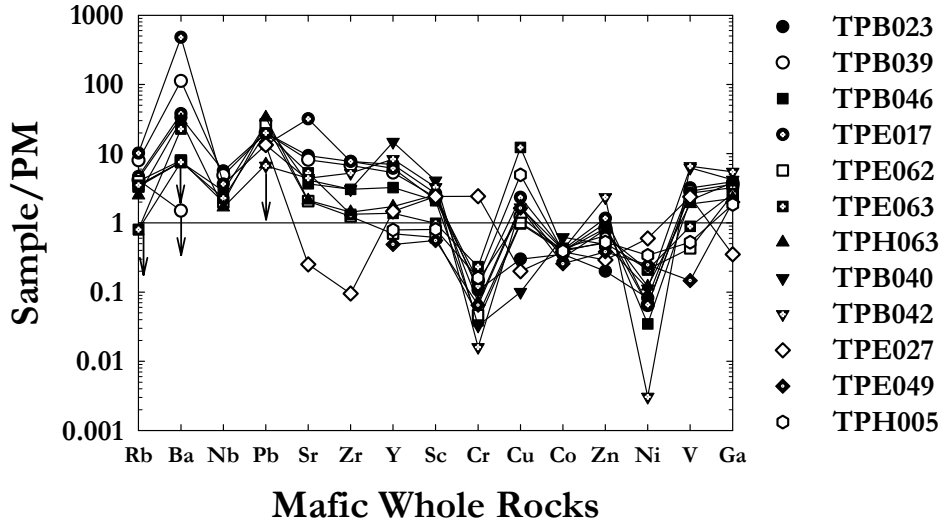

Figure 4-9. Plot of V vs. Al_2O_3 (recalculated to anhydrous) for whole rock peridotite samples. The dashed lines represent the error on the PM estimate for V (McDonough and Sun, 1995).

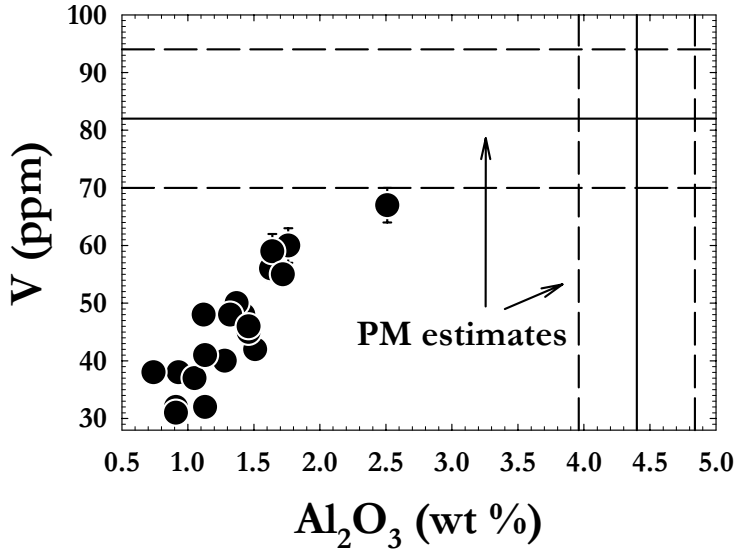

Figure 4-10. Plot of MgO vs. Ni (both recalculated to anhydrous) of Taitao whole rock peridotites (filled circles). The open square represents the PM estimate from McDonough and Sun (1995). Open hexagons correspond to peridotite data from the Troodos ophiolite (Büchl et al., 2002 and 2004). See Figure 4-3 for other symbol references.

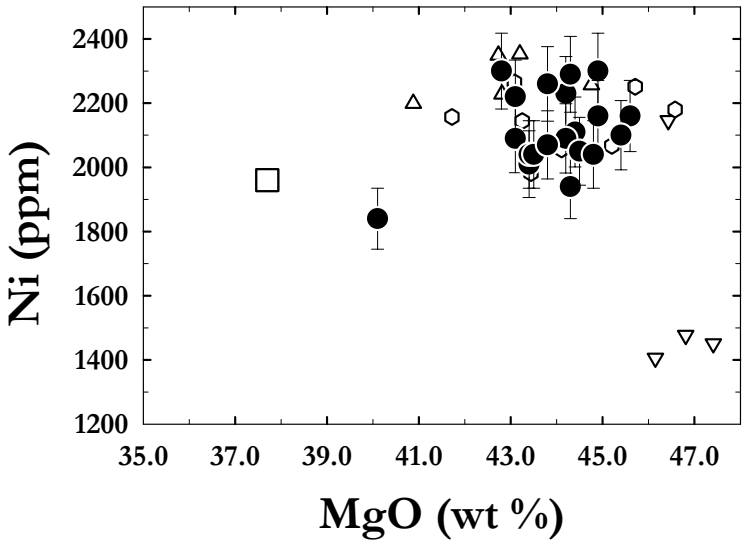

Figure 4-11. Plot of Al_2O_3 (recalculated to anhydrous) versus Ni (recalculated to anhydrous) for whole rock peridotites. The open square represents the PM estimate from McDonough and Sun (1995). Open hexagons correspond to peridotite data from the Troodos ophiolite (Büchl et al., 2002 and 2004). See Figure 4-3 for other symbol references.

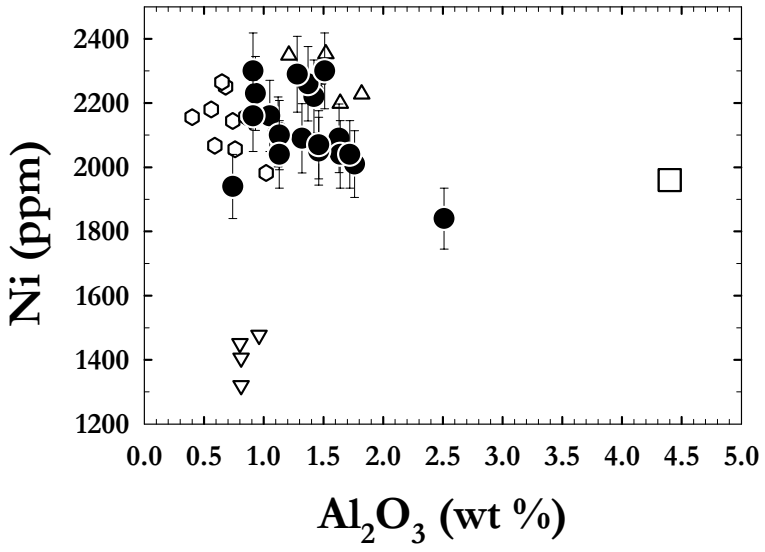

Figure 4-12. Plot of MgO vs. Co (both recalculated to anhydrous) for whole rock peridotites. The open square represents the PM estimate based on McDonough and Sun (1995).

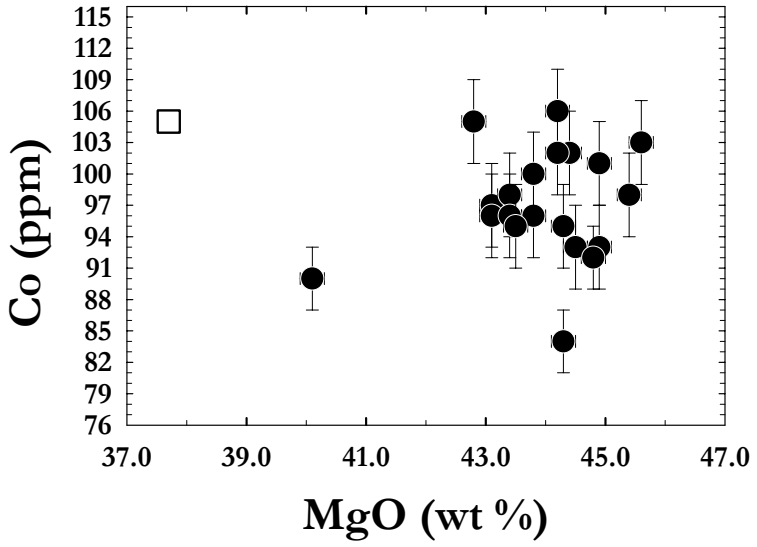

4-3 Olivine and chromite

In order to assess pre-metamorphic compositions and monitor the effects of alteration, polished thin sections were analyzed for olivine and chromite compositions using the electron microprobe. Average major and trace element compositions are provided in Tables 4-3 and 4-4. Most analyses include traverses from rim to core of each olivine and chromite grain analyzed with 2 to 6 points per grain and 4 to 6 grains per rock. Although many of the olivine crystals have been heavily serpentinized, no resolvable chemical zoning is present within the relict olivine grains. The Mg #'s ($Mg^{2+}/(Mg^{2+} + Fe^{2+})$) for olivines vary from 0.901 to 0.915 within the suite and are homogeneous within any given sample. There is poor correlation between the Mg #'s of the olivines versus the Mg #'s of the whole rock peridotites ($r^2 = 0.47$) (Figure 4-13). It is likely, therefore, that the olivine grains record the primary chemical composition of individual rocks rather than the whole rock. Consequently, the lack of a good linear correlation suggests that serpentization and other alteration processes may have affected the composition of the whole rock.

The chemical composition has been calculated for each chromite measurement to fit the $FeCr_2O_4$ chromite model where variable amounts of Mg^{2+} substitute for Fe^{2+}, and Al^{3+} and Fe^{3+} for Cr^{3+}. The compositions of Fe^{3+} and Fe^{2+} were calculated from the total measured FeO measured according to stoichiometry specified by Droop (1987). Chromite grains have Cr #'s ($Cr^{3+}/(Cr^{3+} + Al^{3+})$) ranging from ~ 0.3 to ~ 0.6, which is consistent with Type I peridotites originating from mid-ocean ridges (Dick and Bullen, 1984). The chromite crystals exhibit no chemical zoning within individual grains

(Figure 4-14). Some grains include significant magnetite, particularly TPH069. The magnetite is found primarily as an interstitial mineral or as rims on chromite grains.

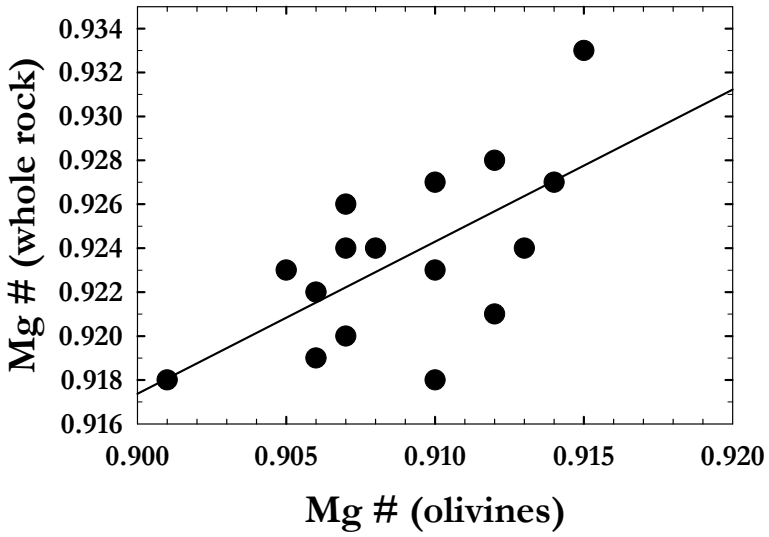

Figure 4-13. Mg # of olivine grains determined by EPMA versus Mg # of whole rock powders determined by XRF analysis.

Figure 4-14. Back-scatter electron microprobe image of a typical chromite grain found in Taitao peridotitic rocks. The bright white areas within the grain are magnetite.

Scale: _____ 500 μm

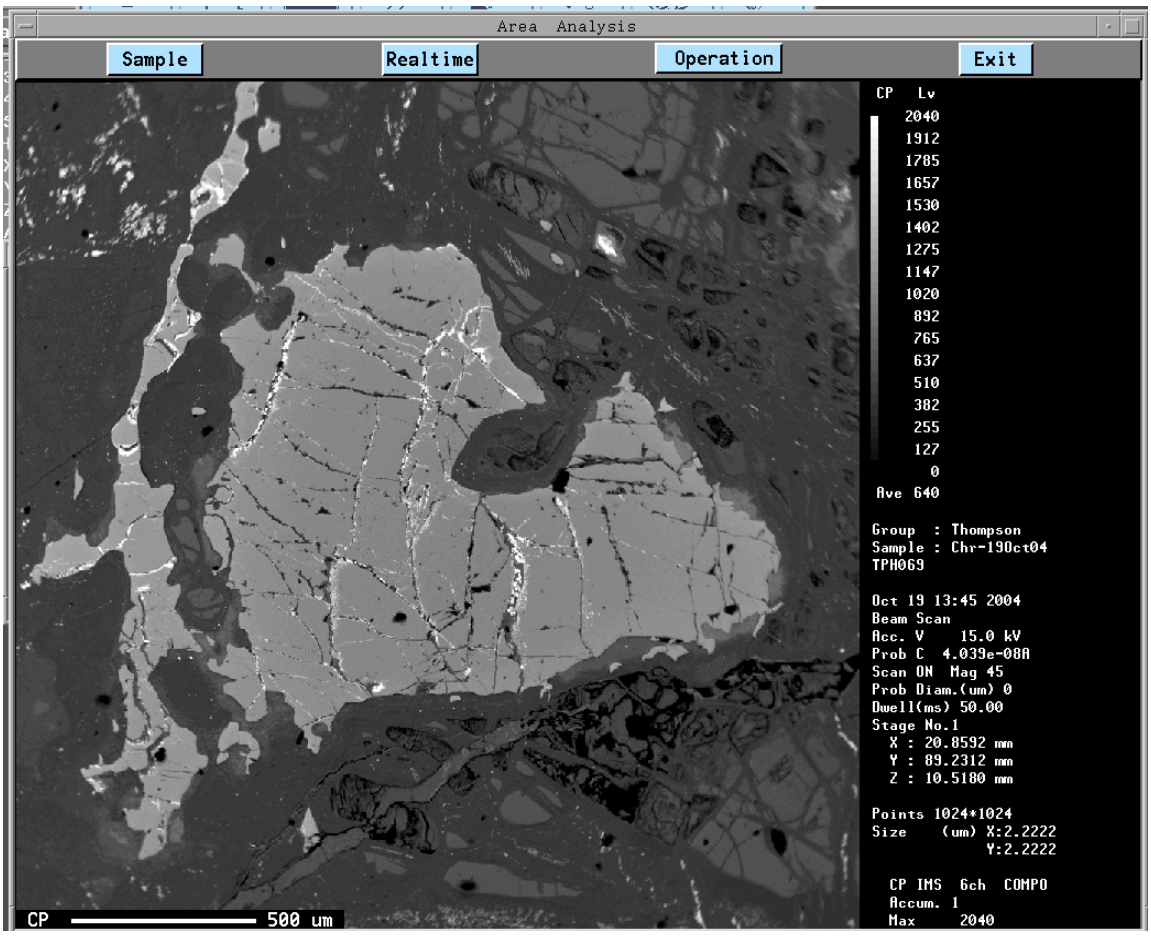

Table 4-3. Averaged microprobe data for olivines from ultramafic rocks. The reported uncertainties (2σ) refer to the standard deviations of the averaged values for each sample and are shown in parenthesis following each value. The number of spots analyzed for each sample ranges from 6 to 27, and is identified as N in the column labeled # of data points.

Sample	# of data points (N)	MgO	CoO	Al_2O_3	CaO	SiO_2	MnO	Cr_2O_3	FeO	NiO	Total	Mg #
Ultramafic Rocks:												
TPB124	**N =16**	49.27(84)	0.03(3)	0.02(4)	0.07(6)	40.90(66)	0.12(3)	0.01(4)	9.63(42)	0.37(6)	100.4	0.901
TPE068	**N = 27**	49.13(66)	0.02(3)	0.04(4)	0.21(5)	41.37(49)	0.11(4)	0.04(4)	8.72(31)	0.39(14)	100.0	0.910
TPB120	**N =18**	49.19(67)	0.03(3)	0.03(3)	0.09(4)	40.56(48)	0.12(2)	0.01(3)	9.09(29)	0.39(6)	99.5	0.906
TPE033	**N =18**	49.61(58)	0.03(3)	0.03(3)	0.10(6)	40.32(58)	0.12(3)	0.02(3)	9.03(42)	0.38(4)	99.6	0.907
TPG049	**N =9**	50.12(64)	0.03(4)	0.01(2)	0.07(3)	40.73(45)	0.07(1)	0.01(3)	8.73(25)	0.42(15)	100.2	0.912
TPH053	**N = 21**	49.85(55)	0.02(4)	0.03(9)	0.05(8)	40.63(37)	0.12(3)	0.02(5)	9.23(30)	0.40(6)	100.3	0.906
TPB116	**N = 12**	49.59(46)	0.02(2)	0.01(3)	0.07(4)	40.45(46)	0.12(2)	0.00(1)	8.79(21)	0.38(7)	99.4	0.910
TPB016	**N = 21**	49.78(73)	0.02(3)	0.02(4)	0.08(6)	40.22(70)	0.12(2)	0.01(3)	9.30(27)	0.40(6)	100.0	0.905
TPG091	**N = 10**	50.33(55)	0.03(3)	0.01(2)	0.08(7)	40.42(50)	0.08(2)	0.01(3)	9.19(23)	0.40(9)	100.6	0.908
TPB010	**N =18**	49.76(84)	0.02(4)	0.04(24)	0.10(7)	40.93(67)	0.12(3)	0.01(1)	9.11(29)	0.40(7)	100.5	0.907
TPG050	**N = 8**	48.30	0.03(4)	0.02(9)	0.05(3)	40.40(85)	0.07(2)	0.01(2)	8.60(38)	0.42(9)	99.3	0.913
dup		51.10					0.02	0.02	0.38	0.09		
TPG036	**N = 7**	50.00(49)	0.03(3)	0.02(3)	0.05(5)	41.09(29)	0.12(2)	0.01(3)	9.12(14)	0.36(7)	100.8	0.907
TPB127	**N = 14**	49.18	0.02(3)	0.01(3)	0.01(2)	41.07(78)	0.11(2)	0.01(2)	8.37(31)	0.42(12)	100.2	0.914
dup		51.22					0.02	0.02	0.31	0.12		
TPG005	**N = 6**	50.01(58)	0.04(2)	0.01(3)	0.08(3)	40.45(51)	0.08(2)	0.00(1)	8.95(21)	0.40(10)	100.0	0.910
TPE010	**N = 6**	50.08(69)	0.02(2)	0.01(3)	0.02(3)	40.61(55)	0.12(2)	0.00(1)	8.59(22)	0.43(4)	99.9	0.912
TPE024	**N = 11**	50.40(63)	0.03(3)	0.01(3)	0.07(7)	40.65(53)	0.10(3)	0.01(2)	8.34(32)	0.43(6)	100.0	0.915
Contact Rocks:												
TPH069	**N = 11**	49.39(99)	0.02(4)	0.01(3)	0.09(6)	40.31(63)	0.09(3)	0.01(4)	9.96(59)	0.38(13)	100.3	0.900
Ultramafic Dike:												
TPE027	**N = 16**	50.52(64)	0.02(2)	0.01(3)	0.06(5)	40.70(37)	0.08(3)	0.01(3)	8.36(41)	0.38(14)	100.1	0.916
Mafic Rocks:												
TPH005	**N = 15**	45.79(60)	0.04(3)	0.02(3)	0.08(10)	39.77(33)	0.20(2)	0.00(1)	13.98(35)	0.22(5)	100.1	0.854
TPE049	**N = 16**	46.62(74)	0.04(3)	0.09(36)	0.09(5)	39.85(36)	0.19(3)	0.01(2)	12.91(66)	0.22(7)	100.0	0.866

Table 4-4. Averaged chromite microprobe data. The reported uncertainties (2σ) refer to the standard deviations of the averaged values for each sample and are shown in parenthesis following the data. In those cases where the standard deviation is very large, the minimum and maximum values are listed, minimum on top and maximum below. The number of spots analyzed for each sample ranges from 7 to 36, and is identified as N in the column labeled # of data points. B.d. stands for "below detection."

Sample	# of data points (N)	MgO	CoO	Al_2O_3	MnO	SiO_2	Cr_2O_3	ZnO	NiO	FeO	TiO_2	Total	Cr #	Mg #
Ultramafic Rocks:														
TPB124	N = 9	11.42	0.08(2)	19.97	0.28(6)	0.16(1)	26.45	0.10(12)	0.13(7)	30.46	0.23(6)	97.7	0.58	0.714
		13.82		26.11			32.53			32.74				
TPE068	N = 8	11.07	0.08(2)	21.68(82)	0.17(5)	0.03(5)	43.11(51)	0.10(10)	0.13(4)	17.89	0.57(10)	98.8	0.57	0.538
		14.85								22.01				
TPB120	N = 7	18.14(47)	0.06(2)	44.99(98)	0.21(4)	b.d.	23.45(99)	0.13(12)	0.24(4)	13.11(56)	0.04(4)	100.4	0.41	0.807
TPE029	N = 10	18.30(40)	0.05(1)	46.68(85)	0.22(8)	b.d.	22.51(53)	0.12(7)	0.25(3)	12.65(66)	0.05(2)	100.8	0.39	0.855
TPE033	N = 9	12.90(97)	0.07(2)	20.90	0.39(6)	0.01(2)	42.67	0.12(7)	0.11(2)	17.51	0.30(4)	98.6	0.64	0.665
				23.34			44.75			20.29				
TPG001	N = 11	18.33(21)	0.06(2)	46.73(84)	0.24(7)	b.d.	21.93(49)	0.11(8)	0.26(2)	13.07(91)	0.05(4)	100.8	0.39	0.818
TPG049	N = 11	18.30(68)	0.06(2)	42.18	0.11(2)	0.07(17)	23.81	0.10(10)	0.24(4)	9.89	0.05(5)	101.3	0.28	0.586
				45.72			27.37			15.71				
TPB116	N = 8	18.05(27)	0.06(2)	44.49(96)	0.20(8)	b.d.	23.32	0.10(8)	0.23(3)	12.89(43)	0.07(6)	100.7	0.42	0.839
							25.80							
TPB016	N = 10	16.82(68)	0.05(3)	38.24	0.23(5)	0.04(4)	21.42	0.13(8)	0.19(4)	10.43	0.04(4)	97.2	0.46	0.807
				42.98			30.08			16.27				
TPG091	N = 14	11.71	0.07(2)	19.98	0.18(4)	0.03(3)	43.33	0.08(9)	0.10(5)	18.13	0.13(3)	99.3	0.59	0.536
		13.99		22.50			46.07			21.63				
TPG050	N = 16	18.53(45)	0.05(2)	44.27	0.09(4)	0.01(3)	22.26	0.10(7)	0.26(6)	12.03(33)	0.05(4)	100.9	0.26	0.595
				47.83			25.20							
TPG036	N = 11	18.40(69)	0.05(2)	42.03	0.23(16)	0.02(11)	20.62	0.14(8)	0.26(4)	9.76	0.04(4)	100.1	0.39	0.830
				49.25			24.04			16.24				

TPG068	N = 10	13.74(97)	0.07(2)	24.57	0.36(6)	b.d.	39.30	0.13(7)	0.12(2)	17.56	0.09(4)	99.6	0.60	0.572
				27.01			41.38			20.34				
TPB127	N = 9	16.00(53)	0.07(2)	33.85	0.29(7)	b.d.	31.40	0.14(7)	0.12(4)	13.12	0.02(3)	100.1	0.53	0.857
				37.95			35.54			15.14				
TPE024	N = 10	16.35(97)	0.07(1)	34.19	0.27(6)	0.01(3)	29.52	0.16(9)	0.17(4)	13.70	0.03(4)	99.7	0.50	0.755
				39.29			32.28			16.30				
Contact Rocks:														
TPH069	N = 36	12.94	0.07(1)	27.40	0.27(5)	0.03(3)	26.84	0.16(5)	0.19(6)	16.19	0.12(3)	98.9	0.40	0.542
		16.34		38.74			37.54			20.11				

4-4 Isotopic results

The Os concentrations for the ultramafic samples (Table 4-5) vary modestly, from 2.94 ppb to 4.82 ppb, and are, on average, slightly higher than the 3.3 ppb estimated concentration for the bulk mantle (Morgan, 1986). These concentrations are also consistent with the range observed in other mantle peridotites (e.g., Snow and Reisberg, 1995; Brandon et al., 2000; Alard et al., 2000, 2002; Harvey et al., 2006). Rhenium concentrations vary significantly, from 0.023 ppb to 0.602 ppb. Most have Re concentrations lower than the estimate for the upper mantle (0.25 ppb; Morgan, 1986). The $^{187}Re/^{188}Os$ ratios range from 0.030 to 0.765 with most less than the chondritic ratio of ~ 0.4. The $^{187}Os/^{188}Os$ ratios range considerably from 0.1168 to 0.1282. With the exception of a few samples, the ultramafic rocks have been analyzed in duplicate, one aliquot via a lower temperature digestion at 240^{o}C and one aliquot at 340^{o}C (Figure 4-15). This was done in order to assess whether the higher temperature digestion liberated more Os and Re (e.g., Reisberg and Meisel, 2002). Agreement between the $^{187}Os/^{188}Os$ ratios resulting from the two digestion temperatures is very good and generally within the measurement error of ± 0.2%. In contrast, the variation of Os concentrations in duplicates ranges from 0.5% to 69%. The heterogeneity of the Os contents probably reflects a nugget effect insofar as Os preferentially resides in refractory sulfides or other Os-bearing microinclusions (e.g., Talkington and Lippin, 1986). However, there is no evidence that the higher temperature digestion for this suite of samples preferentially liberated more Os (Figure 4-16).

Figure 4-15. Plot of $^{187}Os/^{188}Os$ ratios for whole rock peridotites digested at 240°C versus 340°C.

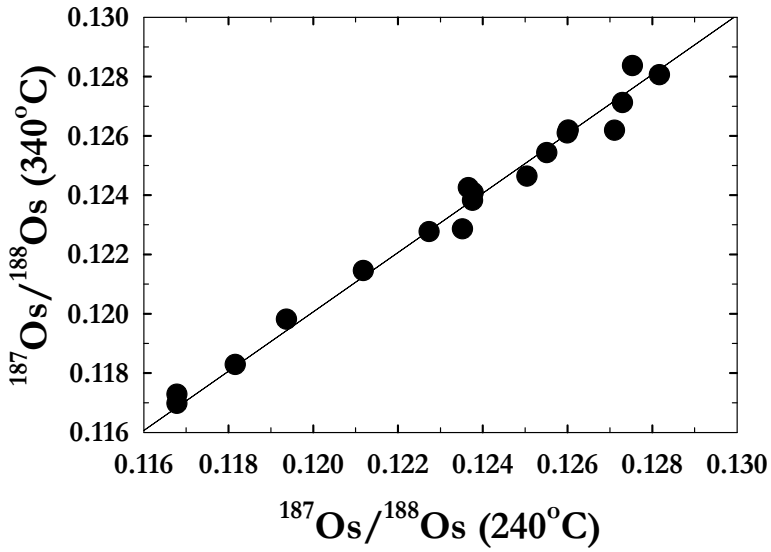

Figure 4-16. Plot of Os concentrations for whole rock peridotites digested at 240°C vs. 340°C.

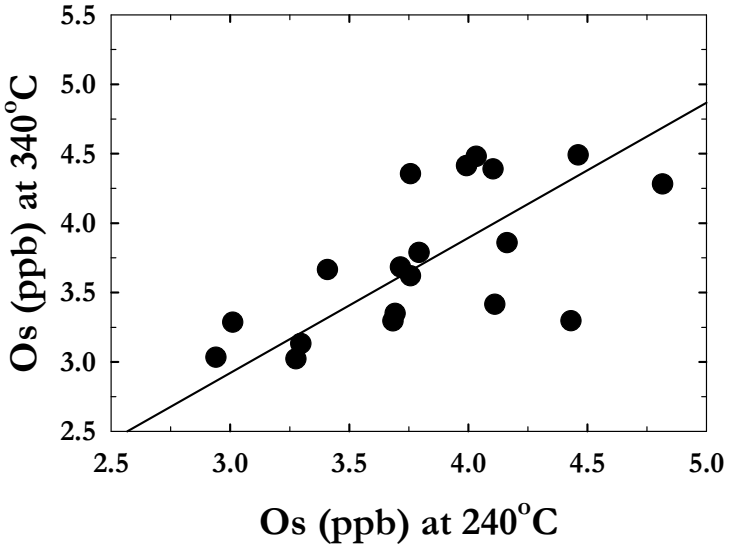

For six samples, disseminated chromite grains were separated from the whole rocks for Re-Os isotope analysis. The $^{187}Os/^{188}Os$ ratios range from 0.1199 to 0.1273. Both Os and Re concentrations vary by an order of magnitude, from 1.83 to 10.8 ppb and 0.075 to 0.745 ppb respectively. The Os isotopic compositions for chromite separates versus whole rock powders are similar. Agreement between whole rock and chromite $^{187}Os/^{188}Os$ values is 4% or better (Figure 4-17). Osmium concentrations of chromite separates are significantly higher than the whole rock powders (Table 4-5) and are consistent with earlier findings that chromites concentrate Os due to its preferential association with sulfide-bearing minerals, which may be included in chromites (Tsuru et al., 2000; Walker et al., 2002).

Samples TPG001 and TPG068 were received after previous researchers drilled them for sensitive high-mass resolution ion microprobe (SHRIMP) U-Pb dating, which evidently contaminated them with Re.

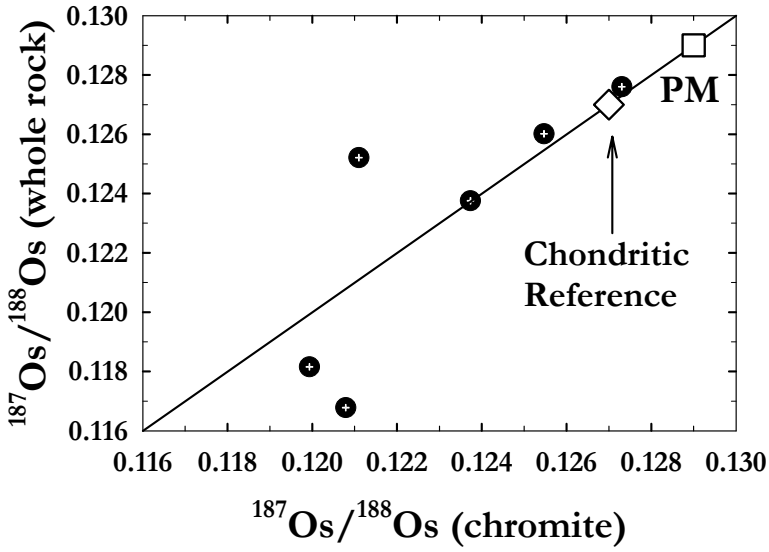

Figure 4-17. Plot of initial $^{187}Os/^{188}Os$ of chromite separates versus calculated initial $^{187}Os/^{188}Os$ of whole rock peridotitic powders.

Mafic rocks cover a much greater range in $^{187}Os/^{188}Os$ compared with the peridotitic rocks. They range from 0.1573 to highly radiogenic ratios of 0.8001. The Os concentrations range from 0.0043 ppb to 0.187 ppb. The Re concentrations of the mafic rocks vary from 0.058 ppb to 3.60 ppb.

Ten whole-rock powders, both ultramafic and mafic, were analyzed for Sm-Nd isotopic compositions, and six were analyzed for Rb-Sr (Table 4-6). These samples were chosen based on their initial Os isotopic compositions in an effort to span the range of Os isotopic compositions. With the exception of three samples, TPH053, TPG036 and TPE024 (where ε_{Nd} = -24.3, < -5.4, and –3.7, respectively), ε_{Nd} values of the ultramafic samples are consistent with the range for the modern day upper mantle (e.g., ε_{Nd} = +8 to +10; DePaolo and Wasserburg, 1976). Concentrations of Sm and Nd in the ultramafic rocks are low and range from less than 0.0053 ppm to 0.1958 ppm for Sm and from

0.0025 ppm to 0.5804 ppm for Nd. These results are typical of peridotites in which no interaction with incompatible-rich melts or crustal components have occurred, insofar as Sm and Nd are incompatible elements. The $^{147}Sm/^{144}Nd$ ratios of the peridotitic samples range from 0.1700 to 0.4331. In contrast, Sm and Nd concentrations are high in the mafic rocks, ranging from 0.653 ppm to 6.33 ppm for Sm and 1.425 ppm to 14.8 ppm for Nd. The $^{87}Sr/^{86}Sr$ range from 0.703179 to 0.707948, and overlap with the range identified by Guivel et al. (1999) for N-MORB- and calc-alkaline-like magmas from the Taitao ophiolite ($^{87}Sr/^{86}Sr$ = 0.702650 to 0.704394).

Whole rock $\delta^{18}O$ values range from 2.47‰ to 5.03‰ for peridotitic whole rock powders (Table 4-5). The $\delta^{18}O$ values for olivine grains from eight ultramafic rocks vary much less, from 5.02 ± 0.50 ‰ to 5.83 ± 0.58 ‰. On average, these values are more consistent with the widely-accepted estimated $\delta^{18}O$ of the mantle ($\delta^{18}O_{mantle}$ = 5.2 ± 0.1 ‰; Mattey et al., 1994).

Table 4-5. Re-Os concentration and Os isotopic data for ultramafic and mafic whole rock powders. The uncertainties reported express two standard deviations of the mean ($2\sigma_{mean}$) of the mass spectrometry data sets and are shown in parentheses following each value. In those cases where the standard deviation is very large or includes a decimal point, the minimum and maximum values are listed, minimum on top and maximum below. The uncertainty for γ_{Os} is listed in a column next to the column for the calculated value.

Sample	Re	Os	$^{187}Re/^{188}Os$	$^{187}Os/^{188}Os$	γ_{Os}	T_{RD} (Ga)	Olivine $\delta^{18}O$	$\delta^{18}O$ (W.R.)	Mg# (W.R.)	Olivine Mg #
Ultramafic Samples										
TPB124	**0.323(3)**	**4.104(3)**	**0.379(4)**	**0.12602(9)**	**-0.71(1)**	**0.15**	5.15(2)	4.60(32)	0.906	0.901(4)
	0.314(3)	4.390(2)	0.345(3)	0.12606(6)	-0.71(1)	0.14				
TPB124-chr	0.608(6)	13.53(2)	0.216(2)	0.12547(16)	-1.15(1)	0.23				
TPE068	**0.207(2)**	**4.431(6)**	**0.225(2)**	**0.12409(16)**	**-2.24(2)**	**0.43**	5.70(2)	3.58(1)	0.906	0.910(3)
TPB120	**0.298(3)**	**4.163(5)**	**0.345(3)**	**0.12760(14)**	**0.53(1)**	**-0.09**		4.05(5)	0.909	0.906(2)
	0.297(3)	3.859(2)	0.371(4)	0.12747(5)	0.40(0)	-0.07				
TPB120-chr	0.723(7)	9.185(32)	0.379(4)	0.12731(45)	0.31(0)	-0.05				
TPE029	**0.206(2)**	**3.409(8)**	**0.291(3)**	**0.12521(28)**	**-1.36(1)**	**0.27**		3.47(1)	0.908	No olivines
	0.246(2)	3.666(2)	0.324(3)	0.12473(8)	-1.75(2)	0.93				
TPE029-chr	0.671(7)	10.81(26)	0.299(3)	0.12072(29)	-4.89(5)	0.34				
TPE033	**0.121(2)**	**3.993(5)**	**0.146(1)**	**0.12376(16)**	**-2.51(3)**	**0.48**	5.24(2)	3.43(2)	0.909	0.907(4)
	0.127(2)	4.414(8)	0.138(1)	0.12382(21)	-2.47(2)	0.47				
TPE033-chr	0.373(4)	5.767(11)	0.311(3)	0.12374(23)	-2.51(3)	0.48				
TPG001	**n.d.***	**3.715(6)**	**n.d.***	**0.12585(19)**	**-0.88(1)**	**0.17**		3.57(1)	0.909	No olivines
TPG049	**0.142(1)**	**4.816(4)**	**0.142(1)**	**0.12378(11)**	**-2.51(3)**	**0.48**	5.56(2)	4.40(1)	0.912	0.912(3)
	0.162(2)	4.282(5)	0.182(2)	0.12414(13)	-2.22(2)	0.43				
TPH053	**0.371(4)**	**2.629(3)**	**0.681(7)**	**0.12728(14)**	**0.31(0)**	**-0.04**		4.27(1)	0.911	0.906(3)
	0.353(4)	3.415(12)	0.499(5)	0.12712(44)	0.13(0)	-0.02				
TPB116	**0.211(2)**	**3.693(3)**	**0.275(3)**	**0.12274(9)**	**-3.30(3)**	**0.63**		4.60(0)	0.911	0.910(2)
	0.167(2)	3.350(3)	0.241(2)	0.12280(10)	-3.25(3)	0.62				
TPE005	**0.070(1)**	**4.111(2)**	**0.082(1)**	**0.11816(6)**	**-6.93(7)**	**1.3**		2.47(0)	0.912	No olivines

	0.133(1)	4.492(3)	0.142(1)	0.11834(9)	-6.78(7)	1.3				
TPE005-chr	0.434(4)	9.900(18)	0.211(2)	0.11994(21)	-5.51(6)	1.0				
TPB016	**0.602(6)**	**3.793(2)**	**0.765(8)**	**0.12753(8)**	**0.51(1)**	**-0.08**	5.83(2)	5.03(1)	0.912	0.905(3)
	0.358(4)	3.788(13)	0.456(5)	0.12837(44)	1.11(1)	-0.20				
TPG091	**0.223(2)**	**3.297(0)**	**0.325(3)**	**0.12599(1)**	**-0.76(1)**	**0.15**	5.02(2)	3.72(1)	0.914	0.908(2)
	0.194(2)	3.132(10)	0.298(3)	0.12610(42)	-0.68(1)	0.13				
TPB010	**0.242(2)**	**3.757(1)**	**0.311(3)**	**0.12817(4)**	**0.98(1)**	**-0.17**		4.67(2)	0.914	0.907(2)
	0.272(3)	3.620(3)	0.362(4)	0.12813(9)	0.95(1)	-0.17				
TPG050	**0.171(2)**	**3.276(1)**	**0.251(3)**	**0.12366(4)**	**-2.60(3)**	**0.50**		4.28(2)	0.916	0.913(3)
	0.138(1)	3.023(5)	0.220(2)	0.12406(19)	-2.29(2)	0.44				
TPG036	**0.175(2)**	**3.011(3)**	**0.281(3)**	**0.12551(11)**	**-1.12(1)**	**0.22**		4.41(1)	0.915	0.907(1)
	0.211(2)	3.287(2)	0.309(3)	0.12550(9)	-1.12(1)	0.22				
TPG068	**n.d.***	**3.959(6)**	**n.d.***	**0.12717(19)**	**0.16(0)**	**-0.03**		4.24(1)	0.916	n.d.
TPB127	**0.023(1)**	**3.684(6)**	**0.030(0)**	**0.11938(18)**	**-5.976)**	**1.1**	5.33(2)	3.88(2)	0.916	0.914(3)
	0.023(1)	3.295(19)	0.034(0)	0.11982(71)	-5.62(6)	1.1				
TPG005	**0.115(1)**	**2.940(2)**	**0.189(2)**	**0.12504(10)**	**-1.51(2)**	**0.29**		3.43(0)	0.916	0.910(2)
	0.140(1)	3.033(9)	0.222(2)	0.12464(35)	-1.83(2)	0.35				
TPE010	**0.124(1)**	**4.462(6)**	**0.134(1)**	**0.12118(18)**	**-4.54(5)**	**0.86**		4.63(1)	0.918	0.912(3)
	0.121(1)	4.355(32)	0.134(1)	0.12146(90)	-4.33(4)	0.82				
TPE024	**0.287(3)**	**4.033(1)**	**0.342(3)**	**0.11678(4)**	**-7.99(8)**	**1.5**	5.26(2)	5.03(1)	0.924	0.915(3)
	1.06(1)	4.481(2)	1.14(1)	0.11703(6)	-7.73(8)	1.5				
	0.428(4)	5.031(17)	0.410(4)	0.11717(40)	-7.71(8)	1.5				
TPE024-chr	0.308(3)	3.837(9)	0.387(4)	0.12083(27)	-4.80(5)	0.92				
Contact rocks:										
TPH069	**1.13(1)**	**2.800(4)**	**1.94(2)**	**0.12711(19)**	**0.12(0)**	**-0.02**		4.06(1)	0.905	0.900(5)
	0.343(3)	4.303(5)	0.383(4)	0.12604(14)	-0.72(1)	0.14				
TPE004	**0.042(2)**	**6.486(6)**	**0.031(0)**	**0.12114(12)**	**-4.58(5)**	**0.87**		2.18	0.912	n.d.
TPH065	**0.309(3)**	**3.898(6)**	**0.381(4)**	**0.12352(18)**	**-2.71(3)**	**0.52**		3.52(1)	0.879	n.d.
	0.248(2)	4.944(3)	0.241(2)	0.12274(7)	-3.32(3)	0.63				
Ultramafic Dike:										
TPE027	**0.023(1)**	**0.094(0)**	**1.21(1)**	**0.22542(105)**	**78(1)**	**-17**		4.88	0.926	0.916(4)
Mafic Rocks:										
TPB042	**0.058(1)**	**0.005(0)**	**61.6(6)**	**0.79214(489)**	**529(5)**	**-111**		5.84	0.350	

TPB040	**0.124(43)**	**0.014(0)**	**41.6(4)**	**0.17158(77)**	**38(0)**	**-7.1**		2.83	0.581	
TPB039	**2.025(1)**	**0.011(0)**	**924(9)**	**0.55798(1)**	**412(4)**			2.67	0.679	
TPB046	**0.063(20)**	**0.004(0)**	**73.5(7)**	**0.43902(215)**	**252(3)**	**-90**		5.27	0.681	
TPE017	**0.649(1)**	**0.009(0)**	**372(4)**	**0.22277(279)**	**105(1)**	**-16**		5.51	0.684	
TPB023	**0.105(6)**	**0.009(0)**	**57.8(6)**	**0.23797(106)**	**92(1)**	**-19**		2.51	0.742	
TPH063	**0.101(1)**	**0.012(0)**	**41.1(4)**	**0.21768(128)**	**75(1)**	**-15**		3.65(1)	0.824	
TPE063	**0.184(1)**	**0.053(0)**	**16.8(2)**	**0.15814(117)**	**26(0)**	**-4.8**		5.80	0.834	
TPH005	**1.06(2)**	**0.038(0)**	**135(2)**	**0.15266(47)**	**31(0)**	**-4.0**		5.53	0.860	0.854(4)
TPE049	**3.60(1)**	**0.187(0)**	**93.0(9)**	**0.15570(14)**	**30(0)**	**-4.4**		6.09	0.869	0.866(7)

Results for samples digested at 240°C are in bold. Chromite separates are identified by the suffix –chr. N.d. stands for "not determined." The asterisk (*) following Re concentration data and $^{187}Re/^{188}Os$ ratios indicates that the sample was contaminated by a metal blade when drilled for SHRIMP U-Pb dating. γ_{Os} = % difference between Os isotopic composition of sample at time T (6 Ma) and reference chondrite value at that same time. T_{RD} = time of Re depletion. W.R. represents "whole rock."

Table 4-6. Sm-Nd and Rb-Sr isotopic results. All concentrations are in ppm.

Sample	Sm	Nd	$^{143}Nd/^{144}Nd$	$^{147}Sm/^{144}Nd$	ε_{Nd}	Rb	Sr	$^{87}Sr/^{86}Sr$	$^{87}Rb/^{86}Sr$
Ultramafic Rocks:									
TPE033	0.0268	0.0578	0.513113	0.2802	9.2	0.0793	0.545	0.7032	37.79
TPH053	0.0068	0.0095	0.5114	0.4331	-24.3	n.d.	n.d.	n.d.	n.d.
TPE005	0.0473	0.1501	0.513111	0.1907	9.2	0.053	1.03	0.7079	94.48
TPB010	0.1958	0.5804	0.513161	0.204	10.2	0.217	0.5041	0.7042	49.70
TPG036	<0.0053	0.0025	0.5124	<1.2813	<-5.4	n.d.	n.d.	n.d.	n.d.
TPB127	0.0219	0.0745	0.51309	0.1773	8.9	n.d.	n.d.	n.d.	n.d.
TPE024	0.0128	0.0454	0.512446	0.170	-3.7	0.0388	0.617	0.7053	62.66
Mafic Rocks:									
TPB040	6.331	14.81	0.51328	0.2601	12.5	1.688	94.31	0.7047	55.70
TPE017	2.788	8.149	0.513168	0.2087	10.3	4.392	n.d.	n.d.	n.d.
TPE049	0.6528	1.4255	0.51316	0.2767	10.2	n.d.	n.d.	n.d.	n.d.

CHAPTER 5: DISCUSSION

5-1 Evidence for variable extents of partial melting

Major and trace element characteristics of the ultramafic rocks of the Taitao ophiolite are mostly consistent with their being residues of variable extents of partial melting of the upper mantle. In particular, incompatible elements, such as vanadium, show clear positive correlations with Al_2O_3 (Figure 4-10), consistent with trends observed in mid-Atlantic ridge abyssal peridotites examined by Harvey et al. (2006) as well as peridotitic samples from the Troodos ophiolite (Büchl et al., 2004). A positive correlation between MgO versus Al_2O_3 also provides evidence for the variable loss of a melt component (Figure 4-3), and is comparable to the depletion trends recorded in other suites of mantle rocks (e.g., Southwestern Indian and American-Antarctic Ridge abyssal peridotites, Snow and Dick, 1995; Internal Ligurides, Rampone et al., 1996; and Oman ophiolite, Godard et al., 2000). Other melt depletion trends, like MgO versus CaO are only broadly consistent with variable extents of melt depletion (Figure 4-5).

Chromite grains have Cr #'s ($Cr^{3+}/(Cr^{3+} + Al^{3+})$) ranging from ~ 0.3 to ~ 0.6, which is consistent with Type I peridotites generated at mid-ocean ridges (Dick and Bullen, 1984). The Cr #'s generally increase from lherzolites to harzburgites, and this trend can be explained by partial melting (Dick and Bullen, 1984) or melt percolation processes in which lherzolites become harzburgites by clinopyroxene dissolution or incongruent melting of orthopyroxene (Büchl et al. 2004; Kelemen et al., 1997).

While some of the chromites contain high concentrations of iron (ferritochromite), suggesting some recrystallization (Walker et al., 2002), a plot of Cr # vs. Mg # places the analyzed chromites within the context of primary ophiolite chromites

analyzed in previous studies (Figure 5-1). Many of the chromites from Taitao lie close to or within the 50% and 90% fields proposed by Barnes and Roeder (1991). Exceptions include some chromites from TPG050 and TPG049, which plot with low Cr #'s (Figure 5-1). These may be the result of lesser degrees of partial melting (suggested by higher Mg #), multiple episodes of metamorphism, differences in the magma source, or that the ophiolite chromite data compiled by Barnes and Roeder are not representative of ophiolite chromites worldwide.

Figure 5-1. Plot of Cr # vs. Mg # for chromite grains in peridotitic samples. The fields represent 90% and 50% of ophiolite chromites from Barnes and Roeder (1991).

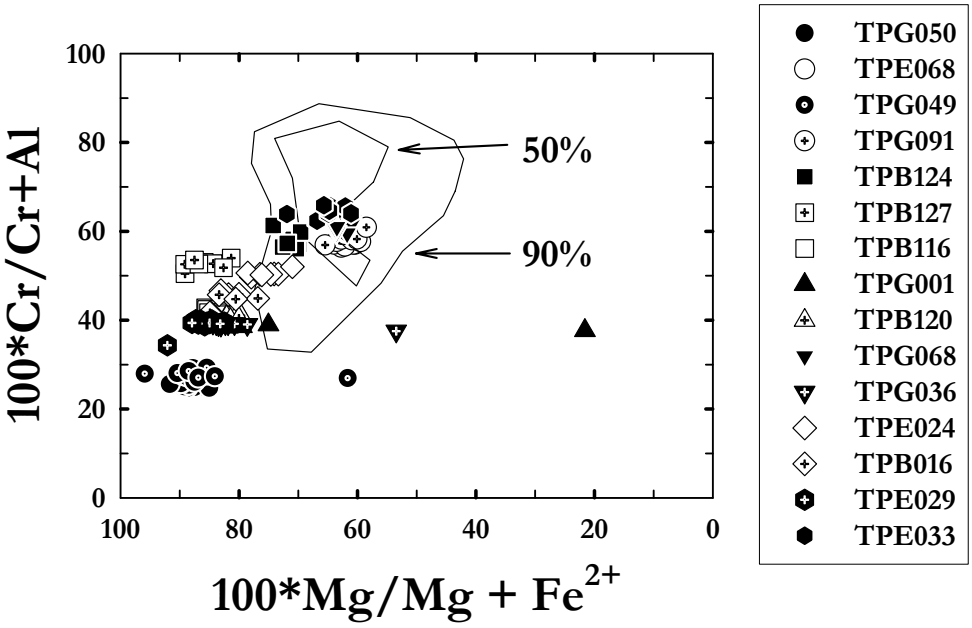

5-2 Alteration History

Variations of oxygen isotope ratios in mantle rocks can be used to constrain the contribution of subducted crustal igneous rocks, sediments, and fluid interactions to the relevant mantle region. Given that the Taitao peridotites have undergone significant serpentinization, oxygen isotope data were obtained for both whole rock powders and olivine separates to assess whether there is evidence of a subducted crustal or non-mantle component in the rocks. These results may also provide insight into the variations recorded in the Os isotopic data.

The $\delta^{18}O$ values for olivine grains range from +5.02‰ to +5.83‰, which largely agrees with the estimated $\delta^{18}O$ mantle value ($\delta^{18}O = 5.2 \pm 0.1$ ‰; Mattey et al., 1994). Any significant interaction with meteoric water, seawater or hydrous fluid at both high (750^{o}C) and low (300^{o}C) temperatures would likely drive the $\delta^{18}O$ value of the olivine grains lower given that little fractionation between olivine and water occurs at both high and low temperatures ($\alpha_{olivine\text{-}water}$ = 0.997 at 750^{o}C and 0.996 at 300^{o}C when $\alpha_{forsterite\text{-}calcite}$ is divided by $\alpha_{calcite\text{-}water}$; Clayton and Keiffer, 1991; Hu and Clayton, 2003). The concept of equilibrium is based on the thermodynamic assumption that energy is constant and equals RTlogK (where R is the gas constant, T is temperature and K is the partition coefficient), such that equilibrium fractionation is large at low temperatures but approaches zero at infinitely high temperatures. Because seawater has a $\delta^{18}O$ value of 0 ‰, olivine grains that are in equilibrium with seawater at 300^{o}C will possess $\delta^{18}O$ values of –3 ‰, and –4 ‰ at 750^{o}C (based on their respective $\alpha_{olivine\text{-}water}$ values). The mantle-like $\delta^{18}O$ values of olivine, therefore, suggest that the grains record the oxygen isotopic compositions of the mantle at the time of formation (Figure 5-2). Three olivine samples

(TPE068, TPB016 and TPG049) plot above the uncertainty associated with the $\delta^{18}O$ mantle estimate, although they are still within the range generally accepted as typical of mantle values (up to 5.7 ± 0.5 ‰; Eiler et al., 1998). In situ analyses of olivine grains with a UV laser using BrF_5 (which was the analytical technique used in this study) have been shown to result in erroneously low values, with $\delta^{18}O$ values decreasing 1 ‰ for every increase in pressure of 10 torr (Rumble et al., 1997). For this reason, it is unlikely that analytical error is the cause of the higher-than-mantle $\delta^{18}O$ values. On the other hand, if the $\delta^{18}O$-enriched olivine grains are not representative of the mantle, their compositions may be due to assimilation of an ^{18}O-enriched material.

For whole rock powders, the $\delta^{18}O$ values range from 2.47‰ to 5.03‰. Most of these values extend below the $\delta^{18}O$ estimate for the mantle. Exchange of O between rocks and fluids at low temperatures is unlikely due to the decrease in $\delta^{18}O$ values from olivine to the whole rock. Otherwise, the $\delta^{18}O$ values would be higher than the mantle estimate. Instead, it is likely that the fractionation occurred at high temperatures.

The lack of correlation in the initial $^{187}Os/^{188}Os$ composition versus $\delta^{18}O$ in both the whole rock and olivine phenocrysts suggests that hydrothermal interaction with seawater or other hydrous fluids has not affected the Os isotopic compositions of the peridotites (Figures 5-3 & 5-4). Similarly, there is no correlation between $\delta^{18}O$ and $^{187}Os/^{188}Os$ of mafic rocks (Figure 5-5).

While variations in oxygen and Os isotopic compositions need not be linked, correlations, if present, might suggest that the Os isotopic data was somehow associated with the oxygen isotope data and any fluid-derived alteration recorded by the oxygen isotopes might have also then affected the Os isotopic compositions. In addition, the

$^{187}Os/^{188}Os$ of seawater is highly radiogenic at ~ 1.06 (Levasseur et al., 1998) so that high $^{187}Os/^{188}Os$ values might be expected to correspond with O variations had interaction with seawater occurred. Such radiogenic Os isotopic signatures are not observed in the Taitao peridotites. Furthermore, the oxygen isotopic data of the olivines appear to reflect the accepted mantle $\delta^{18}O$ value. Also, the Os isotopic compositions of the peridotitic rocks seem to retain their initial mantle signatures based on the agreement between the Os isotopic compositions of the whole rock with the chromite separates. It must follow, therefore, that any interaction with seawater or hydrous fluid did not significantly affect the Os isotopic compositions of the whole rock.

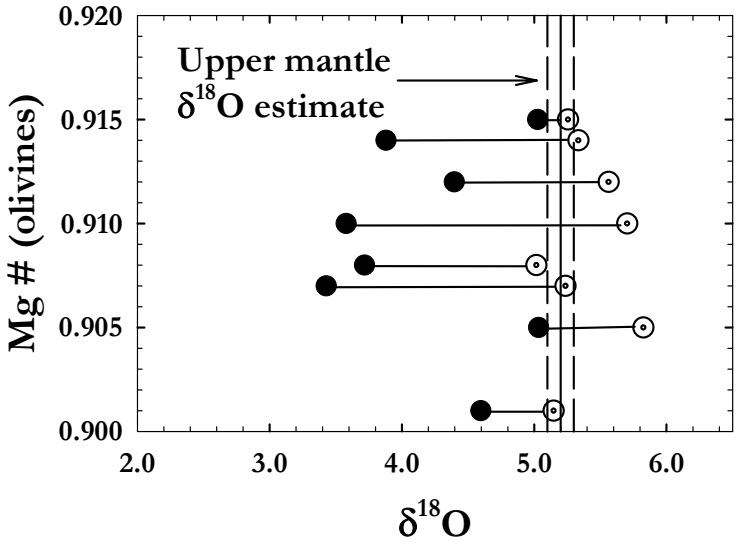

Figure 5-2. Whole rock (filled circles) and olivine (open circles) $\delta^{18}O$ versus Mg # of olivine. The dashed vertical lines represent the uncertainty associated with the upper mantle $\delta^{18}O$ estimate (Mattey et al., 1994).

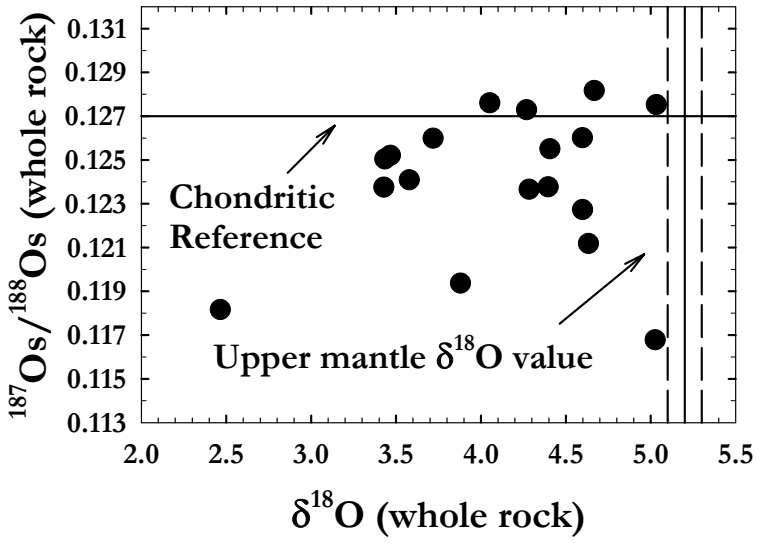

Figure 5-3. Plot of $\delta^{18}O$ versus $^{187}Os/^{188}Os$ for whole rock peridotites. The dashed vertical lines represent the uncertainty associated with the upper mantle $\delta^{18}O$ estimate of Mattey et al., 1994.

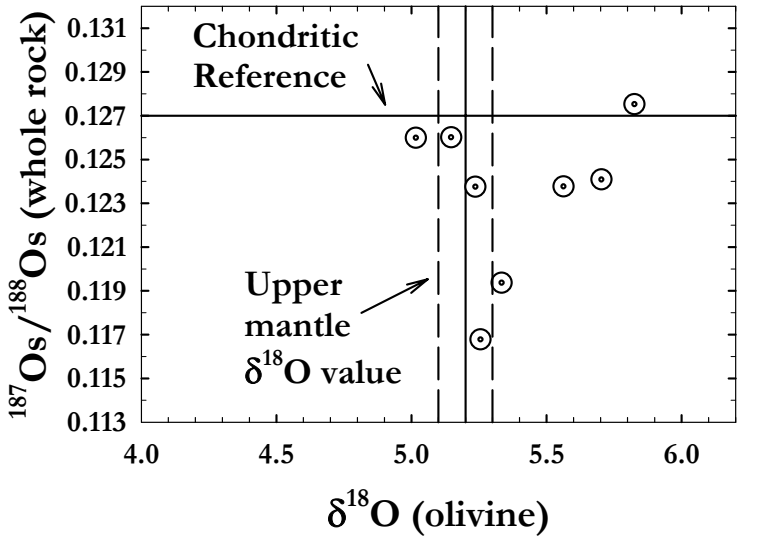

Figure 5-4. Plot of $\delta^{18}O$ of olivine grains versus $^{187}Os/^{188}Os$ for whole rock peridotites. The dashed vertical lines represent the error associated with the upper mantle $\delta^{18}O$ estimate (Mattey et al., 1994).

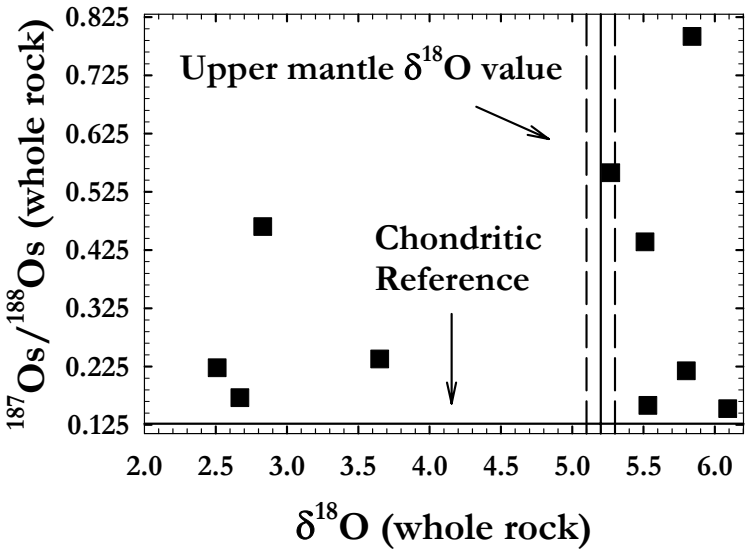

Figure 5-5. Plot of $\delta^{18}O$ versus $^{187}Os/^{188}Os$ for mafic whole rocks. The dashed vertical lines represent the error associated with the upper mantle $\delta^{18}O$ estimate (Mattey et al., 1994).

5-3 Re-Os isotope systematics

Significant Os isotopic heterogeneity is present in the peridotitic whole rocks, with a range of ~ 9% ($^{187}Os/^{188}Os$ = 0.1168 to 0.1282). The isotopic heterogeneity is generally consistent with earlier studies of abyssal peridotites and individual ophiolites (0.117-0.158; Snow and Reisberg, 1995; Brandon et al., 2000; Standish et al., 2001; Walker et al., 2004; Harvey et al., 2006). Specifically, abyssal peridotites from the SW Indian and American-Antarctic Ridges examined by Snow and Reisberg (1995) have $^{187}Os/^{188}Os$ ratios that range from 0.1221 to 0.1270, with a mean of 0.1246 ± 0.0014. The ten abyssal peridotites chosen for analysis were samples that underwent minimal alteration, based on Sr and Nd criteria, as well as major element compositional changes. A similar range in $^{187}Os/^{188}Os$ was observed in abyssal peridotites from the Kane Transform area in the Atlantic Ocean ($^{187}Os/^{188}Os$ = 0.1227 to 0.1276) (Brandon et al.,

2000). Standish et al. (2002), on the other hand, reported a much larger Os isotopic range for abyssal peridotites from the SW Indian and mid-Atlantic Ridges. They found whole rock abyssal peridotites with $^{187}Os/^{188}Os$ values as depleted as 0.1183 and as radiogenic as 0.1582. Similarly, Harvey et al. (2006) reported an $^{187}Os/^{188}Os$ range of 0.1169 to 0.1267 for heavily serpentinized abyssal peridotites from a single core in the mid-Atlantic Ridge. Two sulphide grains from this section had extremely unradiogenic Os isotopic compositions ($^{187}Os/^{188}Os = 0.114$). The $^{187}Os/^{188}Os$ values for over 100 Os-Ir-Ru alloy grains from southwestern Oregon, thought to be from the Mesozoic Josephine ophiolite, range from 0.1173 to 0.1468 (Walker et al., 2005). Meibom et al. (2002, 2004) measured Os-rich platinum group element (PGE) alloys from placer deposits in the Klamath and Siskiyou Mountains of northern California and southwestern Oregon that range from 0.1095 to 0.1870, with the majority of the analyses falling within a Gaussian distribution from about 0.1200 to 0.1300.

Osmium isotopic composition heterogeneity has also been noted for individual ophiolites (Walker et al., 2002). Harzburgites from the Troodos Ophiolite Complex on Cyprus record slightly suprachondritic Os isotopic compositions, with $^{187}Os/^{188}Os$ ranging from 0.1288 to 0.1311 (Büchl et al., 2002). Dunites from the same melt channel, however, are significantly enriched ($^{187}Os/^{188}Os = 0.1335$ to 0.1374) in relation to the carbonaceous chondrite reference ($^{187}Os/^{188}Os$ at 90 Ma = 0.1264), and were interpreted as resulting from melt infiltration. The $^{187}Os/^{188}Os$ of peridotites from the Internal and External Ligurian Ophiolite in northern Italy range from 0.1219 to 0.1223, and 0.1233 to 0.1283, respectively (Snow et al., 2000). Despite the abundance of previous ophiolite studies involving Re-Os analyses, the causes of Os heterogeneity are still not well

constrained. Osmium isotopic heterogeneities in materials presumed to be representative of the DMM could reflect long-term, variable melt depletion or fluid transport of radiogenic or depleted Os into the rocks. In the case of the Taitao peridotites, an isochron is generated by the linear correlation between $^{187}Re/^{188}Os$ versus $^{187}Os/^{188}Os$ (Figure 5-6). The slope of this line suggests that variable extents of partial melting occurred at ~ 1.5 Ga. As a result, this event may be the cause of the observed Os isotopic heterogeneity.

For samples of subcontinental lithospheric mantle (SCLM), correlations between Os isotopic composition and Al_2O_3 or Mg # have been shown to record ancient melt depletion effects (e.g., Walker et al., 1989; Reisberg and Lorand, 1995; Meisel et al., 1996; Gao et al., 2002). Similar to the relationship (or isochron) created by $^{187}Os/^{188}Os$ and $^{187}Re/^{188}Os$, Al_2O_3 should correlate with $^{187}Os/^{188}Os$ in residues because, like Re, it is moderately incompatible. The $^{187}Os/^{188}Os$ of the intercept, or the $^{187}Os/^{188}Os$ present at the lowest Al_2O_3 composition, can then be used as the initial ratio, which, when compared to a model mantle evolution trend, provides a model age (Reisberg and Lorand, 1995; Walker et al., 1989). Comparison of $^{187}Os/^{188}Os$ with Mg #, which is a marker of fertility, has also been found to produce a linear relationship if the peridotites have undergone a melt depletion event, but the trend is in the opposite direction.

The time of melt depletion can be established for individual peridotites using the measured Re/Os ratio to extrapolate back in time to when the $^{187}Os/^{188}Os$ of the sample matched that of the primitive upper mantle (T_{MA} ages). Model ages obtained via this method are analogous to those determined by Sm-Nd systematics. Another method (T_{RD}), which provides a minimum estimate of the timing of melt depletion and is more useful in systems where late-stage Re addition is likely, is similar to the T_{MA} model age

but assumes the initial Re/Os of the sample is zero. At high levels of partial melting the Re/Os of the residue should actually approach zero such that the T_{MA} and T_{RD} ages for uncontaminated samples will converge.

Massif peridotites from the eastern Pyrenees as well as the Ronda Ultramafic Complex record correlations in $^{187}Os/^{188}Os$ versus Al_2O_3, which were used to constrain the initial Os isotopic ratios of the bodies (Reisberg and Lorand, 1995). The time of lithospheric incorporation was determined by comparison with a mantle evolution curve due to the lack of a good correlation between $^{187}Os/^{188}Os$ and $^{187}Re/^{188}Os$. For Ronda, the age of the initial melt depletion event was estimated to be ~ 1.3 Ga, and for the Pyrenean peridotites ~2.3 Ga.

In the case of the Taitao peridotites, the positive correlations between $^{187}Os/^{188}Os$ and Mg # of whole rock and olivine as well as Al_2O_3 are similar to what is observed for SCLM, and are thus consistent with a melting event at ~ 1.5 Ga (Figures 5-7 & 5-8). The T_{RD} of most of the samples are also generally consistent with this age. This suggests that this block of mantle has remained isolated within the convecting mantle since the time of initial melt depletion. Unlike SCLM, however, the Taitao ophiolite is likely from the DMM, and is well mapped with known tectonic associations. Furthermore, petrologic data of peridotite xenoliths from SCLM as well as abyssal peridotites cannot be tied to their initial distribution within the mantle, which creates problems when attempting to constrain Os isotopic variability in the upper mantle. As a result, the Taitao ophiolite is the first example of a well mapped, ancient melt depletion event in the DMM that has been retained in the rock record.

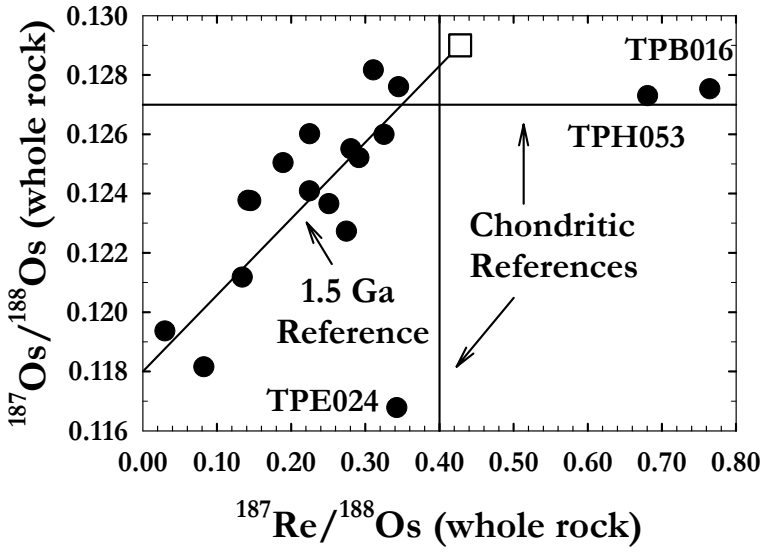

Figure 5-6. Plot of $^{187}Re/^{188}Os$ versus calculated initial $^{187}Os/^{188}Os$ of peridotitic whole rocks. The open box represents the composition of the PM (Meisel et al., 1996).

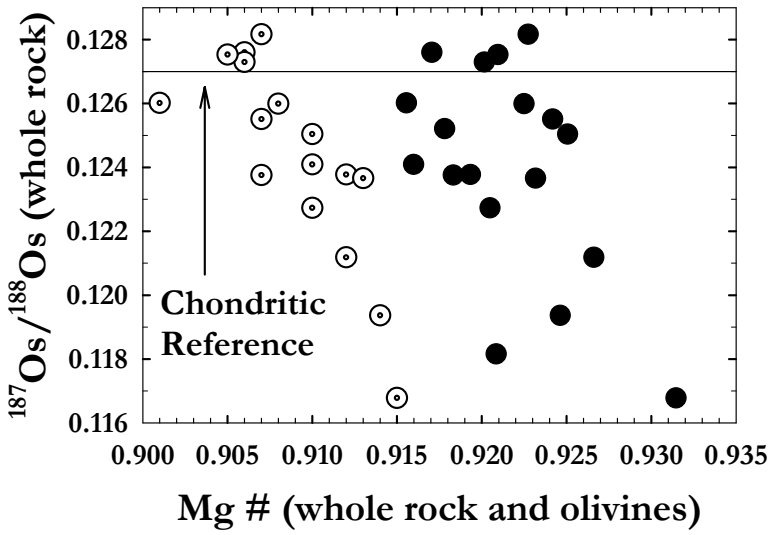

Figure 5-7. Plot of Mg # in olivines (open circles with dots) and whole rock (filled circles) vs. bulk $^{187}Os/^{188}Os$. The PM estimate for whole rock Mg # is 0.88 (McDonough and Sun, 1995).

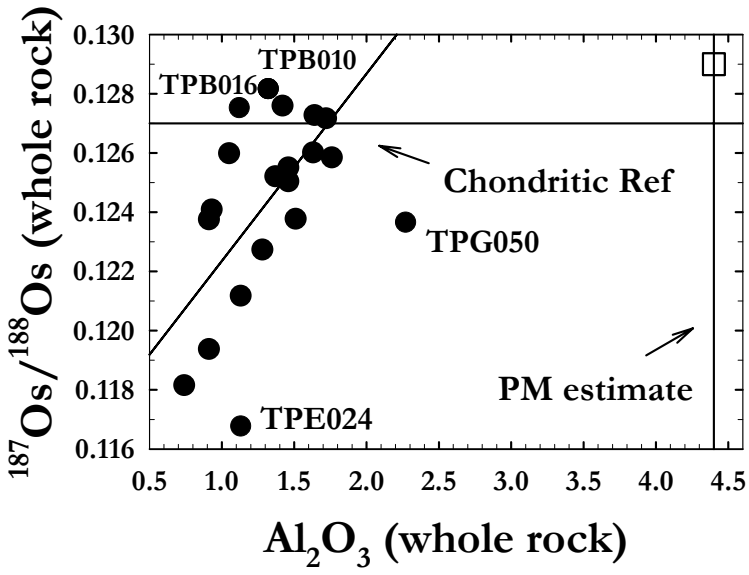

Figure 5-8. Whole rock Al_2O_3 determined by XRF analysis and recalculated to anhydrous versus bulk $^{187}Os/^{188}Os$ where the PM estimate for $^{187}Os/^{188}Os$ is 0.1296 ± 0.0008 (Meisel et al., 1996) and 4.4 wt % for Al_2O_3 (McDonough and Sun, 1995). The r^2 = 0.55 for all whole rock peridotites except for samples TPE024 and TPB016, which most likely experienced secondary Re addition, TPG050, which had significantly more Al_2O_3 than any other sample, and TPB010, which was suprachondritic with respect to the $^{187}Os/^{188}Os$ chondritic reference.

5-4 Chromite Separates

As noted above, bulk peridotite samples are subject to modification by recent processes. Chromites are, therefore, of particular interest in Re-Os studies because they are highly resistant to alteration. Additionally, they concentrate Os and exclude Re such that they may record the initial $^{187}Os/^{188}Os$ of ancient rocks. In the case of the Taitao peridotites, the $^{187}Os/^{188}Os$ ratios of chromite separates range from 0.1199 to 0.1273 and are similar to the Os isotopic compositions of the corresponding whole rock powders, with agreement greater than analytical uncertainty at 4% or better (Figure 4-17). The general agreement between the whole rock $^{187}Os/^{188}Os$ and chromite separates thus

partially confirms that serpentinization has not significantly affected or altered the Os isotopic compositions.

5-5 Mafic Rocks

The calculated initial $^{187}Os/^{188}Os$ ratios of nearly all of the mafic rocks are substantially enriched relative to chondritic and the peridotites, suggesting a transfer of radiogenic Os to the rocks or their mantle sources from either subducting crust or seawater (Figure 5-9). In addition, the Os isotopic results are consistent with radiogenic modern MORB where peridotites are variably depleted and mafic rocks are radiogenic. However, the lack of correlation between $\delta^{18}O$ and $^{187}Os/^{188}Os$ of mafic rocks (Figure 5-5) suggests that the Os isotopic compositions have not been altered by significant interaction with seawater or other hydrothermal fluid. Furthermore, although $^{187}Os/^{188}Os$ of seawater is ~ 1.06 (Levasseur et al., 1998), the radiogenic signature of the mafic rocks is not necessarily an indication of interaction with seawater insofar as the Taitao ophiolite is young and the fraction of water required to significantly alter the Os isotopic composition would need to be much greater than 100% (due to the extremely low concentration of Os in seawater; 10.86 ± 0.07 pg/kg, Levasseur et al., 1998).

Another possible way to explain the $^{187}Os/^{188}Os$ ratios includes formation of the mafic rocks in a different provenance than the peridotites. Alternately, the radiogenic values could be a mantle-derived phenomenon such that the mafic rocks formed from an already radiogenic magma. This would mean that these rocks may have been derived via partial melting of more mafic portions of the mantle (i.e., mafic veins) with higher long-term Re/Os.

In addition, the Os isotopic compositions of mafic and ultramafic samples do not overlap at the time of formation. As a result, the large range of Os isotopic compositions must reflect original isotopic heterogeneity. Because the rocks are less than 10 Ma, there is no chance that $^{187}Os/^{188}Os$ results from post-emplacement ingrowth of ^{187}Os. Consequently, the suprachondritic compositions suggest that the mafic rocks were more radiogenic than the peridotites at the time of formation. The Os isotopic compositions reported for the Taitao ophiolite thus provide additional evidence that the upper mantle is isotopically heterogeneous with respect to Os.

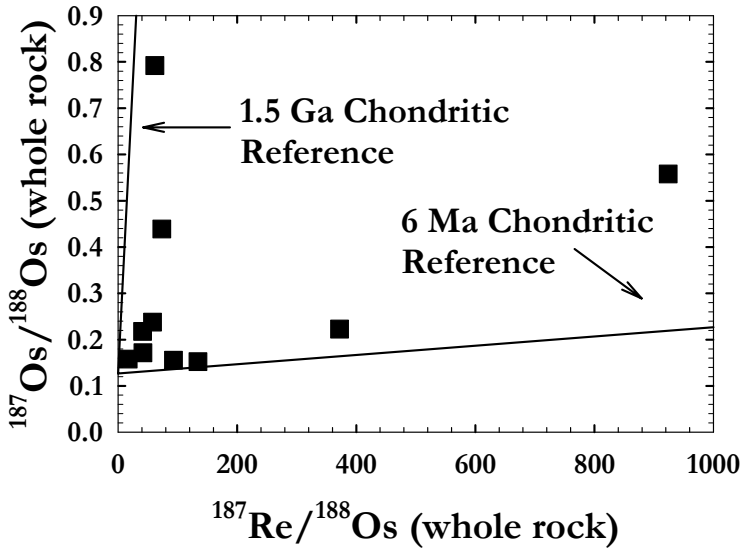

Figure 5-9. Plot of $^{187}Re/^{188}Os$ versus calculated initial $^{187}Os/^{188}Os$ of mafic whole rocks. Even rocks with high $^{187}Re/^{188}Os$ would have little ingrowth of radiogenic ^{187}Os since the putative age of formation is so young.

5-6 Sm-Nd and Rb-Sr isotope systematics

The Sm-Nd system has been found to be useful in assessing continental crustal contamination of the mantle due the preferential extraction of Sm and Nd into the continental crust. Using the ε_{Nd} notation defined by DePaolo and Wasserburg (1976) in

which initial $^{143}Nd/^{144}Nd$ isotope ratios are represented as parts per 10^4 deviation from the CHUR evolution line, the $\varepsilon_{Nd(0)}$ values of the Taitao ultramafic samples scatter widely, from -24.3 to +10.2. The average ε_{Nd} value for the continental crustal rocks assuming an mean age of about 2 Ga is -17 (Goldstein et al., 1984) whereas the DMM generally records ε_{Nd} values that range from +8 to +12 (DePaolo and Wasserburg, 1976). As a result, the range recorded by the Taitao peridotites most likely reflects metasomatic processes, which may have variably affected these rocks. For comparison, extremely depleted ultramafic whole rocks from the Voykar Massif in the Ural Mountains range from ε_{Nd} of +8.3 to +14.1 at 387 Ma and from +21 to + 47 at present day (Sharma et al, 1995). Like Taitao, the harzburgites have less than 2 wt % Al_2O_3. However, these samples have experienced little serpentinization, suggesting these rocks are relatively unaltered residues of melt extraction. In addition, the Voykar peridotites are much older than the Taitao ophiolite, which may also contribute to their high present day ε_{Nd} values.

For Taitao, there is no correlation between Os and Nd isotopic composition. The lack of a correlation suggests that the isotope systems have been decoupled from each other, perhaps during a second melting event in which Nd was reset (Figure 5-10). It is possible that some alteration may have interfered with the Os isotopic systematics in the samples with low ε_{Nd} values. However, when ε_{Nd} is compared to $\delta^{18}O$ of the olivine grains as well as the $\delta^{18}O$ of the bulk rock, the low ε_{Nd} values correspond with more mantle-like $\delta^{18}O$ values (Figures 5-11 & 5-12). The oxygen data thus provide no evidence of crustal interaction, but the Nd data may require some. Consequently, it is likely that O and Nd have been decoupled from each other.

The Rb-Sr decay scheme is another isotope system that has proven useful in identifying the influence of secondary processes on mantle rocks. In particular, the Rb-Sr system can help identify seawater contamination because ^{87}Rb decays to ^{87}Sr in crustal rocks with a half-life of ~ 4.9 x 10^{10} years. Over time, crustal Sr enters seawater via erosional processes, after which it can be incorporated into oceanic rocks that have undergone hydrothermal alteration or other interaction with seawater. In the case of the Taitao peridotites, Sr isotopic compositions range from 0.703179 to 0.707948, which is greater than the range identified by Guivel et al. (1999) in Taitao peridotites ($^{87}Sr/^{86}Sr$ = 0.702650 to 0.704394) as well as the estimate for the unfractionated Bulk Earth mantle ($^{87}Sr/^{86}Sr$ = 0.7045; DePaolo and Wasserburg, 1976).

DePaolo and Wasserburg (1976) also identified a coupled fractionation of Sm-Nd and Rb-Sr in the formation of magma sources in the mantle based on the negative correlation between $^{143}Nd/^{144}Nd$ and $^{87}Sr/^{86}Sr$ in oceanic and some continental igneous rocks. If the analyzed rocks lay to the right of this correlation, radiogenic Sr in the crust has most likely contaminated them. While there are a limited number of Sr isotope analyses, it appears as most of the samples analyzed fall within the mantle array (Figure 5-13). One sample, TPE005, clearly plots outside of the array and suggests some interaction with a crustal component.

Although the oxygen data should provide insight into any processes that may have altered the Rb-Sr isotopic signatures of the rocks, there is insufficient corresponding olivine oxygen data for a meaningful interpretation (Figure 5-14). The whole rock oxygen data show no correlation with Sr isotopic composition, supporting the idea that the oxygen and Sr isotopes are decoupled from one another (although there is limited data

with which to infer solid anti-correlations). Additionally, the lack of a solid correlation between $^{87}Sr/^{86}Sr$ and LOI suggests that these rocks have experienced little interaction with seawater (Figure 5-15).

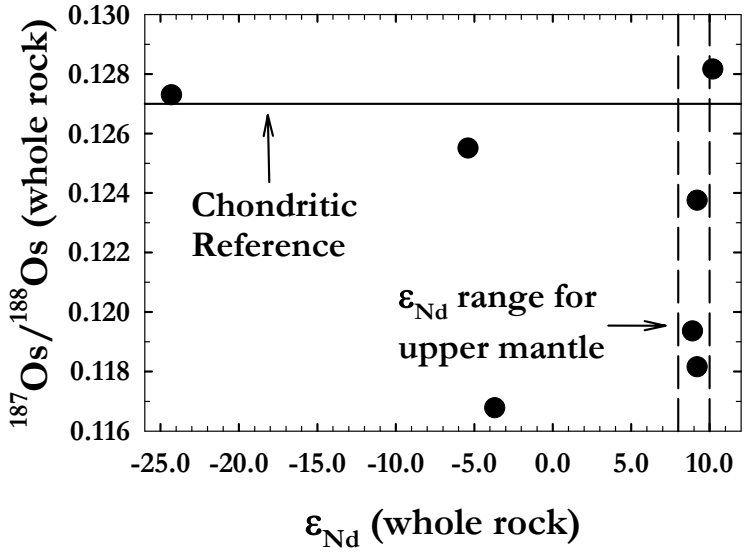

Figure 5-10. Plot of ε_{Nd} versus $^{187}Os/^{188}Os$ for whole rock peridotites. The dashed lines represent the ε_{Nd} range associated with the upper mantle.

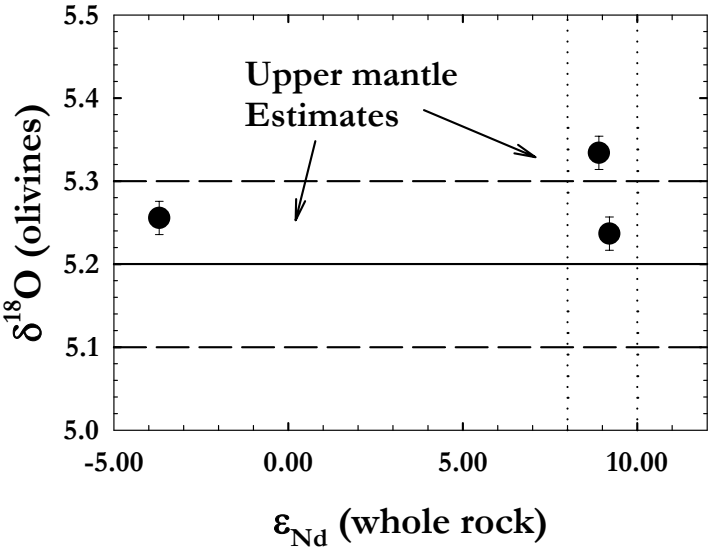

Figure 5-11. Plot of ε_{Nd} (whole rock) versus $\delta^{18}O$ (olivine grains) for peridotitic rocks. The dashed lines represent the errors associated with the upper mantle estimates. The dotted vertical lines refer to the range of ε_{Nd} values associated with the upper mantle.

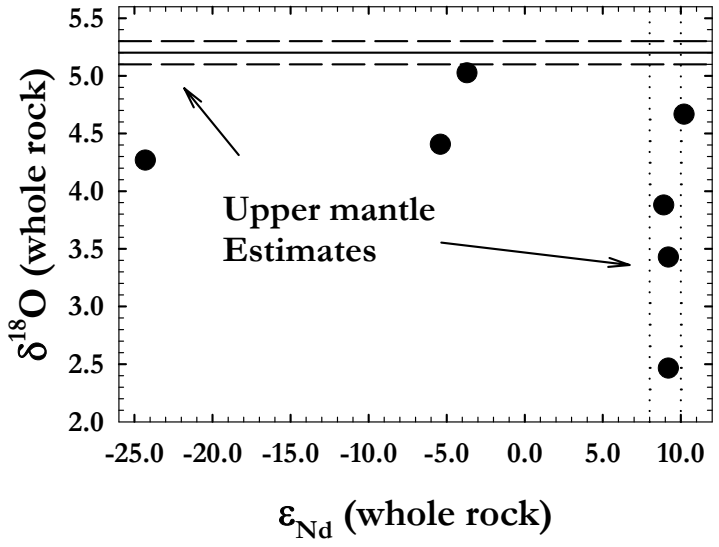

Figure 5-12. Plot of ε_{Nd} (whole rock) versus $\delta^{18}O$ (whole rock) for peridotitic rocks. The dashed lines represent the errors associated with the upper mantle estimates. The dotted vertical lines refer to the range of ε_{Nd} values associated with the upper mantle.

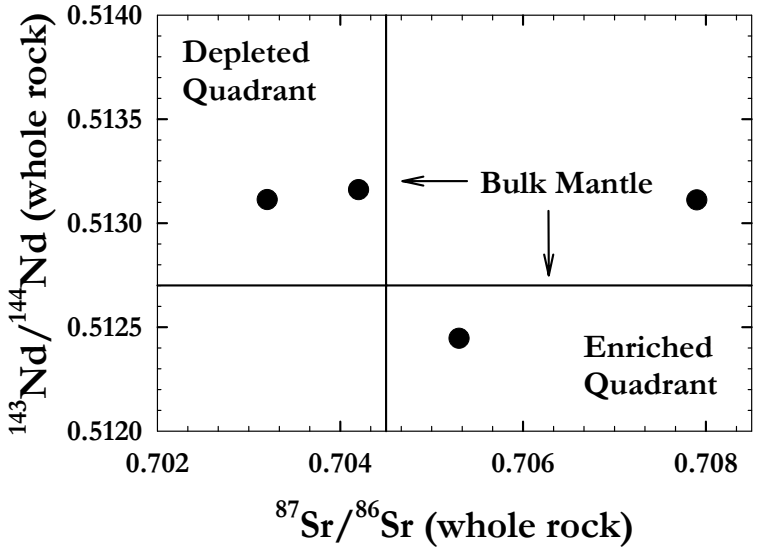

Figure 5-13. Plot of $^{87}Sr/^{86}Sr$ versus $^{143}Nd/^{144}Nd$ for whole rock peridotites. The bulk mantle values are based on DePaolo and Wasserburg (1976).

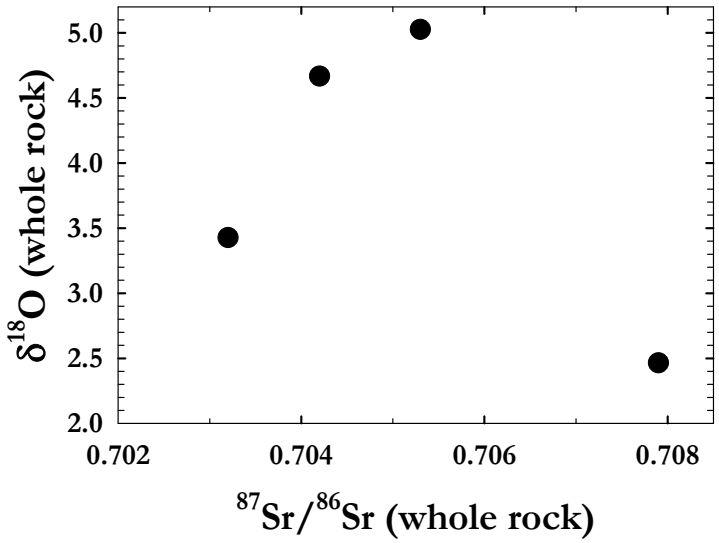

Figure 5-14. Plot of $^{87}Sr/^{86}Sr$ versus $\delta^{18}O$ for whole rock peridotites.

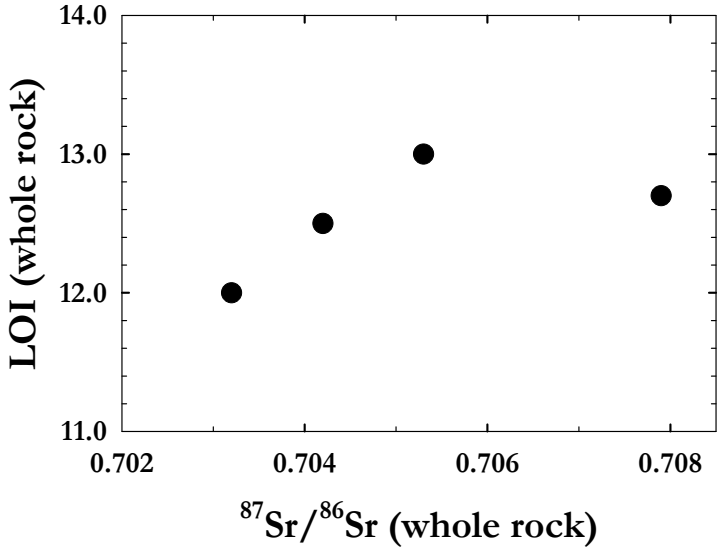

Figure 5-15. Plot of $^{87}Sr/^{86}Sr$ versus LOI for whole rock peridotites.

5-7 Implications of isotopic heterogeneities

While the correlations between melt depletion indicators and Os isotopic composition of the Taitao peridotites indicate an ancient melting event, the Al_2O_3 contents of all the peridotites are much lower than the PM estimate of ~ 4.4 wt %, which is seemingly inconsistent with ancient melting due to retention of chondritic Re/Os and present day $^{187}Os/^{188}Os$ in some samples. It is also different from most studies of SCLM xenoliths, which include samples with > 3 wt % Al_2O_3. Low Al_2O_3 contents (< 2 wt. %), however, are widely observed in abyssal peridotites (e.g., Snow et al., 2000; Harvey et al., 2006). Additionally, the Al_2O_3/SiO_2 ratios (0.02–0.04) compare favorably with dunites from the mantle-crust transition zone (MTZ) from the Oman ophiolite (0.01-0.03; Godard et al., 2000) as well as the most refractory abyssal peridotites (e.g., Niu et al., 1997; Parkinson et al., 1998; Büchl et al., 2002 and 2004), which also suggests that the low Al_2O_3 contents in the Taitao ultramafic suite are not atypical for rocks from the DMM.

Other indicators of melt depletion, like Mg # and CaO, suggest different degrees of melt depletion (Table 1; Figure 4-1). For example, the Mg #'s of the whole rock are closer to the PM estimate of 0.88, while CaO is, in most cases, even more depleted than Al_2O_3. Pervasive marine weathering (Snow and Dick, 1995) can potentially produce very low Al_2O_3 values in peridotites. However, there is insufficient petrologic evidence in the Taitao ultramafic suite (e.g., very high degrees of serpentinization for all rocks) to support this idea. Moreover, the linear correlation between Al_2O_3 and MgO argues against secondary alteration as a cause of the extreme Al_2O_3 depletions (Figure 4-3) insofar as MgO is much easier to alter than Al_2O_3.

One explanation for the observation is that the mantle region from which the Taitao peridotites were formed was depleted in Al_2O_3 very early in earth history. There is no geochemical or geophysical reason, however, why a primordial Al_2O_3-depleted region in the primitive mantle should remain distinct from the bulk mantle.

Another possible explanation for the observed $^{187}Os/^{188}Os$- Al_2O_3 correlation may involve reintroduction of Re to the mantle block, such that radiogenic ingrowth could reach near chondritic $^{187}Os/^{188}Os$ levels without altering the Al_2O_3 contents. In this case, a massive early depletion event would have had to occur and then been almost immediately followed by Re addition (without Al) in order to establish the observed errorchron and more chondritic Os isotopic compositions (Figure 5-6). The probability of this model seems unlikely given that a melt or fluid transporting the Re would most likely also contain Al, thus destroying the previous $^{187}Re/^{188}Os$-$^{187}Os/^{188}Os$ correlation. More importantly, the low Re contents and subchondritic $^{187}Re/^{188}Os$ ratios of the peridotites seemingly rule this option out.

Snow et al. (2000) found nearly constant Al_2O_3 with increasing and slightly subchondritic $^{187}Os/^{188}Os$ ratios in the Internal Liguridian peridotites, which they to be a byproduct of an early partial melting event that was sequestered in the upper mantle for a period of time before being re-melted near the mid-ocean ridge. The initial melt would have exhibited an $^{187}Os/^{188}Os$-Al_2O_3 correlation but re-melting would have altered the Al_2O_3 concentration without homogenizing the Os isotopes. Their results differ from the trends recorded in the Taitao peridotites in that none of their $^{187}Os/^{188}Os$ ratios are as depleted, and their Al_2O_3 concentrations are higher and essentially constant.

We speculate that Taitao peridotites experienced a two-stage melting history similar to the Inner Ligurides of Snow et al. (2000). The most likely scenario for the formation of the Taitao peridotites would thus involve: 1) an initial, variable melt extraction at ~ 1.5 Ga and 2) a second, recent melting event that further depleted the mantle domain in Al_2O_3 without perturbing the Os isotopic signature, Re/Os or V contents. In addition, the degree of melt depletion would have to correlate with the amount of Al available in the residue in order to preserve the Al_2O_3 vs. $^{187}Os/^{188}Os$ correlation (Figure 5-17). Rocks with higher amounts of Al_2O_3 would give up proportionally more Al during the second melting event. The problem with this model is that the second melting event should most likely destroy the linear correlation between $^{187}Re/^{188}Os$ and $^{187}Os/^{188}Os$.

The Re-Os isochron (or 'errorchron') could also be considered as a mixing line between a modern chondritic reservoir and an ancient depleted reservoir, but this still would not explain why chondritic $^{187}Os/^{188}Os$ was preserved in rocks with extremely low Al_2O_3.

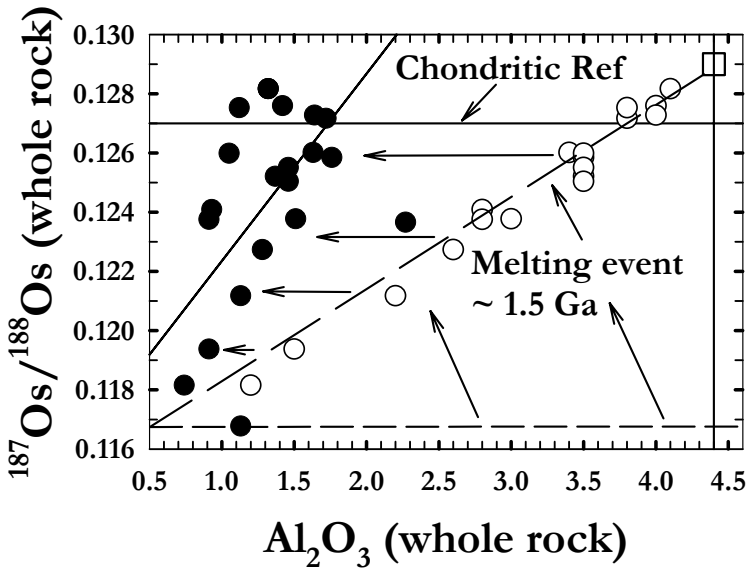

Figure 5-16. Plot of anhydrous whole rock Al_2O_3 versus bulk $^{187}Os/^{188}Os$ with hypothetical Al_2O_3 values (open circles) that might have existed prior to the postulated second melting event in recent times. The dashed horizontal line represents the Os isotopic composition prior to melt removal.

CHAPTER 6: CONCLUSIONS

The observed Os isotopic heterogeneity in the Taitao Ophiolite is consistent with those seen in abyssal peridotites, peridotite massifs, peridotitic xenoliths and other ophiolites. Unlike abyssal peridotites, dissociated ophiolitic bodies and SCLM, however, the Taitao Ophiolite is young at ~ 6 Ma and well mapped, with known tectonic associations such that the distribution of heterogeneities can be more readily observed. The $^{187}Os/^{188}Os$ ratios of the ultramafic rocks are chondritic to subchondritic while the mafic rocks are suprachondritic. Due to the young age of the ophiolite, it must follow that the Os isotopic compositions of the different bodies did not overlap at the time of formation. A negative correlation between Mg # of the olivines and Os isotopic composition of the peridotites suggests that there was an ancient melting event at ~1.5 Ga. This is also supported by a linear correlation between $^{187}Re/^{188}Os$ and $^{187}Os/^{188}Os$. The fact that some peridotites have modern chondritic $^{187}Os/^{188}Os$ ratios and are also highly depleted in Al relative to PM is problematic and most likely requires a two-stage model: 1) initial melt depletion at 1.5 Ga and 2) a more recent melting event in which Al_2O_3 was removed without significantly disturbing the previously established Re/Os and Mg # trends. Nevertheless, the $^{187}Os/^{188}Os$-Mg# correlation requires that a block of upper mantle experienced an ancient melting event at ~1.5 Ga and then remained isolated within the convecting upper mantle without perturbation until obduction onto the continental surface. This is the first example of such an event for the DMM.

APPENDIX 1: TABLE OF MODAL MINERALOGY

Sample	Ol	Opx	Cpx	Cr-Spi	Srp	Mt	Chl	Plag	Src	Other
Ultramafic Rocks:										
TPE124	805	10	5	5	65	10				
TPE068	8010	10	5	5	58	10	2			
TPB120	7545	6	4	5	30	10				
TPE029	703	15	3	10	60	5	2			2 (amph)
TPE033	7840	17	0	5	30	5				3 (act)
TPG001	661	12	7	15	43	22				
TPG049	7510	20	0	5	55	10				
TPH053	8020	0	12	8	50	10				
TPB116	772	8	12	3	65	10				
TPE005	830	7	0	10	73	8	2			
TPB016	6730	12	11	10	32	5				
TPG091	7515	20	0	5	50	10				
TPB010	7533	10	10	5	40	2				
TPG050	8015	17	0	3	60	5				
TPG068	7717	10	5	8	50	10				
TPG036	783	10	7	5	60	10				5 (amph)
TPB127	8010	5	5	10	50	20				
TPG005	805	10	5	5	70	5				
TPE010	77	13	5	5	50	5				2 (amph)

	20									
TPE024	87	5	10	8	55	10	2			
	10									
Contact Rocks:										
TPH069	80	10	5	5	50	20				
	10									
TPE004-prd	80	10	0	10	40	10				
	30									
TPE004-gb			50			5	10	10	15	
TPH065	80	10	5	5	60	20				
	0									
Ultramafic Dike:										
TPE027	78	6	3	10	7	5				3 (hrn)
	66									
Mafic Rocks:										
TPB042			35					60		5 (hrn)
TPB040							2	38		60 (hrn)
TPB046			30		10			30		30 (hrn)
TPB023 (TPG023)								95		5 (il)
TPH063			30					20	50	
TPE063								40	30	20 (amph)
										10 (tlc)

Primary olivine abundances are listed above relict abundances. Mineral symbols: ol - olivine, opx – orthopyroxene, cpx – clinopyroxene, cr-spi – chromium spinel, srp – serpentine (group), mt – magnetite, chl – chlorite, plag – plagioclase, src – sericite, act – actinolite, amph – amphibole, hrn –hornblende, il – ilmenite, and tlc – talc

APPENDIX 2: THIN SECTION DESCRIPTIONS

Ultramafic rocks:

TPE124. Tectonite. Primary minerals include olivine, chromite, pyroxene and chromite. Olivine crystals were originally ~ 1cm in diameter and 80% in abundance. Relict olivine grains are 0.5mm or less, predominantly oval-shaped and less than 5% in abundance. Chromite grains (5%) are anhedral with lacy edges and 0.5-2 mm in diameter. Both clinopyroxene and orthopyroxene (enstatite) are present, with enstatite slightly higher in abundance (10%) than clinopyroxene (5%). Orthopyroxene grains are pale in color, 1-3 mm in diameter and subhedral on average. Smaller enstatite grains, less than 0.5 mm, are also scattered throughout the thin section. Clinopyroxene grains average 1-3 mm diameter and are subhedral. Over half of the rock is serpentinized (65%). Secondary minerals include serpentine and magnetite (10%). A 4-5 mm serpentine vein cuts across the thin section and is flanked by well-preserved olivine, clinopyroxene, magnetite and chromite grains. Magnetite is located within the serpentinized portions of the rock as well as along cleavage planes in some pyroxenes and olivines.

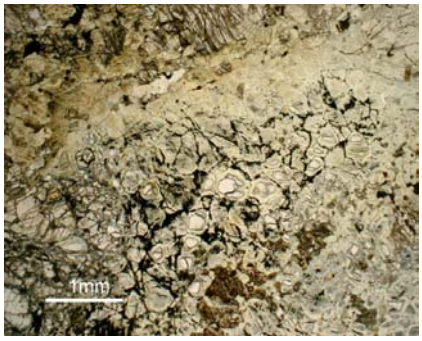

_____ 1 mm

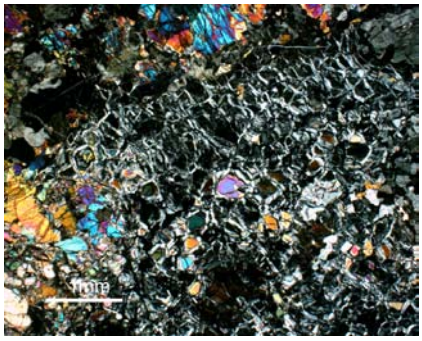

_____ 1 mm

TPE068. Peridotite lens. The primary minerals in this rock are olivine (80%), pyroxene (15%), and chromite (5%). Original olivine was 1-2 cm in diameter. Most of the remaining olivine (10%) is 0.5 mm or less and oval to subangular in habit. The orthopyroxene and clinopyroxene are ~ 2 mm on average, though there is a clinopyroxene grain as large as 6 mm. Chromite grains are generally 0.5 mm or less and anhedral with feathery, lacy edges. Secondary minerals include serpentine (58%), magnetite (10%), and chlorite (2%). The magnetite occurs in veins as well as along fractured cleavage planes in the pyroxene crystals.

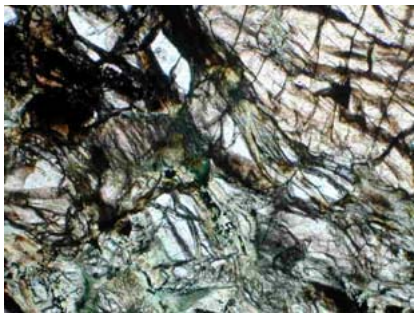

_____ 1 mm

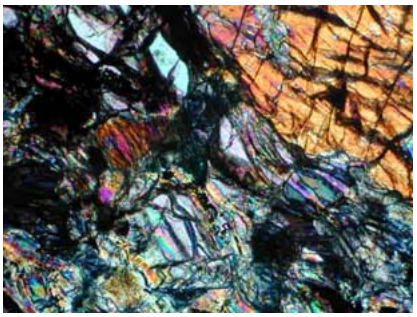

_____ 1 mm

TPB120. Harzburgite/Tectonite. Primary minerals include olivine (75%), orthopyroxene (6%), clinopyroxene (4%), and chromium spinel (5%). Original olivine was 0.5 – 1 cm in diameter. The relict olivine is well-preserved, 45% in abundance, subhedral, and typically 0.25 mm or less and scattered randomly throughout the thin section. The pyroxenes are 1-3 mm in diameter and subhedral to anhedral in shape, with clinopyroxene generally smaller and less abundant than orthopyroxene. Chromite grains are anhedral with lacy edges and reddish-brown interiors, and 0.5 mm in diameter or less. The secondary minerals serpentine and magnetite are 30% and 10% in abundance, respectively; and occasionally occur in veinlets.

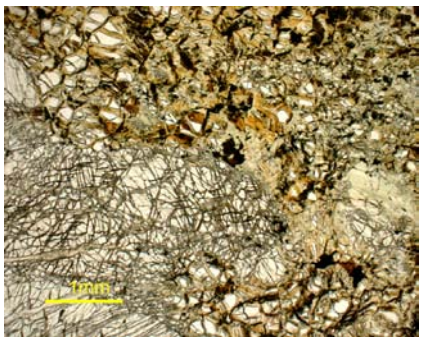

_____ 1 mm

_____ 1 mm

TPE029. Harzburgite. Primary minerals include olivine (70%), orthopyroxene (15%) and chromite (10%). Relict olivine crystals are rare (3%), 0.1 mm in diameter and subhedral in habit. Original olivine grains were 0.5 – 1 cm in diameter. Chromite is ~ 0.5 mm, subhedral to anhedral with reddish-brown interiors and black, lacy edges, though there are a few grains as large as 1 mm. The orthopyroxene (2-4 mm) is in most cases surrounded by the secondary mineral amphibole (2%) or clinopyroxene (3%), with replacement often evident around the edges. Other secondary minerals include serpentine (60%), chlorite (2%), and magnetite (5%).

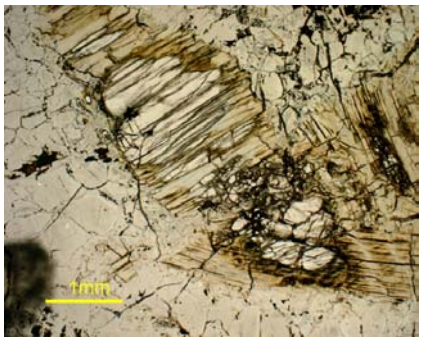

_____ 1 mm

_____ 1 mm

TPE033. Harzburgite. Primary minerals include olivine (78%), orthopyroxene (17%) and chromium spinel (chromite) (5%). Original olivine grains were 0.5 – 1 cm in diameter. Relict olivine (40%) is well preserved, 0.25 mm or less, and colorless with subhedral, angular habits. The chromite is reddish-brown in color, anhedral with rounded or lacy edges. Most of the grains are 0.5 mm or less, some of which are situated within pre-existing orthopyroxene crystals. The smaller grains tend to be more rounded in shape. Orthopyroxene crystals are 2-4 mm in diameter, though some are as small as 1 mm. Secondary minerals include serpentine (30%), magnetite (5%) and actinolite (3%). The magnetite occurs mostly in semi-parallel veins that cut across the thin section.

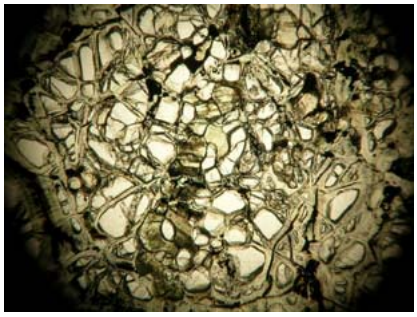
_____ 1 mm


_____ 1 mm

TPG001. Peridotite. Primary minerals include olivine (66%), orthopyroxene (12%), clinopyroxene (7%) and chromite (15%). Primary olivine grains were ~1 cm in diameter. Remaining olivine crystals (~1%) are subhedral and 0.25 mm or less. Chromite grains are reddish-brown with black trim, 1 mm in diameter on average, and anhedral or subhedral in shape. Orthopyroxene grains are often grungy and surrounded by clinopyroxene rims in some places. Secondary minerals include serpentine (43%) and magnetite (22%). The magnetite occurs mostly as thin veinlets, 0.25 mm thick, and along cleavage planes in some pyroxenes.

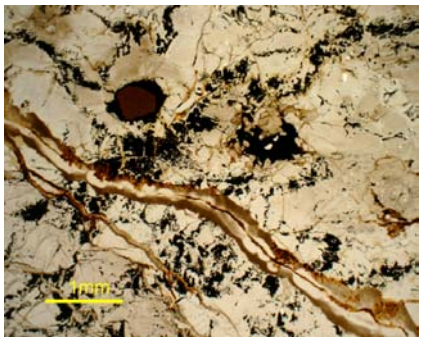

_____ 1 mm

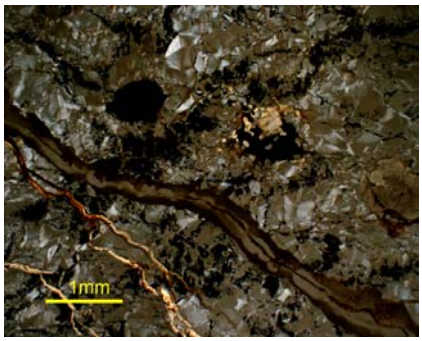

_____ 1 mm

TPG049. Peridotite. Primary minerals include olivine (75%), chromite (5%), and orthopyroxene (20%). Original olivine was 1-2 cm in diameter. Relict olivine crystals (10%) are scattered throughout the rock as tiny blebs, 0.25 mm or less in diameter, subhedral and oval-shaped. Chromite grains are less than 0.25 mm on average and anhedral with lacy edges. Orthopyroxene crystals are highly fractured, 1-2 mm in diameter and mostly subhedral. More than half the rock is serpentinized (55%) and contains the secondary mineral magnetite (10%). Magnetite occurs with serpentine, particularly along serpentine veins and in fractures surrounding olivine.

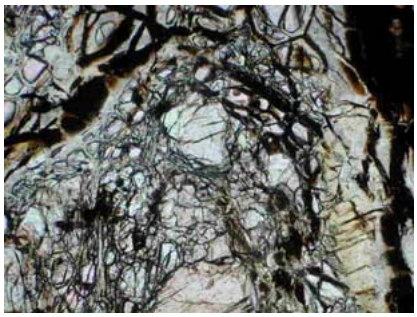

_____ 1 mm

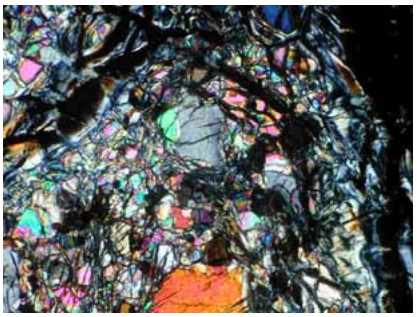

_____ 1 mm

TPH053. Peridotite. This rock consists of the primary minerals olivine (80%), clinopyroxene (12%), and chromium spinel (8%). Original olivine grains were ~2 cm in diameter. The remaining olivine grains are ~ 0.5 mm in diameter or less, 20% in abundance, and subhedral in habit. Clinopyroxene is 1- 3 mm in diameter with rounded edges. Chromite is ~ 0.5 mm or less, though there are a few grains as large as 1 mm. The interiors are reddish-brown and crosscut and surrounded by black lacy rims. Serpentine (50%) and magnetite (10%) comprise the secondary minerals.

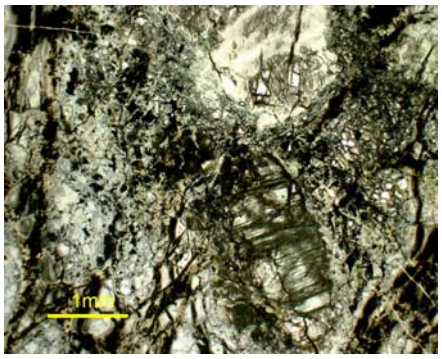

_____ 1 mm

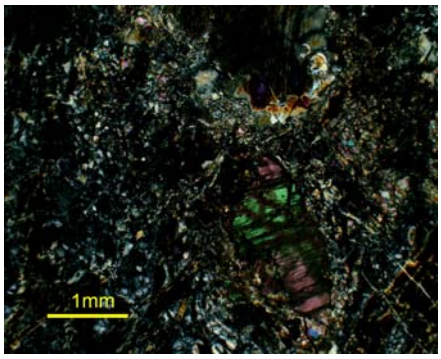

_____ 1 mm

TPB116. Peridotite. The rock is almost completely serpentinized (65%) with only 2% olivine crystals remaining intact. Primary olivine was 77% in abundance and ~ 1 cm in diameter. The relict olivine grains are mostly subhedral, oval-shaped and 0.25 mm or less in diameter. Both orthopyroxene (8%) and clinopyroxene (12%) are present, each roughly 1-2 mm in diameter and subhedral. Chromite grains, ~ 3% in abundance, are less than 0.5 mm on average, and anhedral with lacy edges. There is one 1-mm-sized, subhedral chromite grain with a mostly reddish-brown interior that is crosscut and surrounded by black, Fe-rich veins. The secondary mineral magnetite (10%) fills fractures and cleavage planes within the pyroxenes and possibly larger chromite grains.

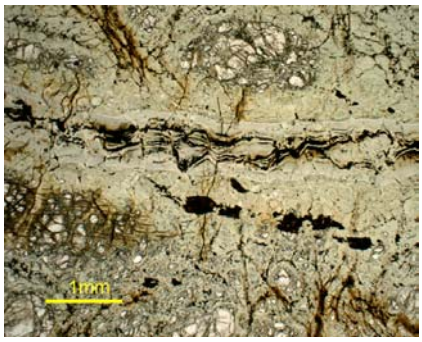

_____ 1 mm

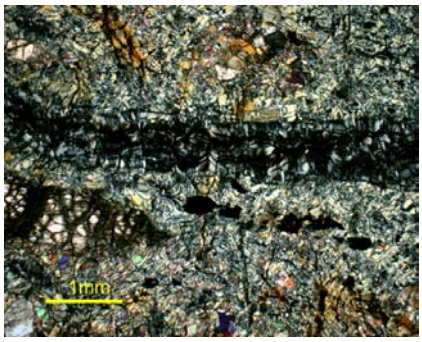

_____ 1 mm

TPE005. Harzburgite. Primary minerals include olivine (83%), oikocrystic orthopyroxene (7%), and spinel (10%). There is no olivine remaining in this thin section. Original olivine was 1-3 cm in diameter. Orthopyroxene is 1-3 mm in diameter on average with rounded, subhedral habits. Chromite grains are predominantly 0.25 mm or less and anhedral with lacy edges. The interiors are reddish-brown. A few grains are as large as 1 mm, though these are rare. Secondary minerals include serpentine (73%), magnetite (8%), and chlorite (2%). Veins of serpentine are generally ~ 0.25 mm thick. Magnetite is scattered throughout the thin section and also occurs in veinlets surrounding other minerals.

_____ 1 mm

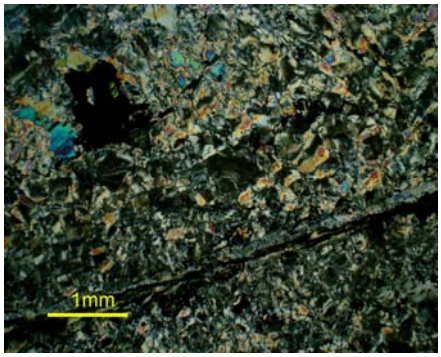

_____ 1 mm

TPB016. Peridotite. Primary minerals include olivine (67%), orthopyroxene (12%), clinopyroxene (11%), and spinel (10%). The original olivine grains were ~2 cm in diameter. Most of the remaining olivine grains (30%) are serpentinized around the edges, subhedral in shape and < 0.25 mm in size. Orthopyroxene grains are 3-5 mm on average and often display kinkbands. Clinopyroxene is generally ~ 2mm and very rounded in shape. Chromium spinel is reddish-brown to brown in color with lacy edges and anhedral in habit. Secondary minerals include serpentine (32%) and magnetite (5%).

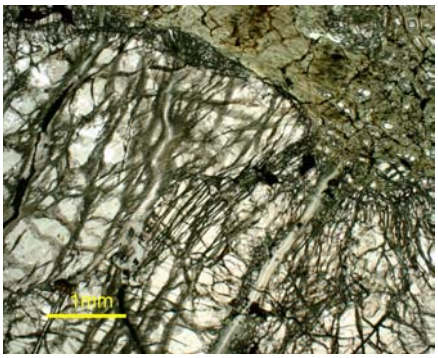

_____ 1 mm

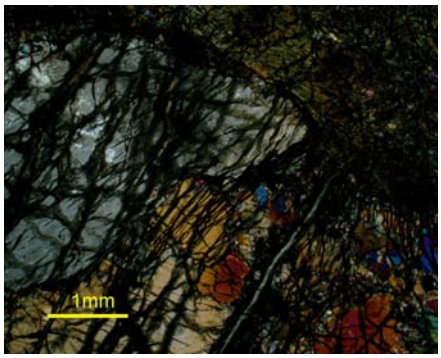

_____ 1 mm

TPG091. Orthopyroxene-rich harzburgite. Primary minerals include olivine (75%), chromite (5%), and orthopyroxene (20%). Original olivine grains were 1-2 cm in diameter. Remnant olivine crystals are scattered throughout the rock as tiny blebs, 15% in abundance, 0.25 mm or less in diameter, subhedral and oval-shaped. Chromite grains occur in small clusters or are randomly scattered throughout the rock. On average, they are less than 0.25 mm, anhedral with lacy edges, and reddish-brown in color. Orthopyroxene crystals are highly fractured, 1-2 mm in diameter and mostly rounded and subhedral in habit. Half the rock is serpentinized (50%) where the serpentine replaces olivine and also occurs in 1-4 mm veins along with the mineral magnetite (10%). Magnetite is also located along cleavage planes in some pyroxenes and olivines.

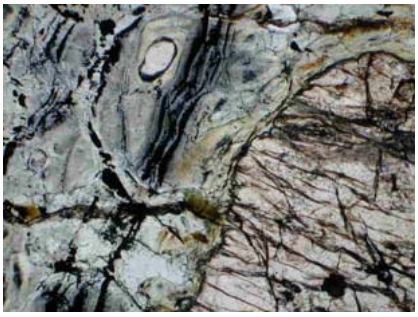

_____ 1 mm

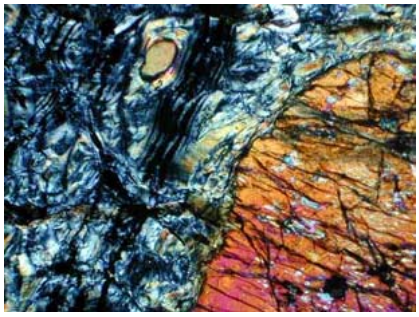

_____ 1 mm

TPB010. Peridotite. Primary minerals include olivine (75%), orthopyroxene (10%), clinopyroxene (10%), and chromium spinel (5%). Olivine was originally ~ 2 cm in diameter. The relict olivine crystals (33%) are subhedral in habit and < 0.25 mm in diameter. Orthopyroxene and clinopyroxene are 3-6 mm in diameter on average. The chromite grains are ~ 0.5 mm or less in diameter, reddish-brown in color, anhedral, and often in clusters surrounding larger, fractured olivine grains. Secondary minerals include serpentine (40%) and magnetite (2%).

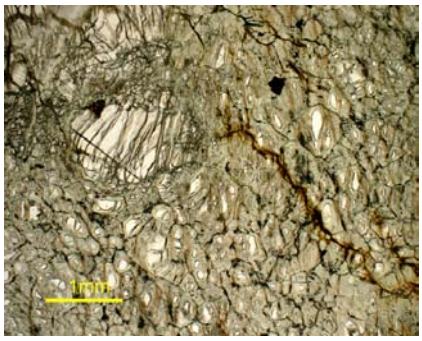

_____ 1 mm

_____ 1 mm

TPG050. Orthopyroxene-rich peridotite. Primary minerals include olivine (80%), chromite (3%), and orthopyroxene (17%). Olivine grains were originally 1-2 cm in diameter. Remnant olivine crystals are 15% in abundance, scattered throughout the rock as tiny blebs, 0.25 mm or less in diameter, subhedral and oval-shaped. Chromite grains are less than 0.25 mm on average and anhedral with lacy edges, though some are as large as 1 mm. Orthopyroxene crystals are highly fractured, 1-2 mm in diameter and mostly subhedral. More than half the rock is serpentinized (60%) and contains the secondary mineral magnetite (5%). Magnetite occurs with serpentine, particularly along serpentine veins and in fractures surrounding olivine and orthopyroxene grains.

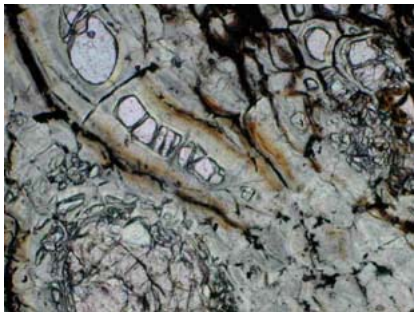

_____ 1 mm

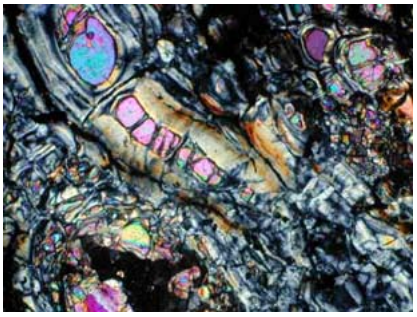

_____ 1 mm

TPG068. Harzburgite. The primary minerals in this rock consist of olivine (77%), ortho- and clinopyroxene (15% total), and chromite (8%). Original olivine was ~ 2 cm in diameter. Relict olivine (17%) is ~ 0.55 mm, sometimes less, and oval in shape. There are a few grains as large as 1 mm. The orthopyroxene ranges 2-6 mm in diameter, but most are ~ 4 mm. There is one very large orthopyroxene crystal (10 mm) that encloses a pre-existing olivine matrix. Clinopyroxene grains are smaller, only ~ 1 mm in diameter. Secondary minerals include serpentine (50%) and magnetite (10%).

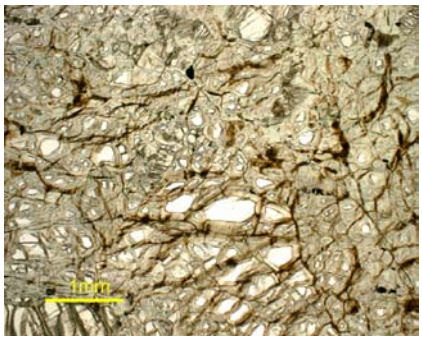

_____ 1 mm

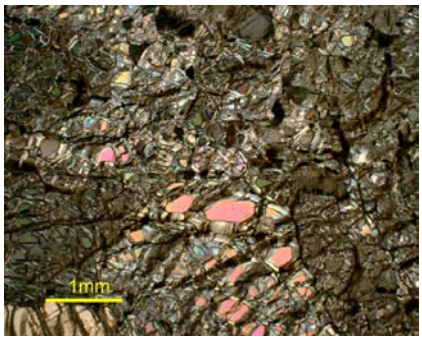

_____ 1 mm

TPG036. Peridotite. Olivine (78%), orthopyroxene (10%), clinopyroxene (7%), and chromite (5%) make up the primary minerals in this rock. Primary olivine was 2-3 cm in diameter. The relict olivine (3%) is mostly 0.25 mm in diameter, subhedral and subangular. Orthopyroxene and clinopyroxene are both 1-2 mm with rounded, subhedral shapes. The chromite is 05 mm or less with feathery, anhedral edges and reddish-brown interiors. Serpentine (60%), magnetite (10%) and amphibole (5%) comprise the secondary minerals. In general, the amphibole surrounds pre-existing clinopyroxene grains.

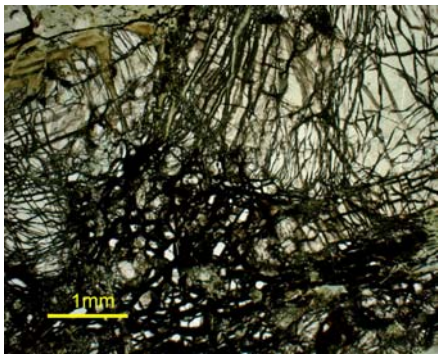

_____ 1 mm

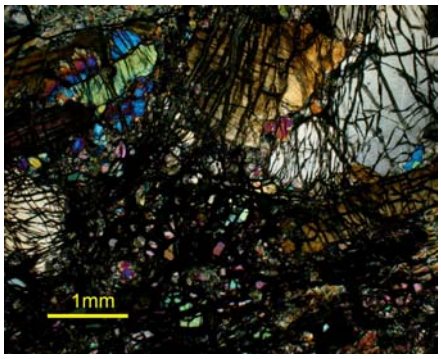

_____ 1 mm

TPB127. Tectonite. The rock is moderately serpentinized at 50% with extensive magnetite veinlets cross-cutting the thin section, some as large as 0.25-0.5 mm thick. Magnetite, including the veinlets, comprises 20% of the rock. Minimal primary olivine grains remain (only ~10%) and are 0.1 mm in diameter. The original shape of original olivine grains is occasionally evident, however, and suggests that olivine was once ~2 cm in diameter. Primary abundance of olivine was 80%. Chromite (10%) is predominantly located along magnetite-serpentine veinlets. Chromite grains are 0.25 mm or less on average (though a few grains are as large as 1 mm) and sub- to anhedral with reddish-brown interiors that are crosscut and surrounded by black, Fe-rich veins. Both orthopyroxene and clinopyroxene are present. The orthopyroxene is mostly enstatite (5%) and 2-4 mm diameter on average, though several grains are as large as 8 mm. Clinopyroxene is 5% in abundance and ~1 mm in diameter with high second-order birefringence.

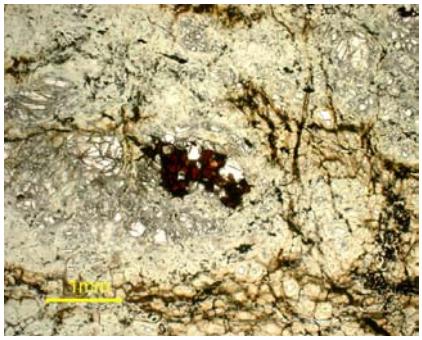

_____ 1 mm

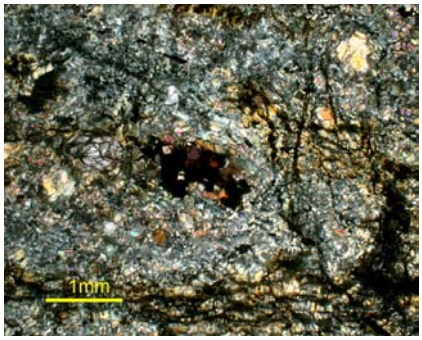

_____ 1 mm

TPG005. Peridotite. Hand specimen examination reveals heavily serpentinized olivine grains in an ultramafic massive body. Primary minerals include olivine (80%), pyroxene (15%) and chromite (5%). Original olivine grains were ~ 2 cm in diameter. The relict olivine grains (5%) are highly fractured, and mostly 1-4 mm across, with a few very small blebs (<1 mm) scattered throughout the sample. Chromite grains are 0.25 mm or less on average, anhedral, and have reddish-brown interiors with black, lacy rims. The secondary minerals serpentine (70%) and magnetite (5%) are usually located around fractured olivine crystals or in veins that crosscut the sample.

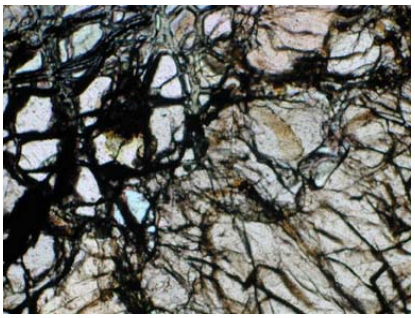

_____ 1 mm

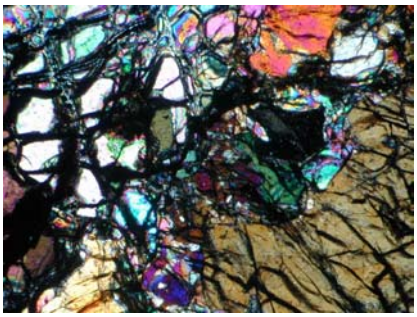

_____ 1 mm

TPE010. Harzburgite. Primary minerals include olivine (77%), orthopyroxene (13%), clinopyroxene (5%), and spinel (5%). The olivine grains were originally 1-3 cm in diameter. Relict olivine crystals (20%) are 0.25 mm or less in diameter, subhedral and oval-shaped and scattered throughout the thin section. Orthopyroxene and clinopyroxene are on average 1-3 mm in diameter. Chromite grains are less than 0.25 mm with a few as large as 1 mm, and anhedral with lacy edges. Secondary minerals include serpentine (50%), magnetite (5%) and amphibole (2%). Two parallel veins of serpentine, 0.25 mm thick, cut across the thin section. Occasional nodules of serpentine occur along the veins, 0.5 mm to 1 mm in diameter.

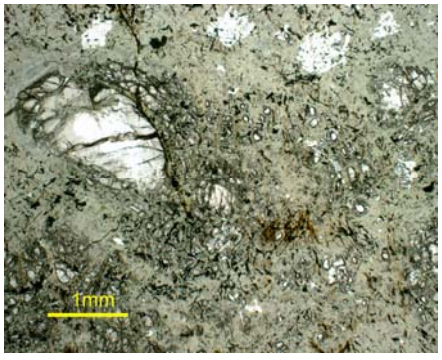

_____ 1 mm

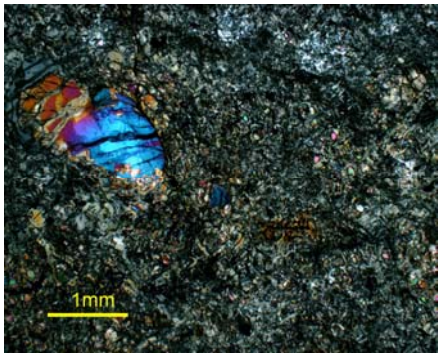

_____ 1 mm

TPE024. Harzburgite. Olivine (87%), clinopyroxene (10%), orthopyroxene (5%), and chromium spinel (8%) comprise the primary minerals in this rock. Original olivine grains were about 1-2 cm in diameter. Remnant olivine grains (10%) are rounded and ~ 0.25 mm or less in diameter. The clinopyroxene and orthopyroxene are 1-2 mm, highly fractured, and subhedral in habit. Magnetite and serpentine fill the fractured cleavage planes in the pyroxenes. Serpentine (55%) makes up the bulk of the secondary minerals. Magnetite (10%) can also be found in veinlets and as anhedral crystals. Chlorite (2%) is found in association with serpentine veins.

_____ 1 mm

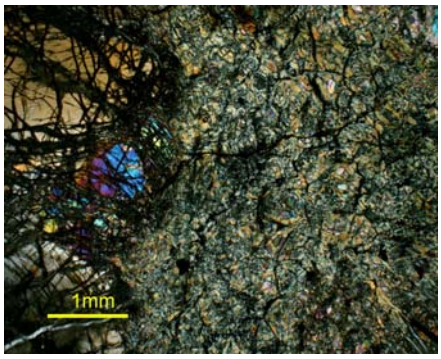

_____ 1 mm

Contact Rocks:

TPH069. Contact between peridotite and gabbro. The peridotite contains primary olivine (80%), pyroxene (15-18%), and chromite (<5%) Secondary minerals include serpentine (50%) and magnetite (20%). Primary olivine grains were 1-2 cm in diameter. Relict olivine grains (10%) are preserved as tiny blebs that are ~0.25 mm. The pyroxene grains are mostly orthopyroxene, 2-3 mm diameter on average with some as small as 0.5 mm and others as large as 5-6 mm. Clinopyroxene grains are similar in size and shape, though much less in abundance. Chromite crystals are subhedral to anhedral, and 0.5-1 mm on average. Magnetite is anhedral and occurs mostly within and alongside serpentine veins as well as around relict olivine.

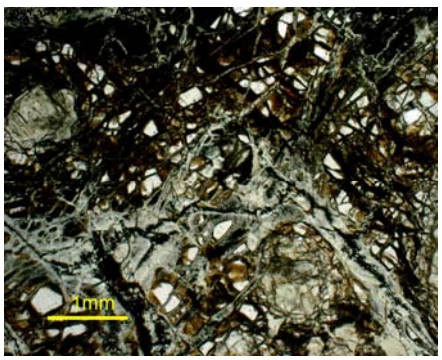

_____ 1 mm

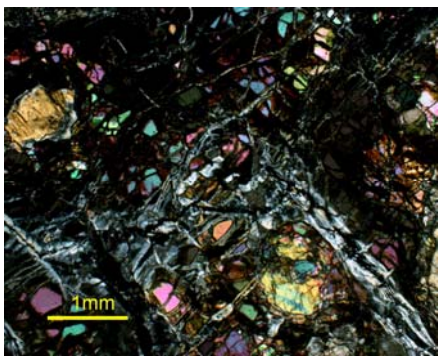

_____ 1 mm

TPE004. Contact between gabbro dike and peridotite. The peridotite portion of the sample contains about 80% olivine, which was originally ~ 1 cm in diameter. Only 30% of the olivine still remains, and is 0.5 to 1 mm in diameter and rounded in habit. Pyroxene is 10% in abundance. Disseminate chromite (10%) is also present, subhedral and 0.25 – 1 mm in diameter. Magnetite (10%) occurs with serpentine (40%) in parallel veins that cut across the thin section. The gabbro portion of the rock consists mostly of large clinopyroxene grains (50%) that are subhedral and 1-3 mm in diameter. Primary plagioclase is also present, at about 10%, and 0.25 - 1 mm in diameter. Secondary minerals include chlorite (10%) and sericite (15%). The chlorite is anhedral, massive, approximately 4 mm wide, and contains magnetite inclusions (which are ≤0.25 μm in diameter and 5% in total abundance).

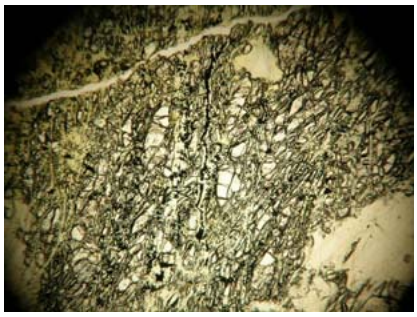

_____ 1 mm

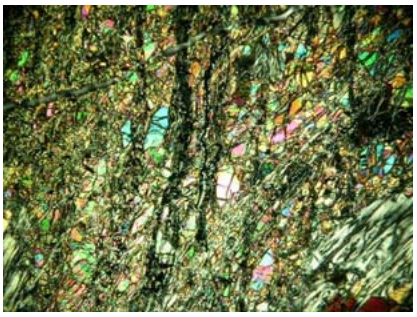

_____ 1 mm

TPH065. Peridotite pod in gabbro body. There are no relict olivines present in this thin section. Original olivine abundance was 80% and ~2 cm in diameter. Clinopyroxene and orthopyroxene (15%) are 3-5 mm in diameter and grungy with subhedral habits. Chromite grains (5%) are as large as 1 mm, sometimes less, and possess anhedral habits with lacy edges. Serpentine (60%) and magnetite (20%) make up the rest of the rock.

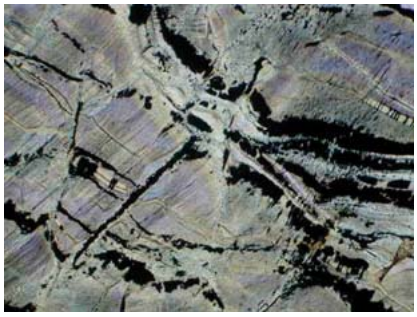

_____ 1 mm

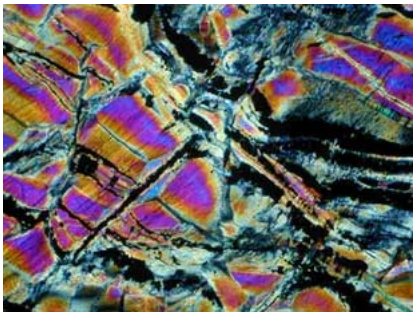

_____ 1 mm

Ultramafic Dike:

TPE027. Peridotitic dike. Hand specimen examination reveals mostly disseminate chromites within an olivine mass and a few layered chromite bands, ~ 3mm thick. Primary minerals include olivine (78% with 66% still remaining), and clino- and orthopyroxene (9% total). The relict olivine is well preserved, euhedral to subhedral in habit, and 0.25-1 mm in diameter. Primary olivine was probably 2-3 cm in diameter. The secondary mineral serpentine is minimally abundant at 7%, and often occurs in veins along with the mineral magnetite (5% in abundance overall). Pyroxene grains are 1.5 to 2 mm in diameter on average, as small as 0.25 mm and as large as 4 mm. The largest pyroxene grains exhibit exsolution lamellae. Chromite is randomly distributed throughout the thin section, mostly reddish-brown in color, subhedral to anhedral with lacy edges, 0.25 mm – 1 mm on average, and comprises 10% of the total rock. A minor amount of hornblende is also present (3%), 10-30 mm in diameter, and is usually located near serpentine-magnetite veins.

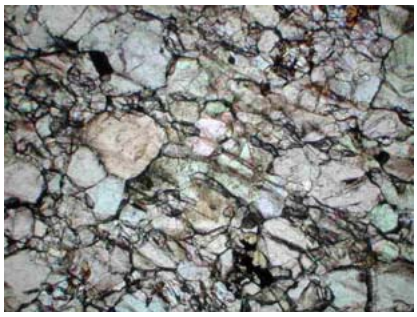

_____ 1 mm

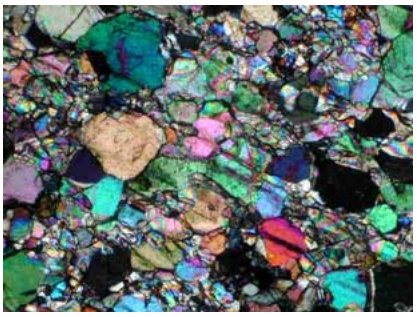

_____ 1 mm

Mafic rocks:

TPB042. Weakly-foliated gabbro. Plagioclase is the most abundant mineral in the rock at 60% with euhedral and hexagonal habits. Clinopyroxene comprises 35% of the rock, is grungy in most places and occurs mostly in two parallel veins that cut across the thin section. A minor amount of hornblende (5%) is found around the clinopyroxene veins.

_____ 1 mm

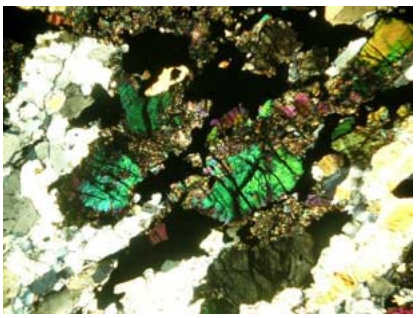

_____ 1 mm

TPB040. Layered gabbro. Primary minerals include plagioclase (38%), which is anhedral and grungy in most places. There are two parallel veins of amphibole, each about 5 mm thick. The amphibole grains have pale brown centers and green edges and comprise 60% of the thin section. Magnetite also occurs in this rock, at 2% modal abundance.

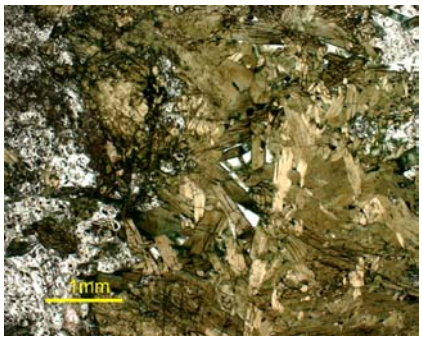

_____ 1 mm

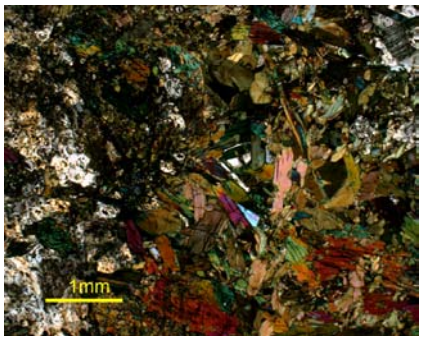

_____ 1 mm

TPB039. Basalt. No thin section.

TPB046. Pegmatitic gabbro with poikilitic texture. Plagioclase is the most abundant mineral at 75%. The grains are 1 mm on average with subhedral, tabular habits. A few plagioclase crystals are as large as 6 mm. Secondary clinopyroxene grains (20%) are 2-6 mm in diameter, grungy, fractured and anhedral with chloritized edges (3%). Clinopyroxene and chlorite also occur in veins (~ 0.5 mm thick) that extend from some of the larger clinopyroxene grains and crosscut the thin section. Many of the clinopyroxene grains are also oikocrystic. Chlorite contains tiny magnetite inclusions (2%) that are ~ 0.25 μm or less and mostly euhedral in habit.

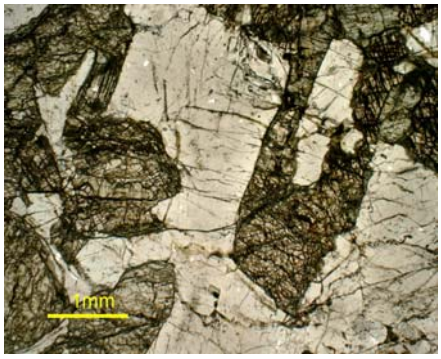

_____ 1 mm

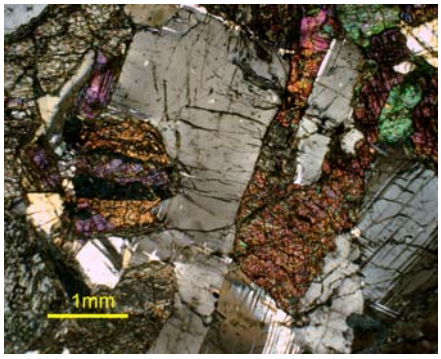

_____ 1 mm

TPE017. Clinopyroxenite-gabbro dike. Primary minerals include plagioclase, clinopyroxene and hornblende. Plagioclase grains are moderately abundant at 30% and ~0.5 mm in diameter on average. Clinopyroxene crystals, also averaging ~0.5 mm in diameter, are embedded in a plagioclase-hornblende matrix and comprise 30% of the rock. Hornblende is similarly ~0.5 mm in diameter and 30% in abundance, with brown pleochroism and moderate birefringence. A serpentine vein, about 0.25 mm wide, cuts across the existing groundmass and constitutes 10% of the rock.

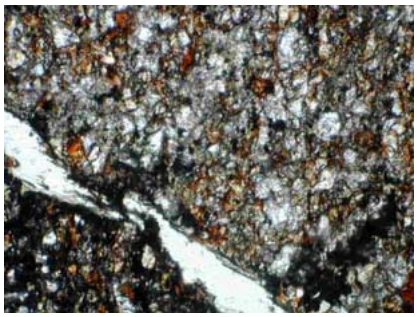

_____ 1 mm

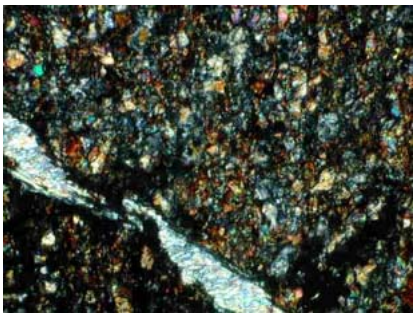

_____ 1 mm

TPB023. (TPG023) Basalt. This rock is aphanitic with a fine-grained groundmass mostly consisting of plagioclase (90%). A few plagioclase phenocrysts exist (5%), and are usually subhedral in habit and 1 mm in diameter. Ilmenite phenocrysts (5%) are tabular and euhedral, 10-20 μm, and display subtle light brown-pink pleochroism.

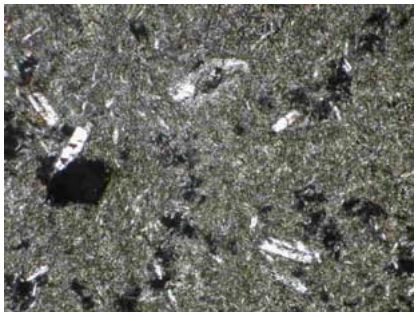

_____ 1 mm

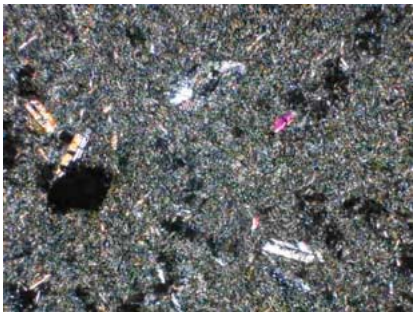

_____ 1 mm

TPH063. Gabbro vein in peridotite. Primary plagioclase grains only comprise 20% of the thin section with subhedral and rounded habits that vary in size from 10 μm to 1 mm. The original plagioclase has been almost entirely replaced by sericite (50%). Clinopyroxene (30%) is highly altered, anhedral, anywhere from 10 μm to 1-2 mm in diameter, and in some cases overprints primary plagioclase crystals.

TPE063. Amphibole vein. This rock consists primarily of plagioclase (40%), with secondary minerals amphibole (20%), and talc (10%). The plagioclase is tabular, slightly subhedral, and ~ 1 mm on average. The talc is anhedral with lacy edges and seems to have grown around the plagioclase grains. Seriticization has occurred in some cases and accounts for 30% of the rock's composition.

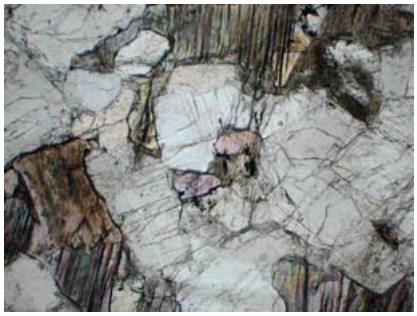

_____ 1 mm

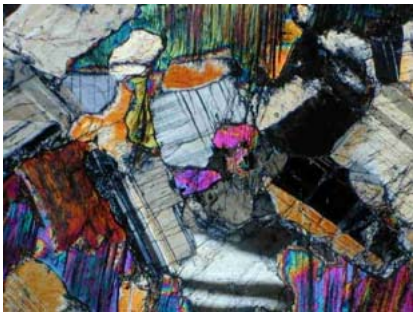

_____ 1 mm

TPE062. No thin section.

TPH005. Layered gabbro. Plagioclase grains comprise 50% of the rock and are tabular, euhedral to subhedral and 1-2 cm on average. Olivine phenocrysts (30%, 0.25 mm in diameter) are highly fractured and occur in clusters such that the original shape and size of the grain are evident (2-4 mm). Orthopyroxene (5%) and clinopyroxene (10%) are subhedral and rounded and 2-4 mm in diameter on average. Orthopyroxene grains are grungy in some places. Amphibole (5% or less) sometimes occurs at the edges of relict olivine grains.

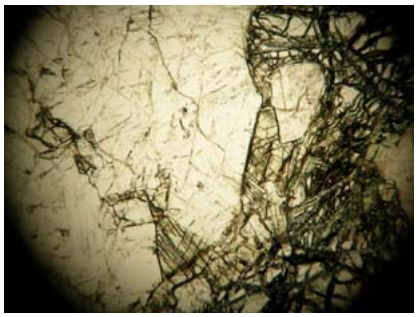

_____ 1 mm

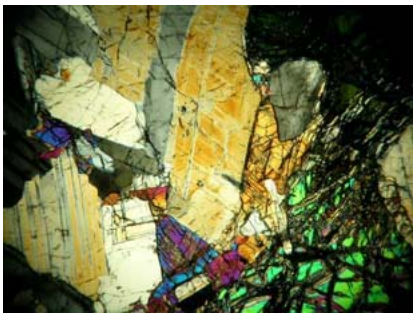

_____ 1 mm

TPE049. Plagioclase-rich gabbro. Plagioclase is the predominant mineral in this specimen, at 65% abundance. The plagioclase crystals are 1-2 cm, euhedral to subhedral in habit, and hexagonal or rounded in shape. Olivine is also present (20%, 0.25 mm or less) and occurs in clusters such that the original shape and size of the grain are evident (2-5 mm). Serpentine (6%) and magnetite (4%) fill the fractures in the olivine grains. Amphibole (5%) occurs around some olivine clusters and is occasionally grungy.

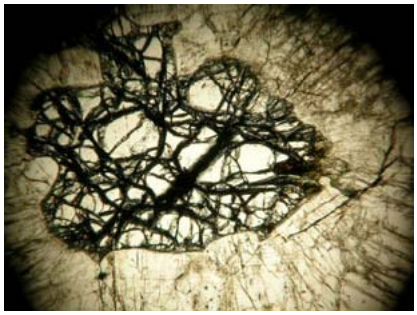

_____ 1 mm

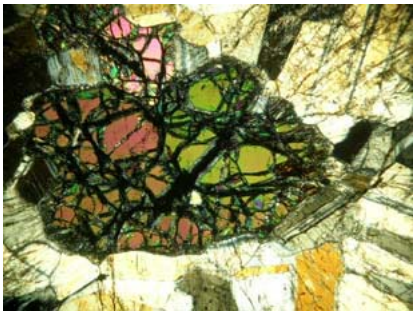

_____ 1 mm

REFERENCES

Alard, O., Griffin, W.L., Lorand, J-P., Jackson, S.E., and O'Reilly, S.Y. (2000) Non-chondritic distribution of the highly siderophile elements in mantle sulphides. *Nature London* **407**: 891-894.

Alard, O., Griffin, W.L., Pearson, N.J., Lorand, J-P., and O'Reilly, S.Y. (2002) New insights into the Re-Os systematics of sub-continental lithospheric mantle from in situ analysis of sulphides. *Earth and Planetary Science Letters* **203**: 651-663.

Alard, O., Luguet, A., Pearson, N.J., Griffin, W.L., Lorand, J-P., Gannoun, A., Burton, K.W., and O'Reilly, S.Y. (2005) In situ Os isotopes in abyssal peridotites bridge the isotopic gap between MORBs and their source mantle. *Nature London* **436**: 1005-1008.

Allègre, C.J., Ben Othman, D., Polve, M. and Richard, P. (1979) The Nd-Sr isotopic correlation in mantle materials and geodynamic consequences. *Physics of the Earth and Planetary Interiors* **19**: 293-306.

Allègre, C.J., Brevart, O, Dupre, B., and Minster, J.F. (1980) Isotopic and chemical effects produced in a continuously differentiating convecting Earth mantle. *Philosophical Transaction of the Royal Society of London, Series A: Mathematical and Physical Sciences* **297**: 447-477.

Allègre, C.J. and Luck, J.M. (1980) Osmium isotopes as petrogenetic and geological tracers. *Earth and Planetary Science Letters* **48**: 148-154.

Allègre, C.J. and Turcotte, D.L. (1985) Geodynamic mixing in the mesosphere boundary layer and the origin of oceanic islands. *Geophysical Research Letters* **12**: 207-210.

Allègre, C.J. and Turcotte, D.L. (1986) Implications of a two-component marble-cake mantle. *Nature London* **323**: 123-127.

Anma, R., Armstrong, R., Danhara, T., Orihashi, Y. and Iwano, H. (2006) Zircon sensitive high mass-resolution ion microprobe U-Pb fission track ages for gabbros and sheeted dykes of the Taitao Ophiolite, Southern Chile, and their tectonic implications. *Island Arc* **15**: 130-142.

Barnes, S. J. and Roeder, P. L. (2001) The range of spinel compositions in terrestrial mafic and ultramafic rocks. *Journal of Petrology* **42**: 2279-2302.

Batiza, R. (1984) Inverse relationship between Sr isotope diversity and rate of oceanic volcanism has implications for mantle heterogeneity. *Nature London* **309**: 440-441.

Birck, J.L., Barman, M.R., and Capmas, F. (1997) Re-Os isotopic measurements at the femtomole level in natural samples. *Geostandards Newsletter – The Journal of Geostandards and Geoanalysis* **21**: 19-27.

Brandon, A.D., Creaser, R.A., Shirey, S.B. and Carlson, R.W. (1996) Osmium recycling in subduction zones. *Science* **272**: 861-864.

Brandon, A. D., Snow, J. E., Morgan, J. W. and Mock, T. D. (2000) ^{190}Pt-^{186}Os and ^{187}Re-^{187}Os systematics of abyssal peridotites. *Earth and Planetary Science Letters* **177**: 319-335.

Briqueu, L., Mevel, C., and Boudier, F. (1991) Sr, Nd and Pb isotopic constraints in the genesis of a calc-alkaline plutonic suite in Oman Ophiolite related to the obduction process. *Petrology and Structural Geology* **5**: 517-542

Böhlke, J.K., Honnorez, J., Honnorezguerstein, B.M., Muehlenbachs, K. and Petersen, N. (1981) Heterogeneous alteration of the upper oceanic-crust – Correlation of rock chemistry, magnetic-properties, and O isotope ratios with alteration patterns in basalts from Site 396B, DSDP. *Journal of Geophysical Research* **86**: 7935-7950.

Bourgois, J., Martin, H., Lagabrielle, Y., Le Moigne, J., and Frutos Jara, J. (1996) Subduction erosion related to spreading-ridge subduction: Taitao peninsula (Chile margin triple junction area). *Geology* **24**:723-726.

Boyd, F.R., and Mertzman, S.A., (1987). Composition of structure of the Kaapvaal lithosphere, southern Africa. *Geochemical Society Special Publication* **1**: 13-24.

Büchl, A., Brügmann, G.E., Batanova, V.G. and Hofmann, A.W. (2004) Os mobilization during melt percolation: The evolution of Os isotope heterogeneities in the mantle sequence of the Troodos ophiolite, Cyprus. *Geochimica et Cosmochimica Acta* **68**: 3397-3408.

Büchl, A., Brügmann, G., Batanova, V.G., Münker, C. and Hofmann, A.W. (2002) Melt percolation monitored by Os isotopes and HSE abundances: a case study from the mantle section of the Troodos Ophiolite. *Earth and Planetary Science Letters* **204**: 385-402.

Cande, S.C. and Leslie, R.B. (1986) Late Cenozoic tectonics of the southern Chile Trench. *Journal of Geophysical Research* **91**: 471-496.

Carlson, R.W. and Nowell, G.M. (2001) Olivine-poor sources for mantle-derived magmas; Os and Hf isotopic evidence from potassic magmas of the Colorado Plateau. *Geochemistry, Geophysics, Geosystems* **2**: Issue 6.

Chalot-Prat, F., Ganne, J. and Lombard, A. (2003) No significant element transfer from the oceanic plate to the mantle wedge during subduction and exhumation of the Tethys lithosphere (Western Alps). *Lithos* **69**: 69-103.

Clayton, R.N and Mayeda, T.K. (1963) The use of bromine pentafluoride in the extraction of oxygen from oxides and silicates for isotopic analysis. *Geochimica et Cosmochimica Acta* **27**: 43-52.

Cohen, R.S. and O'Nions, R.K. (1982) Identification of recycled continental material in the mantle from Sr, Nd and Pb isotope investigations. *Earth and Planetary Science Letters* **61**: 73-84

Davidson, J., Mpodozis, C., Godoy, E., Herve, F., Pankhurst, R. and Brook, M. (1987) Late Paleozoic accretionary complexes on the Gondwana margin of southern Chile: Evidence from the Chonos archipelago, in Gondwana Six, structure, tectonics and geophysics. *Geophysical Monograph* **40**: 221-227.

DePaolo, D.J. and Wasserburg, G.J. (1976) Inferences about magma sources and mantle structure from variations of $^{143}Nd/^{144}Nd$. *Geophysical Research Letters* **3**: 743-746.

Dick, H.J.B. and Bullen, T. (1984) Chromian spinel as a petrogenetic indicator in abyssal and alpine-type peridotites and spatially associated lavas. *Contributions to Mineralogy and Petrology* **86**: 54-76.

Droop, G.T.R (1987) A general equation for estimating Fe^{3+} concentrations in ferromagnesian silicates and oxides from microprobe analyses, using stoichiometric criteria. *Mineralogical Magazine* **51**: 431-435.

Eiler, J.M., McInnes, B., Valley, J.W., Graham, C.M., and Stolper, E.M. (1996) Oxygen isotope evidence for slab-derived fluids in the sub-arc mantle. *Nature* **393**: 777-781.

Elton, D. (1991) Geochemical evidence for formation of the Bay-of-Islands Ophiolite above a subduction zone. *Nature* **354**: 140-143.

Elthon, D., Nelson, E., Allen, M., and Forsythe, R. (1998) Petrology and geochemistry of the Taitao Ophiolite, Chile: The world's youngest ophiolite (?). *Geological Survey of Finland* Special Paper **26**: 20.

Escrig, S., Schiano, P., Schilling, J.-G., and Allegre, C. (2005) Rhenium-Osmium isotope systematics in MORB from the southern Mid-Atlantic Ridge (40^o – 50^o S). *Earth and Planetary Science Letters* **235**: 528-548.

Faure, G. and Hurely, P.M. (1963) The isotopic composition of strontium in oceanic and continental basalts; application to the origin of igneous rocks. *Journal of Petrology* **4**: 31-50.

Foley, S. (1992) Petrological characterization of the source components of potassic magmas; geochemical and experimental constraints. *Lithos* **28**: 187-204.

Gannoun, A., Burton, K.W., Thomas, L.E., Parkinson, I.J., van Calsteren, P., and Schiano, P. (2004) Osmium isotope heterogeneity in the constituent phases of mid-ocean ridge basalts. *Science* **303**: 70-72.

Gao, S., Rudnick, R.L., Carlson, R.W., McDonough, W.F., and Yongsheng, L. (2002) Re-Os evidence for replacement of ancient mantle lithosphere beneath the North China Craton. *Earth and Planetary Science Letters* **198**: 307-322

Gast, P.W., Tilton, G.R., and Hedge, C. (1964) Isotopic composition of lead and strontium from Ascension and Gough islands. *Science* **145**: 1181-1185.

Godard, M., Jousselin, D., and Bodinier, J.-L. (2000) Relationships between geochemistry and structure beneath a palaeo-spreading centre; a study of the mantle section in the Oman Ophiolite. *Earth and Planetary Science Letters* **180**: 133-148

Goldstein, S.L., O'Nions, R.K., and Hamilton, P.J. (1984) A Sm-Nd isotopic study of atmospheric dusts and particulates from major river systems. *Earth and Planetary Science Letters* **70**: 221-236.

Guivel, C., Lagabrielle, Y., Bourgois, J., Maury, R. C., Fourcade, S., Martin, H., and Arnaud, N. (1999) New geochemical constraints for the origin of ridge-subduction-related plutonic and volcanic suites from the Chile Triple Junction (Taitao Peninsula and Site 862, LEG ODP141 on the Taitao Ridge). *Tectonophysics* **311**: 83-111.

Hanan, B.B., Kingsley, R.H., and Schilling, J.G. (1986) Pb isotope evidence in the South Atlantic for migrating ridge-hotspot interactions. *Nature London* **322**: 137-144

Hart, S.R., Schilling, J.-G., and Powell, J.L. (1973) Basalts from Iceland and along the Reykjanes Ridge; Sr Isotope Geochemistry. *Nature; Physical Science London* **246**: 104-107

Hart, S.R. and Zindler, A. (1986) In search of a bulk-Earth composition. *Chemical Geology* **57**: 247-267

Harvey, J., Gannoun, A., Burton, K.W., Rogers, N.W., Alard, O. and Parkinson, I.J. (2006) Ancient melt extraction from the oceanic upper mantle revealed by Re-Os isotopes in abyssal peridotites from the Mid-Atlantic ridge. *Earth and Planetary Science Letters* **244**: 606-621.

Hauri, E.H. and Hart, S. R. (1997) Rhenium abundances and systematics in oceanic basalts. *Chemical Geology* **139**: 185-205.

Hofmann, A.W. (1997) Mantle geochemistry: the message from oceanic volcanism. *Nature* **385**: 219-229.

Irving, A.J. (1980) Petrology and geochemistry of composite ultramafic xenoliths in alkalic basalts and implications for magmatic processes within the mantle. *American Journal of Science* **280-A**: 389-426

Kaeding, M., Forsythe, R. D., and Nelson, E. P. (1990) Geochemistry of the Taitao ophiolite and near-trench intrusions from the Chile Margin Triple Junction. *Journal of South American Earth Sciences* **3**: 161-177

Kelemen, P.B., Koga, K., and Shimizu, N. (1997) Geochemistry of gabbro sills in the crust-mantle transition zone of the Oman Ophiolite; implications for the origin of the oceanic lower crust. *Earth and Planetary Science Letters* **146**: 475-488

Kellogg, L.H. and Turcotte, D.L. (1991) Mixing and the distribution of heterogeneities in a chaotically convecting mantle. *Journal of Geophysical Research* **95**: 421-432

Klein, E.M. and Karsten, J.L. (1995) Ocean-ridge basalts with convergent-margin geochemical affinities from the Chile Ridge. *Nature London* 374: 52-57.

Lagabrielle, Y., Guivel, C., Maury, R. C., Bourgois, J., Fourcade, S., and Martin, H. (2000) Magmatic-tectonic effects of high thermal regime at the site of active ridge subduction: the Chile Triple Junction model. *Tectonophysics* **326**: 255-268.

Lapierre, H., Samper, A., Bosch, D., Maury, R.C., Bechennec, F., Cotton, J., Demant, A., Brunet, P., Keller, F. and Marcoux, J. (2004) The Tethyan plume; geochemical diversity of Middle Permian basalts from the Oman rifted margin. *Lithos* **74**: 167-198.

Levasseur, S., Birk, J.-L. and Allègre, C.J. (1998) Direct measurement of fetomoles of osmium and the $^{187}Os/^{186}Os$ ratio in seawater. *Science* **282**: 272-274.

Luck, J.-M. and Allègre, C.J. (1983) ^{187}Re-^{187}Os systematics in meteorites and cosmochemical consequences. *Nature London* **302**: 130-132

Luck, J.-M. and Allègre, C.J. (1991) Osmium isotopes in ophiolites. *Earth and Planetary Science Letters* **107**: 406-415.

Mattey, D., Lowry, D. and Macpherson, C. (1994) Oxygen isotope composition of mantle peridotite. *Earth and Planetary Science Letters* **128**: 231-241.

McDonough, W.F. and Sun, S.-S. (1995) Composition of the Earth. *Chemical Geology* **120**: 223-253

McKenzie, D. (1979) Finite deformation during fluid flow. *Geophysical Journal of the Royal Astronomical Society* **58**: 689-715

Meisel, T., Walker, R.J., Irving, A.J., Lorand, J.-P. (2001) Osmium isotopic compositions of mantle xenoliths; a global perspective. *Geochimica et Cosmochimica Acta* **65**: 1311-1323.

Meisel, T., Walker, R. J., and Morgan, J. W. (1996) The osmium isotopic composition of the Earth's primitive upper mantle. *Nature* **383**: 517-520.

Moreir, M., Doucelance, R., Kurz, M.D., Dupre, B., and Allègre, C.J. (1999) Helium and lead isotope geochemistry of the Azores Archipelago. *Earth and Planetary Science Letters* **169**: 189-205.

Morgan, J.W. (1971) Osmium-76. *Handbook of elemental abundances in meteorites:* 451-462.

Morgan, J.W. (1986) Ultramafic xenoliths; clues to Earth's late accretionary history. *Journal of Geophysical Research* **91**: 12,375-12,387.

Nelson, E., Forsythe, R., Diemer, J., Allen, M. and Urbin, O. (1993) Taitao ophiolite; a ridge collision ophiolite in the forearc of southern Chile (46^{o}S). *Revista Geological de Chile* **20**: 137-165.

Niu, Y., Langmuir, C.H., and Kinzler, R.J. (1997) The origin of abyssal peridotites; a new perspective. *Earth and Planetary Science Letters* **152**: 251-265.

O'Hara, M.J. and Matthews, R.E. (1981) Geochemical evolution in an advancing, periodically replenished, periodically tapped, continuously fractionated magma chamber. *Journal of Geological Society of London* **138**: 237-277

Parkinson, I.J., Hawkesworth, C.J., and Cohen, A.S. (1998) Ancient mantle in a modern arc; osmium isotopes in Izu-Bonin-Mariana Forearc peridotites. *Science* **281**: 2011-2013.

Paulssen, H. (1988) Evidence for a sharp 670-km discontinuity as inferred from P-to-S converted waves. *Journal of Geophysical Research* **93**: 10,489-10,500.

Pearson, D.G. and Nowell, G.M. (2004) Re-Os and Lu-Hf isotope constraints on the origin and age of pyroxenites from the Beni Bousera peridotite massif; implications for mixed peridotite-pyroxenite mantle sources. *Journal of Petrology* **45**: 439-455

Piercey, S.J. (2003) Neodymium isotope geochemistry of felsic volcanic and intrusitve rocks from the Yukon-Tanana Terrane in the Finlayson Lake region, Yukon, Canada. *Canadian Journal of Earth Sciences* **40**: 77-97

Polvé, M. and Allègre, C.J. (1980) Orogenic lherzolite complexes studied by ^{87}Rb-^{87}Sr; a clue to understand the mantle convection process? *Earth and Planetary Science Letters* **51**: 71-93.

Rampone, E., Hofmann, A.W., Piccardo, G.B., Vannucci, R., Bottazzi, P. and Ottolini, L. (1996) Trace element and isotope geochemistry of depleted peridotites from an N-MORB type ophiolite (Internal Liguride, N. Italy). *Contributions to Mineralogy and Petrology* **123**: 61-76.

Rampone, E. (2004) Mantle dynamics during Permo-Mesozoic extension of the Europe-Adria lithosphere; insights from the Ligurian ophiolites. *Periodico di Mineralogia* **73**: 215-230.

Rautenschlein, M., Jenner, G.A., Hertogen, J., Hofmann, A.W., Kerrich, R., Schmincke, H.U. and White, W.M. (1985) Isotopic and trace element composition of volcanic glasses from the Akaki Canyon, Cyprus; implications for the origin of the Troodos Ophiolite. *Earth and Planetary Science Letters* **75**: 369-383.

Reichen, L.E. and Fahey, J.J. (1962) An improved method for the determination of FeO in rocks and minerals including garnet. *U.S. Geological Survey Bulletin* **1144B**: 1-5.

Reisberg, L and Lorand, J.-P. (1995) Longevity of sub-continental mantle lithosphere from osmium isotope systematics in orogenic peridotite massifs. *Nature* **376**: 159-162.

Reisberg, L. and Meisel, T. (2002) The Re-Os isotopic system: A review of analytical techniques. *Geostandards Newsletter – The Journal of Geostandards and Geoanalysis* **26**: 249-267

Richter, F.N. and Ribe, M.N. (1979) On the importance of advection in determining the local isotopic composition of the mantle. *Earth and Planetary Science Letters* 43: 212-222.

Roy-Barman, M. and Allègre, C.J. (1994) $^{187}Os/^{186}Os$ ratios of mid-ocean ridge basalts and abyssal peridotites. *Geochimica et Cosmochimica Acta* **58**: 5043-5054.

Roy-Barman, M. and Allègre, C.J. (1995) $^{187}Os/^{186}Os$ in oceanic island basalts; tracing oceanic crust recycling in the mantle. *Earth and Planetary Science Letters* **129**: 145-161.

Roy-Barman, M., Wasserburg, G.J., Papanastassiou, D.A., Chaussidon, M. (1998) Osmium isotopic compositions and Re-Os concentrations in sulfide globules from basaltic glasses. *Earth and Planetary Science Letters* **154**: 331-347.

Rumble, D. (III), Farquhar, J., Young, E.D., and Christensen, C.P. (1997) In situ oxygen isotope analysis with an excimer laser using F_2 and BrF_5 reagents and O_2 gas as analyte. *Geochimica et Cosmochimica Acta* **61**: 4229-4234.

Salters, V.J.M. and Stracke, A. (2004) Composition of the depleted mantle. *Geochemistry Geophysics Geosystems* **5**: Q05004.

Schiano, P., Birck, J.-L., and Allègre, C.J. (1997) Osmium-strontium-neodymium-lead isotopic covariations in mid-ocean ridge basalt glasses and the heterogeneity of the upper mantle. *Earth and Planetary Science Letters* **150**: 363-379

Schilling, J.-G. (1973) Iceland Mantle Plume; Geochemical Study of Reykjanes Ridge. *Nature London* **242**: 565-571

Sharma, M., Wasserburg, G.J., Papanastassiou, D.A., Quick, J.E., Sharkov, E.V. and Laz'ko, E.E. (1995) High $^{143}Nd/^{144}Nd$ in extremely depleted mantle rocks. *Earth and Planetary Science Letters* **135**: 101-114.

Shirey, S. B. and Walker, R. J. (1995) Carius tube digestion for low-blank rhenium-osmium analysis. *Analytical Chemistry* **67**: 2136-2141.

Shirey, S. B. and Walker R. J. (1998) The Re-Os isotope system in cosmochemistry and high-temperature geochemistry. *Annual Reviews: Earth and Planetary Science Letters* **26**: 423-500.

Smoliar, M.I., Walker, R.J., Morgan, J.W. (1996) Re-Os ages of Group IIA, IIIA, IVA, and IVB iron meteorites. *Science* **271**: 1099-1102.

Snow, J.E. and Dick, H.J.B. (1995) Pervasive magnesium loss by marine weathering of peridotite. *Geochimica et Cosmochimica Acta* **59**: 4219-4235.

Snow, J. E. and Reisberg, L. (1995) Os isotopic systematics of the MORB mantle: results from altered abyssal peridotites. *Earth and Planetary Science Letters* **133**: 411-421.

Snow, J.E., Schmidt, G. and Rampone, E. (2000) Os isotopes and highly siderophile elements (HSE) in the Ligurian ophiolites, Italy. *Earth and Planetary Science Letters* **175**: 119-132

Standish, J.J., Hart, S.R., Blusztajn, J., and Dick, H.J.B. (2002) Abyssal peridotite osmium isotopic compositions from Cr-spinel. *Geochemistry, Geophysics, Geosystems* **3**: 1004; doi:10.1029/2001GC000161.

Talkington, R.W. and Lipin, B.R. (1984) Platinum-group minerals in chromite seams of the Stillwater Complex, Montana. *Economic Geology* **81**: 1179-1186.

Tatsumoto, M. (1966) Genetic relations of oceanic basalts as indicated by lead isotopes. *Science* **153**: 1094-1101

Turcotte, D.L. and Oxburgh, E.R. (1967) Finite amplitude convective cells and continental drift. *Transactions – American Geophysical Union* **48**: 213.

Tsuru, A., Walker, R.J., Kontinen, A., Peltonen, P. and Hanski, E. (2000) Re-Os isotopic systematics of the 1.95 Ga Jourma Ophiolite Complex, northern Finland. *Chemical Geology* **164**: 123-141.

Valley, J.W., Kitchen, N., Kohn, M.J., Niendorf, C.R., Spicuzza, M.J. (1995) UWG-2, a garnet standard for oxygen isotope ratios; strategies for high precision and accuracy with laser heating. *Geochimica et Cosmochimica Acta* **59**: 5223-5231.

Veloso et al., 2005, Emplacement of the Taitao Ophiolite, Southern Chile, deduced from paleostress and fission track constraints. In **R.Anma, (ed), Spacio-temporal changes in Chilean arc magmatism and its relation to the Chile ridge subduction**, *Japan Society for Promoting Science Report* **13373004**: 68-78.

Walker, R.J., Shirey, S.B., and Boyd, F.R. (1989) Os, Sr, Nd, and Pb isotope systematics of Southern African peridotite xenoliths; implications for the chemical evolution of subcontinental mantle. *Geochimica et Cosmochimica Acta* **53**: 1583-1595.

Walker, R.J. and Morgan, J.W. (1989) Rhenium-osmium isotope systematics of carbonaceous chondrites. *Science* **243**: 519-522.

Walker, R. J., Prichard, H. M., Ishiwatari, A., and Pimentel, M. (2002) The osmium isotopic composition of convecting upper mantle deduced from ophiolite chromites. *Geochimica et Cosmochimica Acta* **66**: 329-345.

Walker, R. J., Brandon, A. D., Bird, J. M., Piccoli, P. M., McDonough, W. F., and Ash, R. D. (2005) ^{187}Os-^{186}Os Systematics of Os-Ir-Ru alloy grains from Southwestern Oregon. *Earth and Planetary Science Letters* **230**: 211-226.

Walter, M.J. (1999) Melting residues of fertile peridotite and the origin of cratonic lithosphere. In **Mantle Petrology: Field Observations and High Pressure Experimentation: A Tribute to Francis R. (Joe) Boyd**, *Geochemical Society, Special Publications* **6**: 225-239.

White, W.M., Schilling, J.-G., and Hart, S.R. (1976) Evidence for the Azores mantle plume from strontium isotope geochemistry of the central North Atlantic. *Nature London* **263**: 659-663

White, W.M., Tapia, M.D.M. and Schilling, J.G. (1979) The petrology and geochemistry of the Azores Islands. *Contributions to Mineralogy and Petrology* **69**: 201-213.

Widom, E., Carlson, R.W., Gill, J.B., and Schmincke, H.U. (1997) Th-Sr-Nd-Pb isotope and trace element evidence for the origin of the Sao Miguel, Azores, enriched mantle source. Chemical Geology 140: 49-68.

Workman, R.K. and Hart, S.R. (2005) Major and trace element composition of the depleted MORB mantle (DMM). *Earth and Planetary Science Letters* **231**: 53-72.

Zindler, A., Staudigel, H., Batiza, R. (1984) Isotope and trace element geochemistry of young Pacific seamounts; implications for the scale of upper mantle heterogeneity. *Earth and Planetary Science Letters* **70**: 175-195

Zindler, A. and Hart, S. (1986) Helium; problematic primordial signals. *Earth and Planetary Science Letters* **79**: 1-8.